①

ORNL/Sub/85-27461/1

ornl

OAK RIDGE
NATIONAL
LABORATORY

MARTIN MARIETTA

AD-A186 612

Energy Division
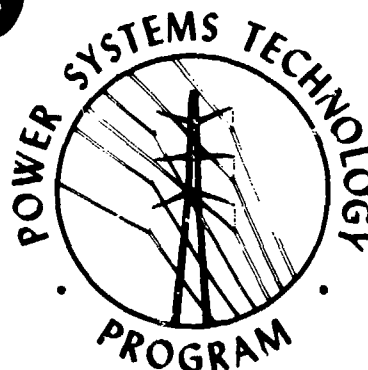
The Effects of Corona on Current Surges Induced on Conducting Lines by EMP: A Comparison of Experiment Data With Results of Analytic Corona Models

J. P. Blanchard
F. M. Tesche
B. W. McConnell

DTIC
S ELECTE
OCT 2 6 1987
D
D

POWER SYSTEMS TECHNOLOGY PROGRAM

87 10 14 116

THE EFFECTS OF CORONA ON CURRENT SURGES
INDUCED ON CONDUCTING LINES BY EMP:
A COMPARISON OF EXPERIMENT DATA
WITH RESULTS OF ANALYTIC CORONA MODELS

J. P. Blanchard
F. M. Tesche
B. W. McConnell, ORNL

ACKNOWLEDGEMENTS

TABLE OF CONTENTS

TABLE OF CONTENTS

LIST OF TABLES

LIST OF FIGURES

ABSTRACT

An experiment to determine the interaction of an intense electromagnetic pulse (EMP) , such as that produced by a nuclear detonation above the earth's atmosphere, was performed in March, 1986 at Kirtland Air Force Base near Albuquerque, New Mexico. The results of that experiment have been published [1,2] without analysis. Following an introduction of the corona phenomenon, the reason for interest in it, and a review of the experiment, this paper discusses five different analytic corona models that may model corona formation on a conducting line subjected to EMP. The results predicted by these models are compared with measured data acquired during the experiment to determine the strengths and weaknesses of each model.

EXECUTIVE SUMMARY

A nuclear detonation in or above the Earth's atmosphere produces an intense electromagnetic pulse (EMP). The interaction of this EMP with the nation's power systems could disrupt these systems leaving large areas of the country without electric power. This is a problem of present concern [1]. The extent and duration of these system blackouts, should they occur, is presently unknown. To determine the probability of such an occurrence and its severity, the Department of Energy (DOE) has formulated a program through the Oak Ridge National Laboratory (ORNL) to assess the effects of EMP on commercial power systems.

The major research effort in this program is being conducted by the Westinghouse Electric Corporation. This effort has produced several computer models for EMP interaction, has performed experiments on power systems equipment to characterize its EMP behavior, and has developed an assessment methodology. The methodology uses fault tree analysis to estimate system behavior.

In the area of numerical modeling of the EMP interaction of power lines with the EMP, a number of models have been developed. These models are generally linear models and the effects of corona; i.e., ionization of the air in the vicinity of the conductor, are not taken into account. Corona is known to alter the shape and magnitude of an injected pulse by a

damping action. However, the models used to predict corona effects on injected pulses are not appropriate for modeling an EMP coupled pulse. These injected pulse corona models generally use a pulse rise time of microseconds as compared to a few tens of nanoseconds rise time for the EMP coupled pulse. Also, the EMP pulse is characterized as a distributed source which requires different modeling techniques. There was no known data on corona effects for fast rising (nanosecond) impulse and distributed excitation. Consequently, in March, 1986, an EMP corona experiment was conducted at Kirtland Air Force Base, New Mexico. This work was funded in part by the DOE and by the Defense Nuclear Agency. This report examines some of the experimental results in detail; viz, a baseline test case representative of the data collected, and compares these results with five corona models.

In general, three of the models fit the measured data reasonably well. In all cases, the limitations of the experimental configuration presented some difficulty in analyzing the data. However, these difficulties were expected and could not be avoided using the present facilities. In particular, the experimental configuration allows the examination of only "positive" conductor charge and has a limited "clear time" of about 90 ns. "Clear time" is the time prior to the appearance of significant reflections in the experimental configuration.

The results of the tests indicate that corona is present under EMP conditions. In fact, the experimental team was unable to find a configuration without corona. Therefore, all comparisons to the no corona case are with respect to a calculated no corona response. While all models fit the data over certain ranges, no single model is capable of covering the entire data range. It is clear that ignoring corona in the evaluation of EMP impact will produce a conservative result; however, the degree of conservatism remains in question.

I. INTRODUCTION

The interaction of an intense electromagnetic pulse (EMP), such as that produced by a nuclear detonation in or above the earth's atmosphere, with a power system is a problem of present concern [1]. The EMP could disrupt the functioning of the system and leave large areas of the country without electrical power. Although occasional localized power disruptions are experienced in commercial power systems, the large geographical coverage of a high altitude EMP suggests that there is a possibility that power outages over extended areas might occur in the event of such a nuclear detonation.

The extent of such a power black-out (should it occur), as well as the length of time that the black-out might exist, is presently unknown. In order to determine the probability of such an occurrence and its severity, should it occur, the U. S. Department of Energy (DOE) has instigated a program through the Oak Ridge National Laboratory (ORNL) to assess the effects of an EMP on the commercial power system. This effort, being conducted by the Westinghouse Electric Co., has developed a number of computer models for EMP interaction studies, has performed experiments on power system equipment to characterize their EMP behavior, and has developed an

assessment methodology based on a fault tree analysis to estimate the system behavior.

In the area of numerical modeling of the EMP interaction of power lines with the EMP, a number of transmission line coupling models have been developed. The majority of these are linear models, and consequently, the effects of corona (either due to the energized line, or to the EMP itself) are not taken into account. However, it is desirable to understand the effect that corona has on the coupled EMP response of long lines and to ascertain if completely neglecting the corona effects in the power system assessment is reasonable.

Several investigators have previously studied the effects of corona on the EMP response of long lines analytically. Much of this work, however, has not been directly verified by experimental observation. Consequently, in March, 1986, an EMP corona experiment, funded in part by DOE through ORNL and by the Defense Nuclear Agency (DNA), was conducted at Kirtland Air Force Base in New Mexico. The data obtained in this measurement program have been published [2, 3], without analysis comparing the experimental results with the various corona models. The purpose of the present document, therefore, is to examine some of the experimental

results in more detail and to compare them with the results from the calculational corona models.

In Section II of this report, brief discussions of the formation and the effects of corona are presented. This is followed in Section III by a review of the experiment and the baseline test configuration chosen for comparing the predictions of several corona models with the measured data. The rationale for selecting the baseline test configuration is also summarized.

After these general background sections, a description of the different corona models analyzed in this paper is given in Section IV. The results predicted by each of the corona models are compared with the data acquired for a chosen baseline configuration and an determination of the appropriate parameters for each model is made to determine the best fit of the model to the test case data.

Following this, Section V concludes the report with a summary of the important observations and some possible directions for future research.

II. WHAT IS CORONA? · A BRIEF BACKGROUND

In this section, an overview of Peek's law, describing the electric field limit beyond which corona formation will begin, is presented. This is followed by a brief discussion of the effects of corona on power lines.

A. Peek's Law

Typically, the atmosphere is a dielectric, or insulator, for which the nominal dielectric strength is approximately 30 kV/cm. If the local electric field exceeds this value, corona will begin to form. The actual value of the dielectric strength may change, however, depending upon wire roughness, barometric pressure and temperature, as indicated by Peek's law [4, 5]:

$$E_c = E_0 \, m \, \delta \, [1 + k/(\delta r)^{1/2}] \qquad \text{for coaxial geometry}$$

where:

E_c is the threshold electric field above which corona may be expected to form.

E_0 is the sparking field strength for air under STP and uniform field for gaps on the order of 1 cm. An approximate value is 31 kV/cm.

m is a coefficient describing the conductor surface roughness: $0.6 < m < 1.0$, with $m = 1.0$ for smooth, round conductors

r is the conductor radius (inner conductor for a coaxial geometry).

For r in cm, the value of k is 0.308 $cm^{1/2}$. The variable δ is the air density factor relative to that at standard temperature and pressure (STP), which is equal to $0.392p/T$, where p is the pressure corrected to sea level in mm-Hg and T is the ambient temperature in degrees Kelvin. This law is valid over a large range of pressures, for $0.1mm < r < $ several cm, and for applied voltages from DC to several kHz.

The ambient air pressure, corrected to sea level, and temperature data on the date of the baseline test were obtained from the National Weather Service office in Albuquerque, NM. The nominal values for these parameters for the baseline case chosen are as follows:

$E_0 = 3.1 \times 10^6$ (Volts/meter)

$0.6 < m < 1.0$

$752.1 < p < 754.9$ (mm-Hg)

$$279.1 < T < 280.2 \quad \text{(degrees Kelvin)}$$

$$r = 1.07 \quad \text{(cm)}.$$

Figure 1 contains a plot of E_c as a function of m for the ranges of p and T indicated above.

B. Corona Effects

When the local electric field intensity exceeds the dielectric strength of the atmosphere, ionization of the air occurs in the region of high field intensity. This effectively transforms the air in that region into a weak electrical conductor. It is well known that one way the local electric field may be enhanced is by the presence of a wire with a relatively small radius carrying a large current. When the air is ionized around a wire because of the enhanced local electric field, corona (from the Greek kronos, or crown) is said to have formed. The formation of corona on a transmission line is generally undesirable, since it dissipates some of the line's power and changes the capacitance of the transmission line, suppressing the amount of current the line may carry.

Studies of the coupling of an electromagnetic pulse (EMP) produced by a nuclear detonation to a long wire indicate that
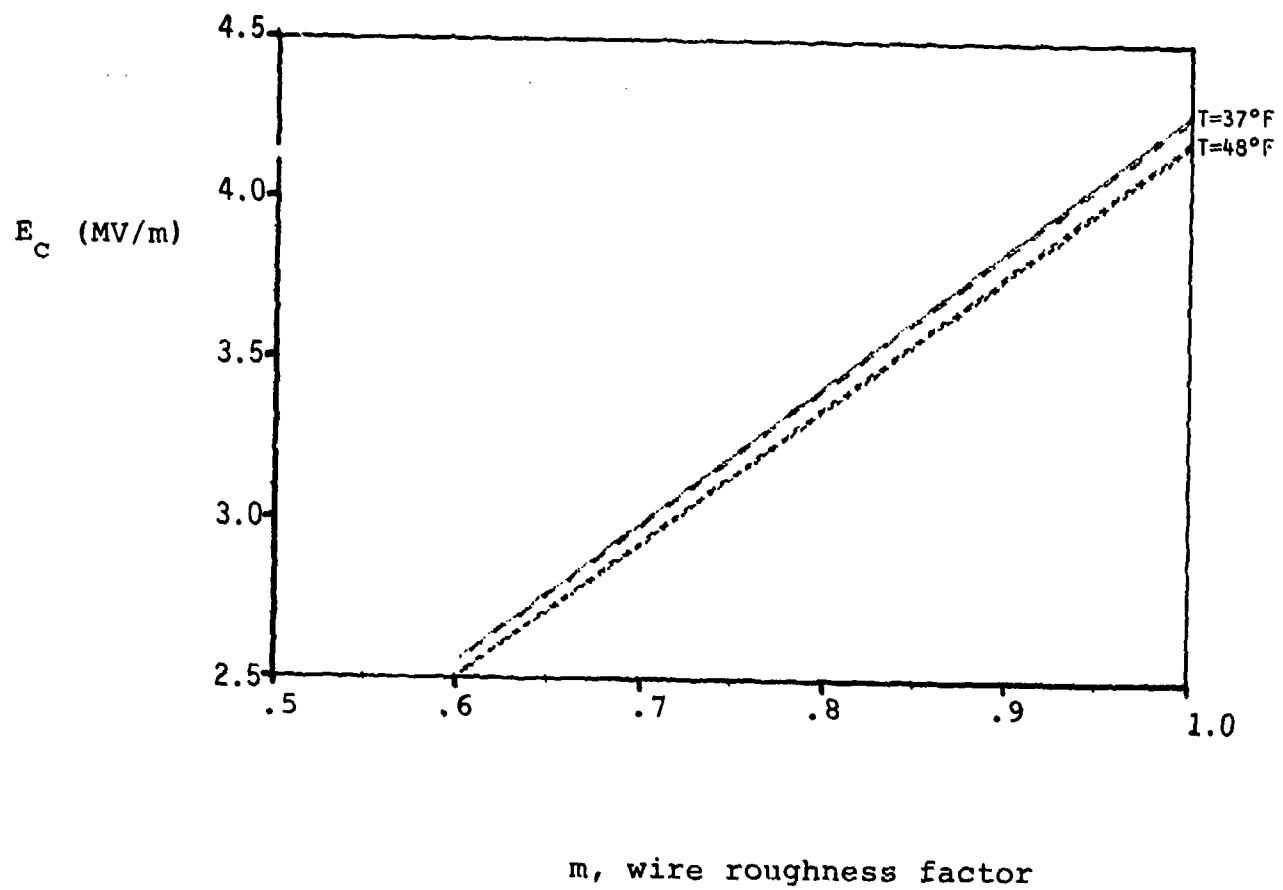
Figure 1. Breakdown Electric Field Strength as Predicted by Peek's Law [4,5] for $0.5 \leq m \leq 1.0$ on Baseline Test Date

large electrical currents may be induced on the wire. These currents, in fact, may be large enough to generate corona on the line, in much the same way large currents on power transmission and distribution lines do. However, because of the transient nature of EMP, the EMP induced corona is also short lived. Nevertheless, it may still reduce the amount of current induced on the line by the EMP.

Before presenting the details of this analysis, a description of an experiment performed to measure EMP induced corona effects is given in Section III. Several analytical models of the effects of EMP induced corona on the induced line current have been developed. These are discussed in Section IV. Following each discussion, the predictions of the analytical model are compared with experimental results. A separate sub-section then compares each model in terms of how well its predictions fit the experimental data. Finally, Section V presents concluding remarks and describes possible directions for future research.

III. DESCRIPTION OF EXPERIMENT AND BASELINE TEST CASE

In this section, a general overview of the experiment and the processing of the data, following its acquisition, are outlined. The baseline test case is described in this context.

A. Experimental Configuration

A pre-test survey of the EMP simulators available to conduct this experiment indicated the VPD-II at Kirtland Air Force Base in Albuquerque, New Mexico as the simulator with the most appropriate field and working volume. Since a common variable in at least three corona models (Baum [6], Townsend [7, 8], and conductivity [7] models) studied prior to performing this experiment was the angle of E-field incidence with respect to the conducting line, this experiment consisted of a test line suspended at various known angles with respect to the vertical electric field emitted by the VPD-II. Induced currents were measured with an in-line current derivative (dI/dt) sensor, designed by EG&G and designated an OMM-2 probe [9].

Other variables explored during this experiment included: test wire length, effective wire diameter, changes

in surface roughness, the addition of a dielectric sheath (insulation) to the test line, and variations in field strength of the pulse emitted from the VPD-II.

Figure 2 indicates the general configuration used in this test. A conducting line was suspended from VPD-II support pole #8 at a chosen height, H, and extended diagonally over the ground plane to a point located a distance, b, radially out from the base of the pole. The in-line current derivative sensor was located a distance, d, along this line from the ground plane intersection point. The local angle of incidence of the simulated EMP E-field with respect to the sensor is indicated by α .

The vertical component of the incident electric field in the vicinity of the current sensor on the line is shown in Figure 3. This was determined by measuring the horizontal component of the magnetic flux density, $\overline{B}$ (Figure 3a), and then multiplying by the speed of light, c, to obtain the electric field (Figure 3b). Measurements of the other field components indicated that they were at least a factor of 10 lower than the vertical electric field.

The baseline configuration chosen for comparison with corona model predictions in this report consisted of a 86.3 meter section of 1/8" diameter aircraft cable (7x19 stranding)

Baseline Values

H	=	30.1 meters
L	=	106.3 meters
d	=	12.0 meters
α	=	18°
a_1	=	1.07 cm
a_2	=	1.12 cm
b	=	101.9 m

Figure 2. General Test Configuration Used in Corona Experiment
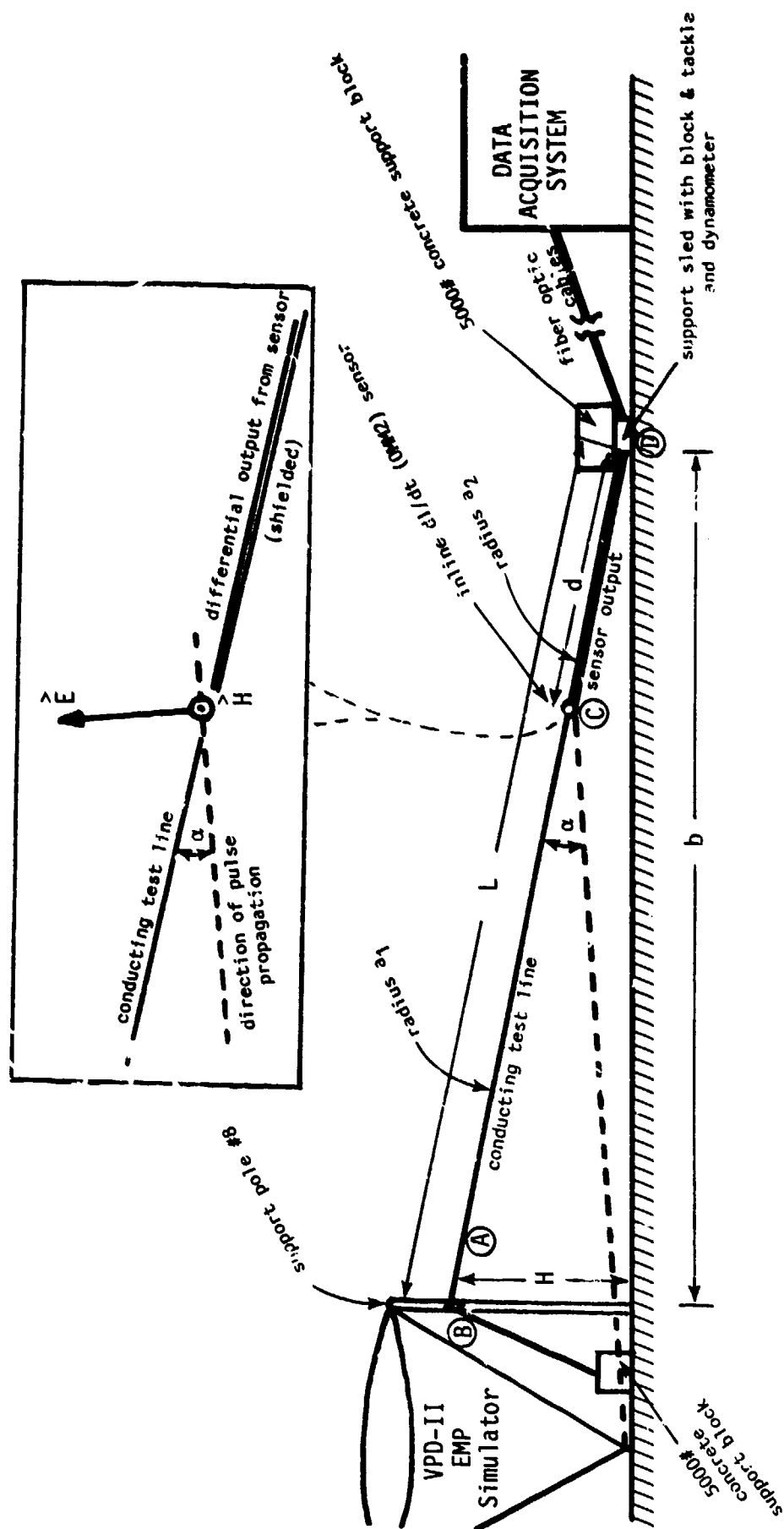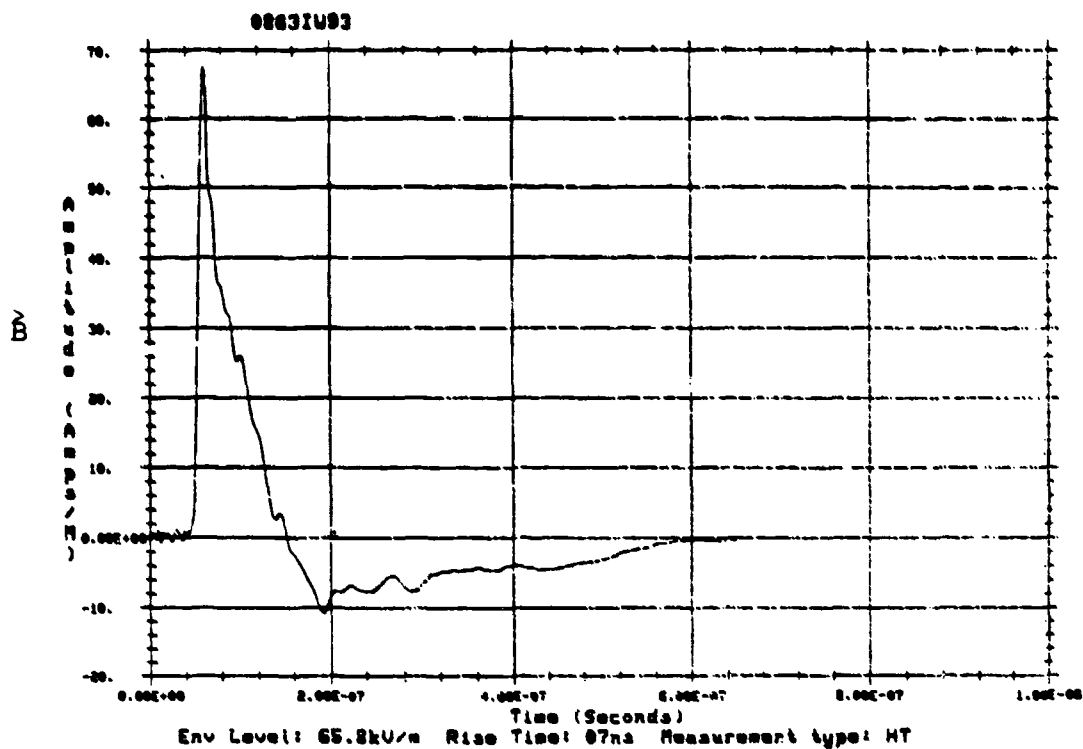
a. Horizontal component of $\vec{B}$ measured during baseline test
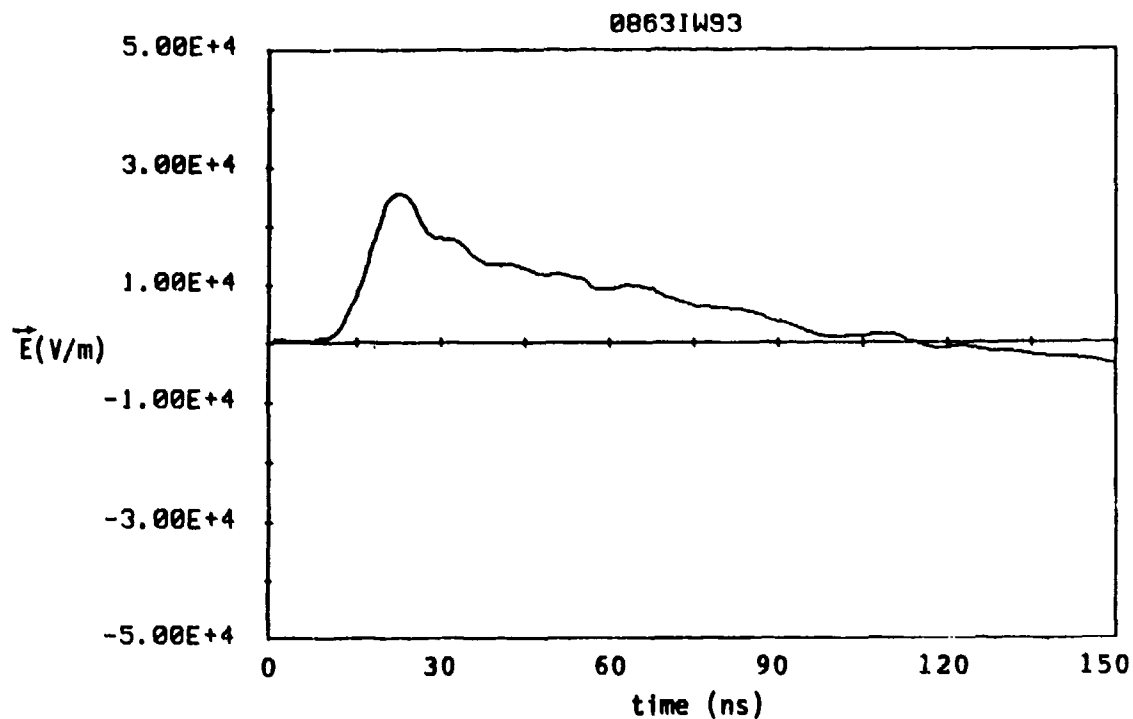
b. Conversion of measured horizontal component of $\vec{B}$ field to vertical Electric Field.

Figure 3. Plot of Field Measurement at Probe Location.

surrounded by a 1/2" PVC pipe covered with copper tape (OD = 0.840"). This was attached on one end (A) to an 8 meter dielectric standoff cable that was then attached to VPD-II's support pole #8 (B). The other end was attached, using standard fittings, to the OMM-2 current derivative sensor (C). The output from the sensor consisted of two type 141 semi-rigid coaxial cables providing a differential output, and an aircraft cable to provide a means for tensioning the entire test line without stressing the coax output cables. Tension on the test line was achieved using a block and tackle (D) attached to a support "sled" and was monitored with a dynamometer. In general, the tension applied was that required to make the line taut. Baseline values for the variables indicated in Figure 2 were:

$$H = 30.1 \text{ m}; \quad L = 106.3 \text{ m}; \quad d = 12 \text{ m}; \quad \alpha = 18° .$$

As discussed in reference [2], the test line was comprised of two sections. Above the probe, the line was a 1/8" diameter aircraft cable. Below the probe, there was a similar 1/8" cable to provide tension and two 141 semi-rigid coaxial cables to send the differential output from the probe down to a fiber-optic transmitter. These three conductors were then covered with a flexible plastic tube and a braided cylindrical conductor was then placed over the plastic tube. This resulted in an equivalent radius of approximately 1.12 cm for the

lower portion of the test line. This value is only approximate, due to the fact that the braided conductor did not form a perfect cylindrical slope as it fit over the plastic tube.

In an attempt to minimize the effects of having a discontinuity in the test line radius at the probe location, two different sizes of PVC tubing were covered with conducting copper tape and placed over the 1/8" aircraft cable on the upper portion of the line. For the nominal 1/2" PVC pipe, this increased the upper test line diameter to 0.84" and for the 1" PVC pipe, the diameter was 1.315".

For the baseline case reported in [2] and analyzed in the present report, the 1/2" PVC pipe was used in an attempt to minimize the discontinuity of the two radii of the line. Figure 4 contains plots of the data collected, both in derivative and in numerically integrated forms for the baseline case.

The differential output from the sensor was connected to a Nanofast 300-2A fiber optic transmitter. Fiber optic cables transmitted the signals to the data acquisition system (DAS), housed in a shielded trailer at the far end of the VPD-II working volume, where the signals were recorded on Tektronics 7912AD waveform digitizers.
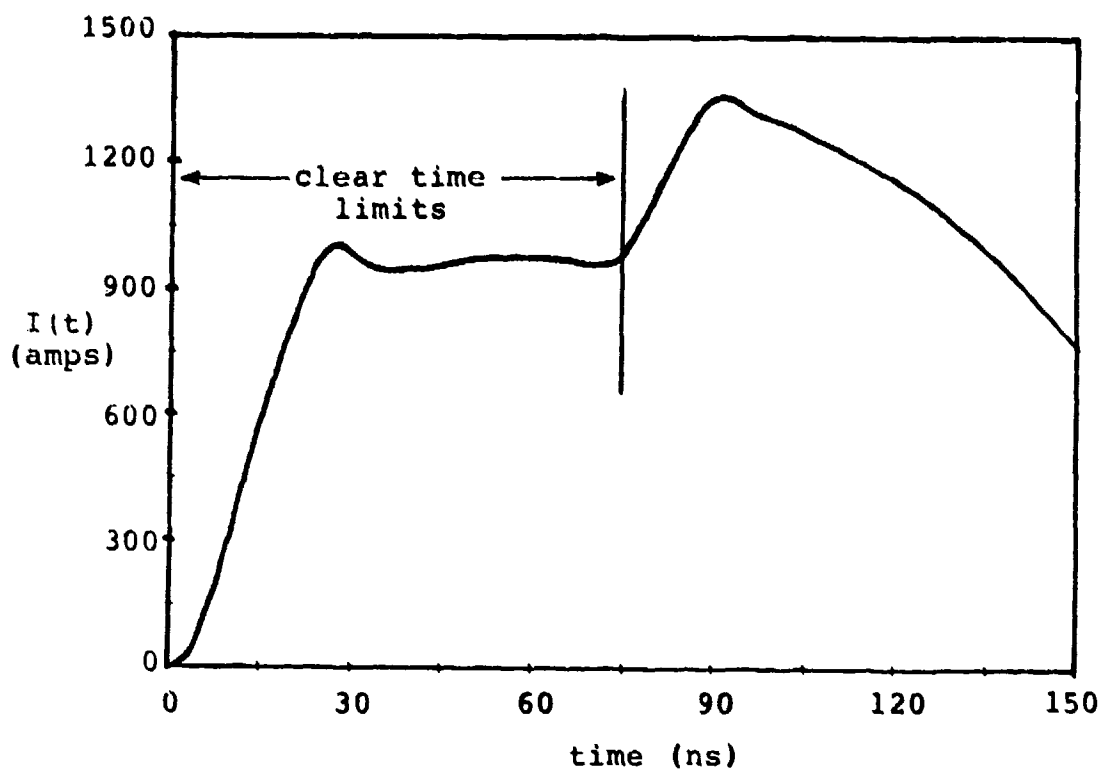
a. Numerically Integrated Form
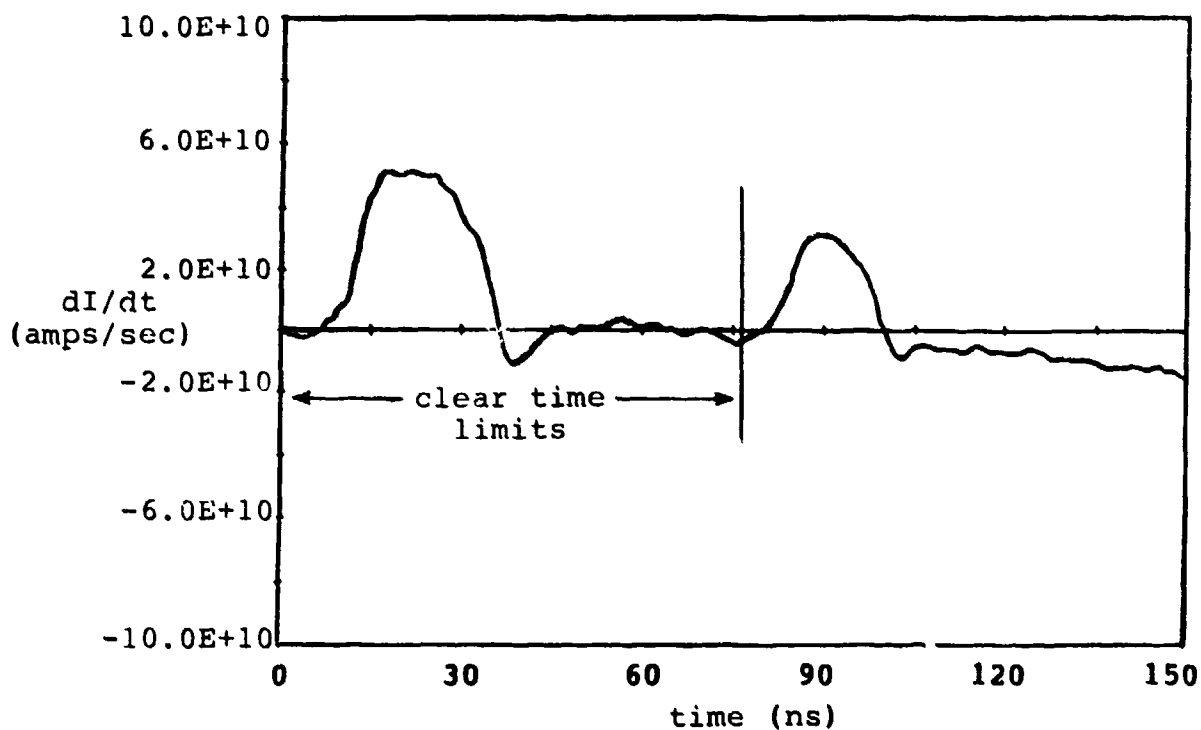
b. Derivative Form

Figure 4. Data Collected for Baseline Test Case During Corona Experiment.

15

Tests involving other configurations similar to that
of the baseline configuration explored the effects of
increasing and decreasing the effective wire radius and
changes in angle of E-field incidence. Variations with
radial angle and tension were also examined. The case
chosen as a baseline test for the purpose of the comparisons
in this paper was selected for three reasons: (1) variations
tested during this experiment examined both increased and
decreased effective test wire radius as well as angles of
incidence higher and lower than that of the baseline, (2) in
the baseline case, the test wire radius was the same as the
radius of the OMM-2 probe, eliminating concerns related to
possible discontinuities at the probe boundary, and (3) the
diameter is representative of a realistic power system con-
ductor. In fact, no reflections were noted at that boundary
during any of the testing. Further details of configuration
variations are contained in Reference [2] and [3].

In examining the measured data, it is important to
realize that there are several perturbations to the response
which arrive at the probe location at certain times. Figure 5
shows the simulator and wire geometry. The first response
at the probe is due to a direct interaction of the line with
the incident field traveling from the pulser to the probe
along Path #1. Later, first order diffraction effects due
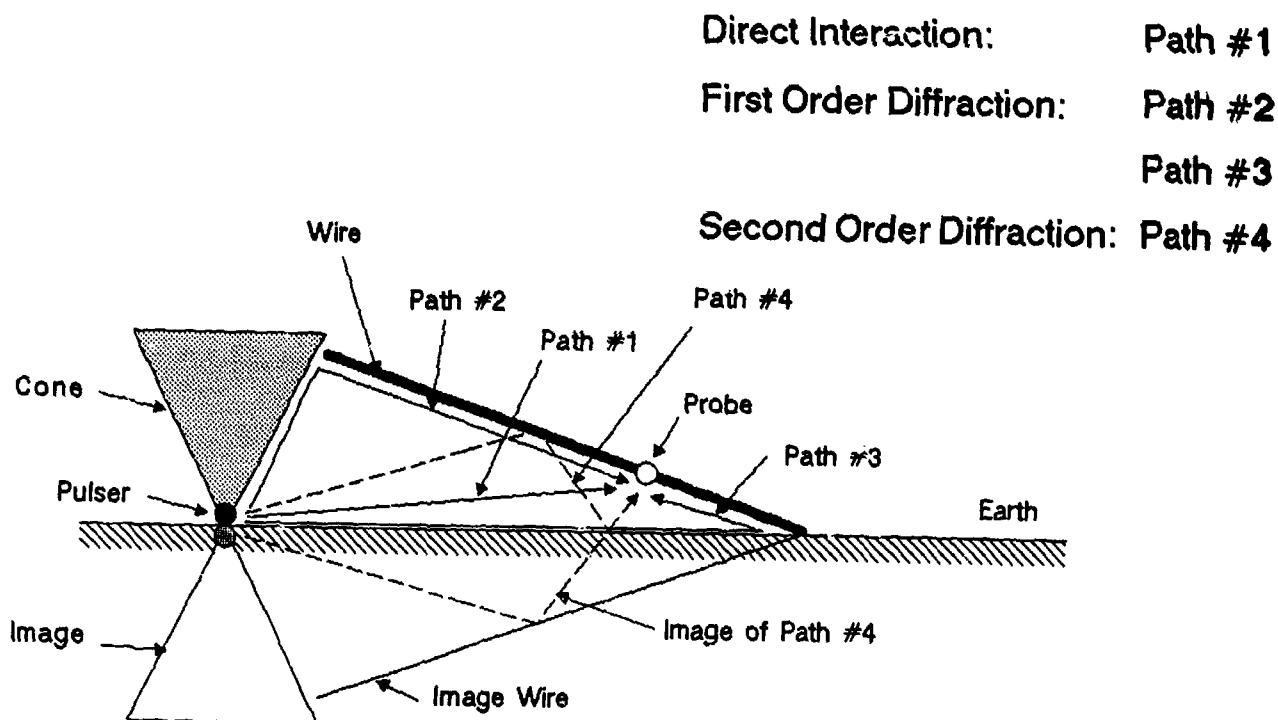
Figure 5. Clear Times for Various Diffraction
Components for the Corona Test.

to a wave propagating up the simulator cone and then down the wire (Path #2) and along the ground and up the wire (Path #3) will be noticed. Calculations were made prior to the experiment to try to maximize the clear time (i.e., the time during which the line response is identical to that of an infinite line) and the optimum probe location was determined.

It should be noted in passing that there is another diffraction component which affects the response of the line current, although it is of second-order importance. This is shown as Path #4, which involves the incident field diffracting from the wire, reflecting specularly in the earth, and then impinging on the probe. This particular diffraction component arrives at a time earlier than the components from Paths #2 and #3, but is believed to have a negligible effect on the measured current. A future research effort should include the determination of the importance of this diffraction term.

During the test, it was found that the major clear time limiting factor was the reflection noted from the metallic sled used in tensioning the line from the ground end. In general, the 12 meter output from the sensor allowed sufficient clear time to demonstrate corona dependent effects. Clear time limitations in the measured data are indicated on

each of the data plots in Figure 4, as well as in later plots comparing the measured data with predictions made by each of the corona models studied in this report.

B. Data Processing Concepts

The differential output from the OMM-2 probe was attached to a fiber optic transmitter containing a balun for common mode rejection. The measured signal was then sent over fiber optic cables to the data acquisition system, housed nearby in a shielded trailer. At that point, the signal was temporally split, using an active signal divider, and passed to waveform digitizers such that there was a 5 to 10 nanosecond overlap of data in successive digitizers. This overlap allowed the data to be later aligned and connected on a common time scale (a process called "time-tying" the data). After the data was recorded on the waveform digitizers, it was transferred to the TRESTLE VAX / 11-750 computer for subsequent processing by BDM.

The data processing techniques discussed below apply to a collection of data sets representing the line's response to a single VPD shot. The term "subsequent data set" means the set of data recorded by a single waveform digitizer that is

temporally next to (and overlapping with) the data set just considered.

On the VAX 11-750 , the data was linearly scaled to correct for non-frequency dependent instrumentation effects. Data from the first digitizer was also corrected for any obvious DC offset. The assumption made in the DC offset correction is that in the absence of any excitation the mean of the line response data should be zero.

Next, data from subsequent digitizers is time-tied with that from earlier digitizers. Beginning with the tail of the first set of data and the head of the second set of data, contemporaneous sections of data are compared and blended through averaging and offsetting the data as necessary. Note that the DC correction, applied only to the earliest data set, is passed through subsequent data sets without requiring a priori knowledge or correction of the exact DC offset of those later data sets. This DC offset adjusted, scaled, and time-tied data is referred to as the raw data.

Raw data may still contain some frequency dependent instrumentation bias. If the transfer function of the combined effects of all instrumentation does not differ significantly from a constant value, its deconvolution may be

performed in the time domain by further scaling of the data by the amount of that constant. However, if the frequency dependencies are critical, it is easiest to deconvolve them in the frequency domain. Here, a Fourier integral transform was used to convert the time domain data to the frequency domain and back to the time domain following deconvolution of instrument effects. Frequency domain transfer functions for each indicated piece of equipment consisted of 50 points per decade over the three decade range 250 kHz to 250 MHz and were obtained using a Hewlett Packard 8505A Network Analyzer calibrated to NBS standards by Precision Measurement Equipment Laboratory (PMEL).

C. Measurement Equipment

Table I contains a list of the major equipment used to conduct this experiment.

A. TEST LINE
    1/8" (diameter) aircraft cable (7x19 stranding).
    1/8" aircraft cable with 1/32" thick PVC coating.
    1/2" (inner diameter) schedule 315 PVC pipe.
     1" (inner diameter) schedule 200 PVC pipe.
    Copper tape added to exterior of all PVC pipes.
    EG&G OMM-2 Differential current probe
    EG&G DMB-1 (differential mode balun)
    Tinned copper grounding braid.

B. DATA ACQUISITION
    Tektronics 7912AD Waveform Digitizers with plug in
    modules:
        Tek 7A16P Programmable Amplifier
        Tek 7B90P Programmable Time Base
    Nanofast 300-2A Fiber Optic Link - Transmitter
    Hewlett-Packard 11549A Power Splitter
    Tektronics 7104 1 GHz Real Time Oscilloscope &
    modules:
        Tek 7A29 Dual Trace Amplifier
        Tek 7B15 Delta Delaying Time Base
    EG&G ODL-6 Fiber Optic Link - Receiver

C. MISCELLANEOUS
    Omni-Spectra 2082-6013-20 20 dB attenuators
    EG&G MGL-2 B-dot sensor (for field mapping)

Table I. Major Equipment used in Corona Experiment

D. Limitations of the Experiment

It should be noted at this point that there were limits
to what could be examined in the course of the experiment.
Furthermore, the analysis contained below is limited since
it examines the predictions of each analytic model against a
single baseline test case, selected from the full set of
acquired data for the reasons discussed earlier.
Consequently, the reader may be aware of two kinds of
limitations: those arising from limits in what could be
tested during the course of the experiment and those arising
from the use of a single, representative baseline test case in
evaluating the models discussed below. Such limitations are
inherent in nearly every experiment and in nearly every
comparison of analytical results with experiment data.

Limitations on the experiment included limitations
posed by the capabilities of the EMP simulator used, as well
as those created by the geometry chosen for the experiment.
The incident field effectively had a fixed form with a
constant rise time. Consequently, the induced current had
essentially a constant rate of rise. Different waveforms may
have an impact on the corona inception voltage, but there is
no data from this experiment that clearly supports or negates
this notion. Given the full set of acquired data [2, 3], one

might be able to make tentative conclusions about the corona inception voltage, but such conclusions would be inappropriate in this paper due to the limited nature of the single baseline test case. However, simulator limitations restricted the variations in the pulse shape used during the experiment. Consequently, even the full set of acquired data may be inadequate for full determination of the relation of the corona inception voltage to the pulse risetime.

There are two polarities for the EMP that could be tested to determine the difference in their impact. However, the pulser of the simulator could only be charged in one way, resulting in an E-field that generated a positively charged wire. In addition, energizing the test line (to give it electrical characteristics similar to either an AC or a DC transmission line) might also impact the results noted. Again, we have no data to support or negate these ideas. They are presented here to emphasize the limitations of what might be inferred from the data.

Reflections of an EMP from the ground plane such that its initial interaction with the test line is followed 60-100 nanoseconds later by the interaction of the reflected EMP with the test line were not tested because both the simulator and the experiment geometry could not accomodate such a test.

The reflected pulse, which is likely to occur as a result of an EMP resulting from a nuclear weapon detonation, can be expected to also alter the results obtained. However it will be noted that none of the models investigated here considered this reflected EMP either. Although the reflection is likely to occur in an actual EMP event, the magnitude of its impact on a given transmission line is strictly a function of the local geometry. Later revisions to corona models n ay include considerations of the impact of the pulse reflection in terms of the local geometry. The consideration of the reflected EMP is beyond the scope of the current investigation.

Although a number of attempts were made during the experiment to obtain "no corona" data [2,3], the effect of corona was noted in every test run. However, in some of these attempts, the reduction in corona impact was sufficient to indicate a general notion of what "no corona" data should look like. A comparison of the baseline test data with analytical "no corona" data is included in Figures 12-20.

IV. COMPARISON OF MEASURED DATA WITH CALCULATIONAL RESULTS

A. Overview

The study of the effects of corona discharge on power system conductors has been a subject of considerable interest for a number of years. This interest stems from corona's role in creating radio frequency interference, in adding power loss on electrical transmission lines, and in modifying the shape of lightning-induced transient surges along power lines. A number of authors [5], [10], [11], and [12] have studied corona related effects which are frequently described as arising from a changing conductor capacitance ar ` a corona resistance which accounts for loss in the corona.

In the recent literature, there are a number of articles which describe corona models for power lines or other above-ground conductors [13], [14], and [15]. All of these models make the assumption that the propagation of voltage and current waves on the line can be described by TEM transmission line theory, with suitable modifications being made in either the source terms or in the transmission line parameters to account for the behavior of the corona.

Although this previous work aided in the development of corona models, its application was primarily intended for the study of point-injected signals, such as that form a lightning attachment to the line, and their subsequent propagation characteristics. Other early corona models examined corona resulting from high voltages being carried on the lines. Neither of these forms of corona model were directly applicable to the case of EMP induced corona.

In the EMP area, it is important to understand the behavior of a distributed field excitation of a line as well as the effects that EMP-induced corona will have on the line current. There have been a number of recent papers which describe models for computing this phenomena [6], [7], [16], [17] and [18]. As in the previous cases of surge propagation in the presence of corona, most of these models invoke the transmission line approximation for obtaining a solution for the line response, but with a distributed field excitation. Investigations have indicated that such transmission line solutions can be quite accurate in describing the transient current behavior as illustrated in Figure 6.

An alternate, but closely related calculational approach is described in reference [7] which employs an antenna solution for the corona coupling problem. This and the other transmission line coupling models will be described in more detail in the following section.
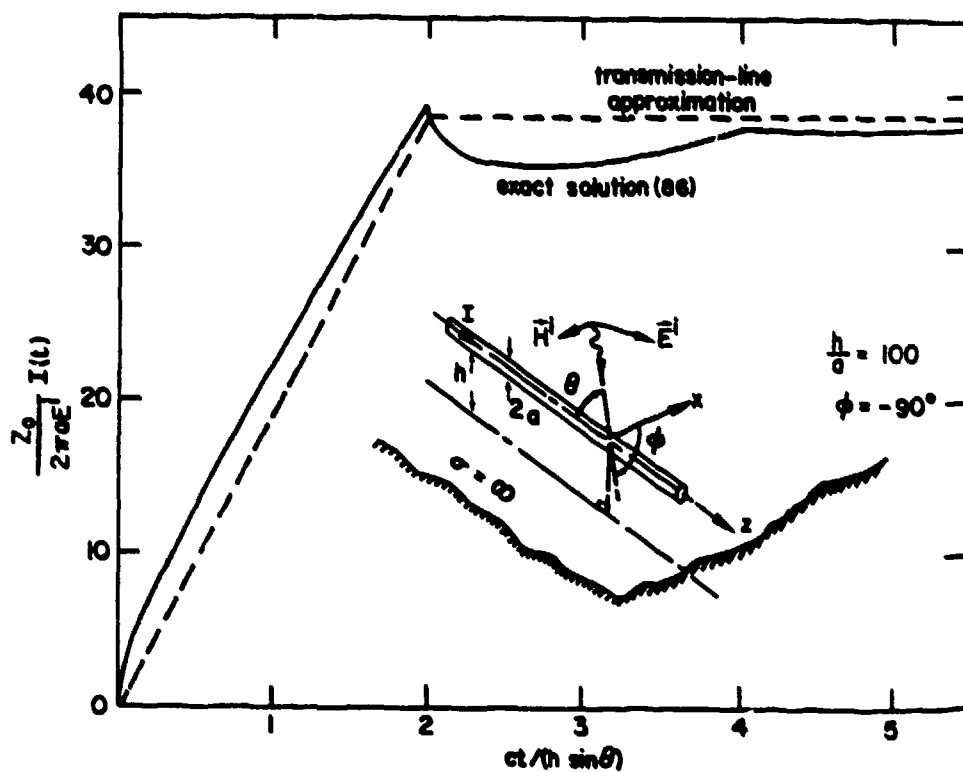
Figure 6.   Current Induced on an Infinite Conductor
Over a Perfectly Conducting Ground Plane
by a Step-Function Incident Wave (Trans-
verse Magnetic Field) [25].

In the corona models to be discussed, there are several parameters which describe the corona behavior and its effect on the line response. Frequently, the precise values for these corona model parameters are not known from first principles. However, it is believed that they can be determined by comparing computed data with experimental results.

One common parameter in these models is the air breakdown electric field strength, E_c, which is usually taken to be a constant. E_c is considered to be independent of the rate of rise of the local electric field normal to the conductor, which is the ultimate ionization field for the air surrounding the conductor. It may be noted that in several of the models studied, better fits to the data have been found using values for E_c larger than the range of values predicted by Peek's law. Possible reasons for this may include: (1) There is a lag between the time when the local field equals or exceeds E_c and the time when the impact of corona formation is noted in the conductor response. This time is required for appropriate numbers of separated electron-ion pairs to form. If the driving waveform has a magnitude higher than E_c and risetime slightly longer than the corona establishment time, then the time delay in corona establishment could be seen in the data as an artificially high E_c. Reference 4 indicates that the establishment time consists of a statistical lag time, which is dependent on geometry and gas characteristics, and a

formative lag time (about 1 nanosecond). In this particular experiment, the statistical lag time depends on the time for the electron to detach from an O_2^- ion in the region in which the electric field exceeds E_c [20]. (2) Peek's law as stated in [4] is valid only from DC to several kiohertz. The driving waveform contains higher frequencies, although the bulk of its energy is in the lower frequencies. The impact of the higher frequency components may be to raise the effective E_c, although there is evidence [19, p. 4-136] contrary to this notion.

In this section, the measured EMP-induced response of a wire excited strongly enough to produce a corona along the conductor is compared with 5 different corona models. All of there models involve corona parameters which must be "fit" to a particular set of measured data, then used to predict the response of the line to other excitations.

This section is divided into several sub-sections. Each of these will describe one of the previously referenced corona models and compare the corresponding computed line responses with the measured results which are described in refernece [2]. From this study, a suggestion as to the "best" corona model for EMP predicitons can be made.

B. The Baum Corona Model

1. Theory

The model proposed by Baum [6] for the EMP excitation of a conductor is similar to previous corona models used within the power community for computing the propagation of lightning surges along a line. However, in the EMP case, a set of distributed excitation sources along the line is required. In this model, a voltage-dependent conductor radius is used to represent the effects of the corona, and the conductor is assumed to be located in free space or above a reference ground plane at a height, h (Note that Baum's model describes a conversion between a conducting line above a ground plane and an analogous coaxial line.). The response of the line is computed by transmission line equations in which the line current and voltage (with respect to the ground plane) are unknowns:

$$\frac{\partial V}{\partial z} + L' \frac{\partial I}{\partial t} = V'_s \qquad (1a)$$

and

$$\frac{\partial I}{\partial z} + \frac{\partial}{\partial t}(C'V) = I'_s \quad .$$ (1b)

In this expression, $I(z,t)$ is the induced current on the line and $V(z,t)$ is the voltage of the line. The term L' is the per-unit-length inductance of the line, and this is assumed to be independent of the presence of corona on the line. For the case of a line of radius a_w located over a ground at a height h , this inductance is given by

$$L' = \mu_o f_{go} \quad ,$$ (2)

where the parameter f_{go} is given by

$$f_{go} = \frac{1}{2\pi} \cosh^{-1}(h/a_w)$$ (3a)

$$\approx \frac{1}{2\pi} \ln (2h/a_w)$$ (3b)

The term C' is the per unit length capacitance of the line. In the Baum model, this is assumed to depend on the nature of the corona. Normally, this parameter is given by

$$C' = \epsilon_o/f_{go}$$ (4)

for the case of a wire without corona. With corona, however,

Baum's model assumes that the wire radius is effectively increased, due to the presence of the ionized cloud surrounding the wire. Consequently, the per unit length capacitance is modified. The new capacitance is given by

$$C' = \epsilon_o / f_{gc} \quad , \tag{5}$$

where f_{gc} has the same form as in equation (3), with the radius of the wire, a_w , being replaced by the effective radius of the corona region, a_c .

This corona radius is estimated by determining the radius away from the wire at which the local electric field just exceeds the air breakdown field strength. Denoting this breakdown field by E_c , the radius of the corona region can thus be expressed in terms of the charge per-unit-length on the conducting wire, Q' , as

$$a_c = \frac{|Q'|}{2\pi \, \epsilon_o \, E_c} \quad . \tag{6}$$

The line capacitance is given, therefore, by the nonlinear relation

$$C'(Q) = \epsilon_o / (\text{minimum } [f_{go}, f_{gc}(Q)]) \quad , \tag{7}$$

which depends on the local charge on the line, as well as on the air breakdown strength.

For the case of an isolated wire in free space, the i-v relations of equations (1a) and (1b) are still assumed to hold, but the definition of the line inductance in equation (2) and the line capacitance in equation (4) becomes ill-defined, due to the lack of a reference conductor in the problem. In this instance, the parameter f_{go} (or equivalently, the line "height", h) may be regarded as a fictitious line constant and varied in order to obtain a good fit of the computed data with that obtained from experiment. Note that the response of the line depends on h only logarithmically, so as a consequence, the response is not extremely sensitive to the choice of this parameter.

The source terms in equations (1a) and (1b) are related to the incident field exciting the line. The term V_s' is related to the per-unit-length magnetic flux linking the conductor and the reference conductor, and the term I_s' is related to the charge deposited on the conductor due to the incident electric field.

In reference [6], Baum illustrates how these equations can be re-arranged to yield two coupled equations for the line current and charge, with the source term related to the incident tangential electric field on the wire, E_t . This form is completely equivalent to the previous equations, and is expressed as

$$\frac{\partial}{\partial z} (Q'/C') + L' \frac{\partial I}{\partial t} = E_t \tag{8a}$$

and

$$\frac{\partial I}{\partial z} + \frac{\partial Q'}{\partial t} = 0 \quad . \tag{8b}$$

By defining a new variable $v(z,t) \equiv Q(v,t)/C'(Q)$, it is possible to convert equations (8) into the following "standard" form, which will be useful in comparing this corona modeling approach with other models:

$$\frac{\partial v}{\partial z} + L' \frac{\partial I}{\partial t} = E_t \tag{9a}$$

and

$$\frac{\partial I}{\partial z} + \frac{\partial}{\partial t}(C'v) = 0 \quad . \tag{9b}$$

35

Note that although the variable v has the dimensions of volts, it is not the total voltage between the line and the ground which is being induced by the EMP. This latter response is computed by adding the contribution of the vertical component of the incident electric field as described in [4].

It is the set of equations in (9) that must ultimately be solved for the line current, I . This solution may be carried out using the usual time-marching, finite-difference approach, or by a method reminiscent of the method of characteristics [21], as done by Baum.

In applying this corona model to the experimental data described in Section II, it is noted that there are two independent parameters which can be varied in order to optimize the computed solution. These are the electric field breakdown strength in air E_c , and the value of f_{go} in equation (3) which can be interpreted as fixing the value of the parameter h .

Considering the geometry for the baseline experimental case as defined in Section II, corona coupling calculations using the Baum model have been conducted for a variety of different values of E_c and f_{go} , and the results are presented in figures 7 through 20.
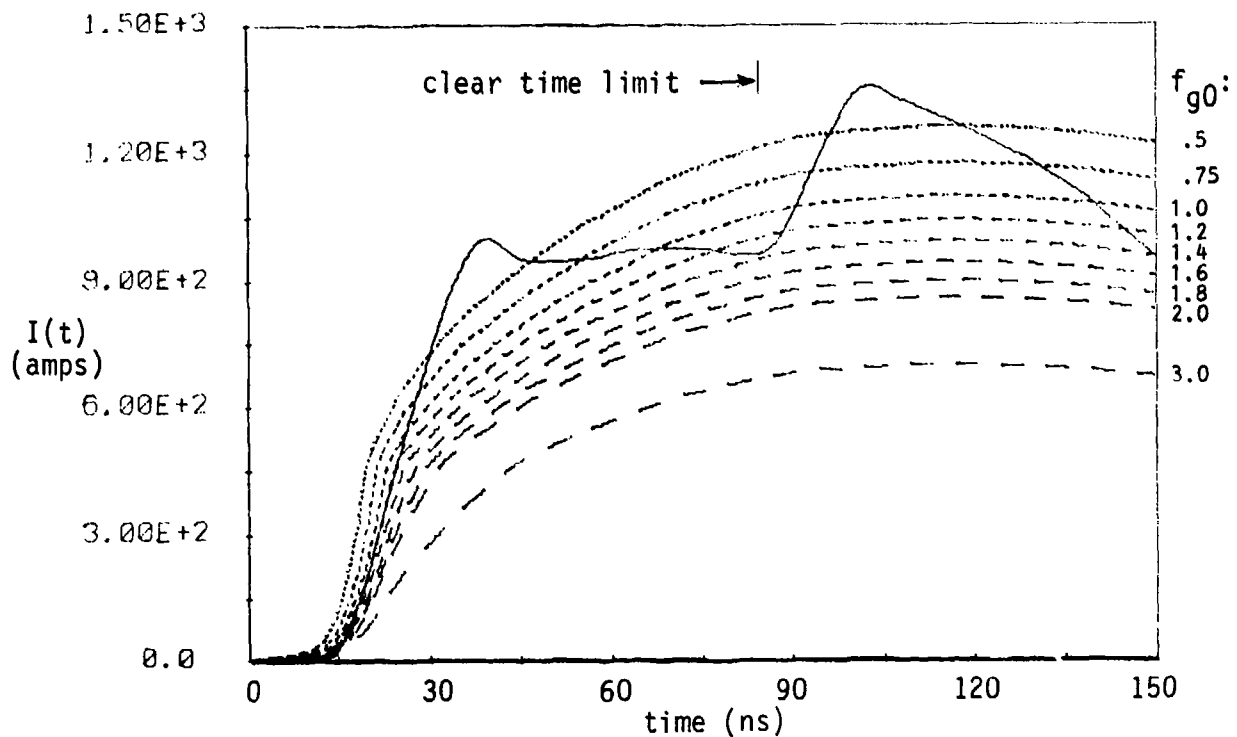
Figure 7. Comparison of Measured (——) and Baum Corona
Model (- - -) Results:
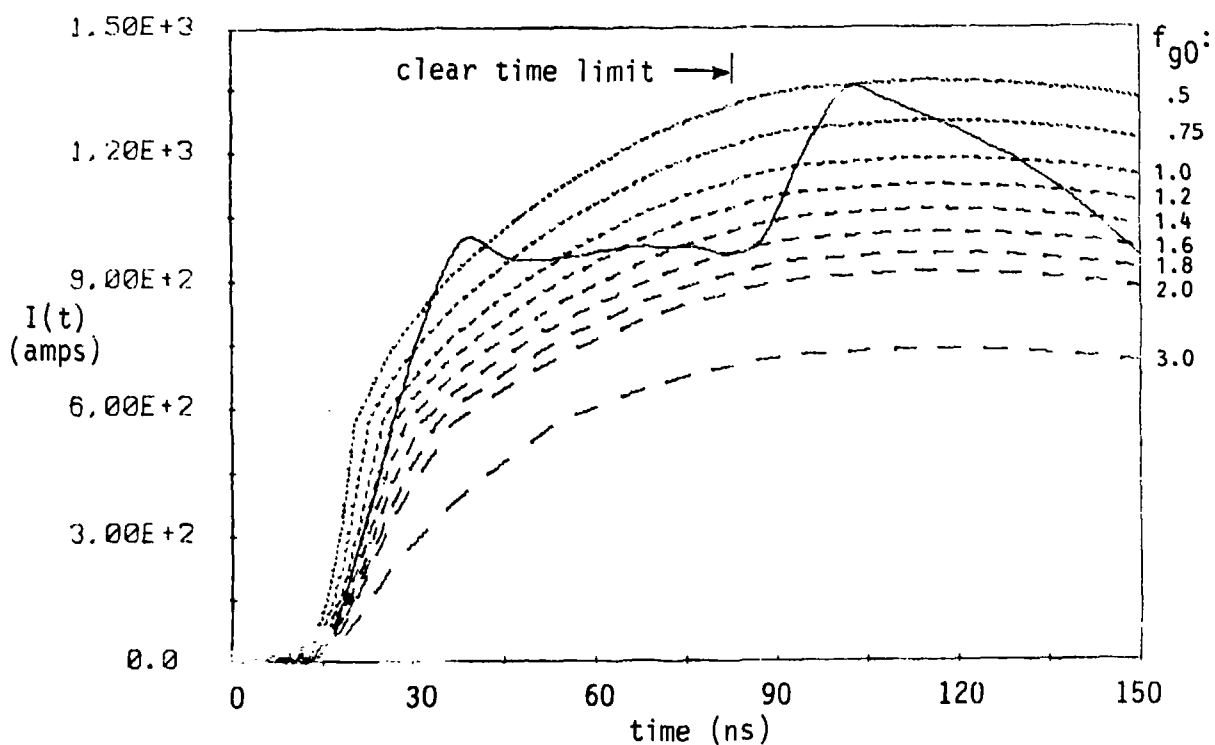
$E_c = 2.5$ MV/m; f_{g0} Variations as Indicated

Figure 8. Comparison of Measured (——) and Baum Corona
Model (- -   Results:

$E_c = 3.0$ MV/m; f_{g0} Variations as Indicated

37

Figure 9.   Comparison of Measured (——) and Baum Corona
Model (---) Results:

E_c = 3.5 MV/m; f_{g0} Variations as Indicated

Figure 10.   Comparison of Measured (——) and Baum Corona
Model (---) Results:

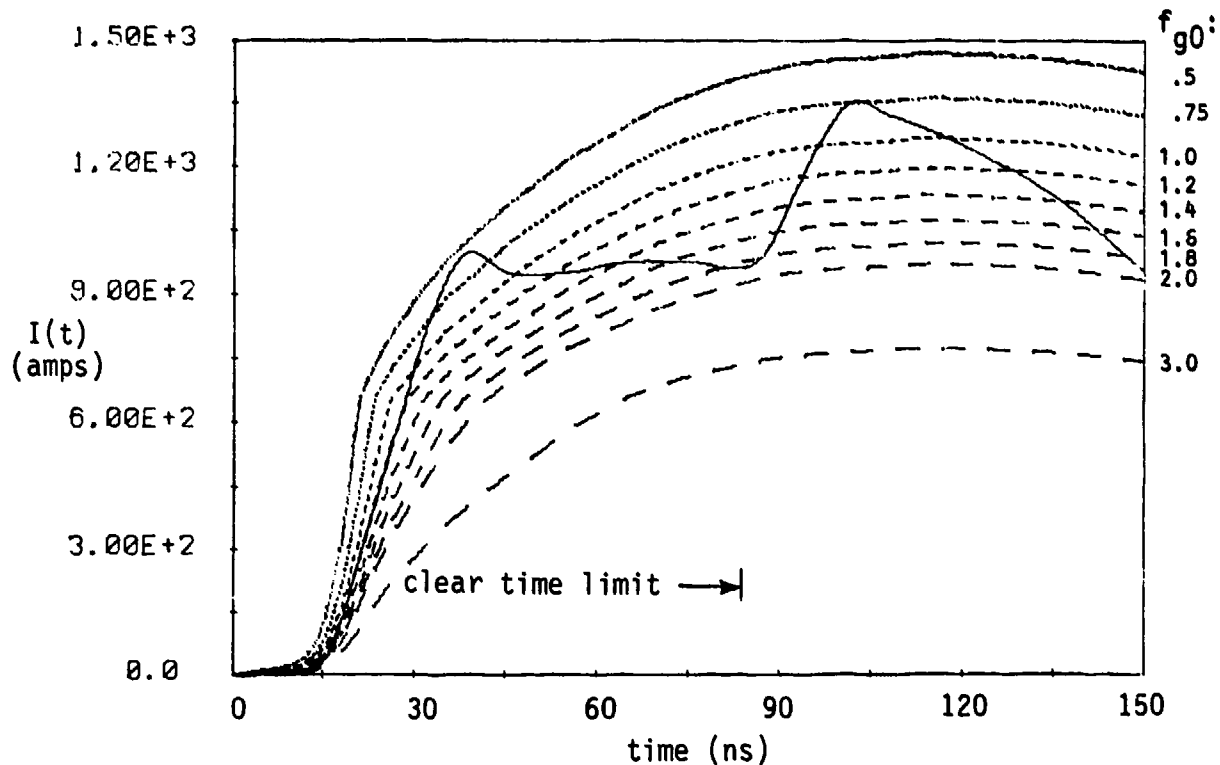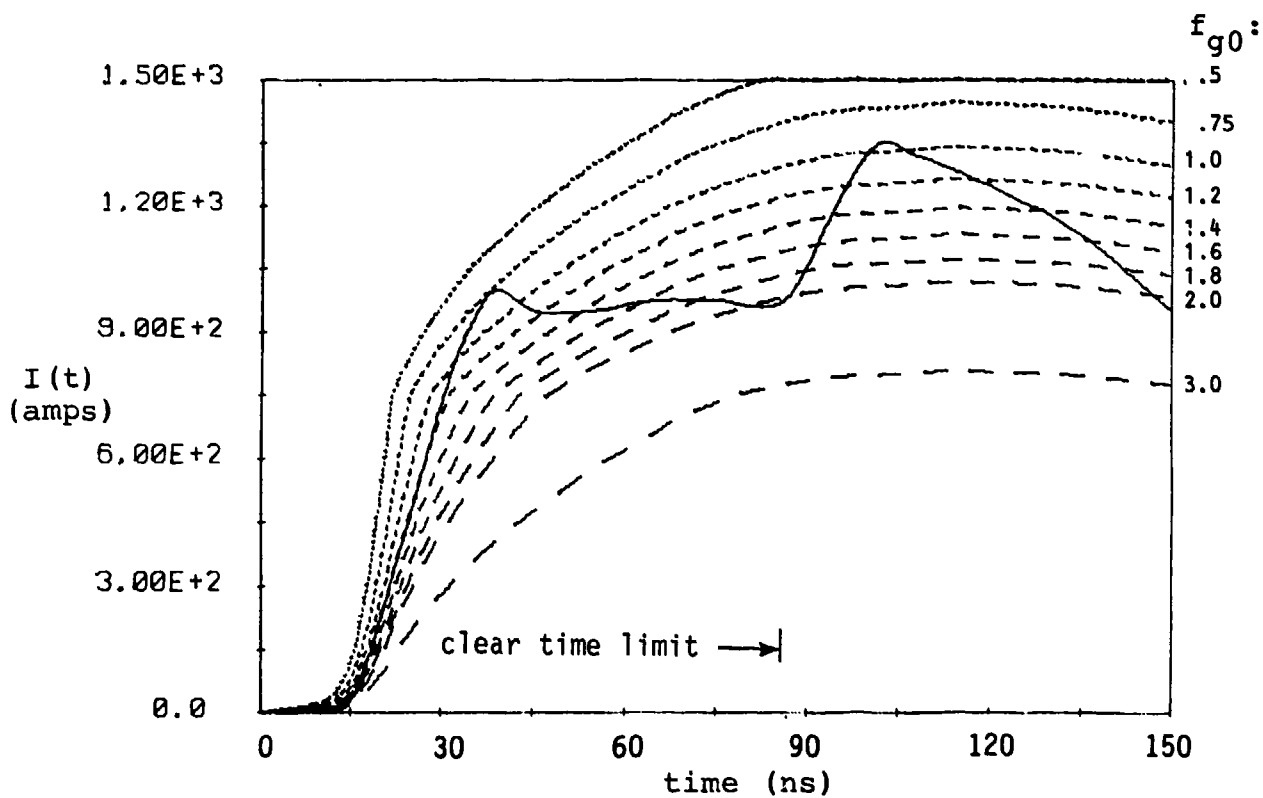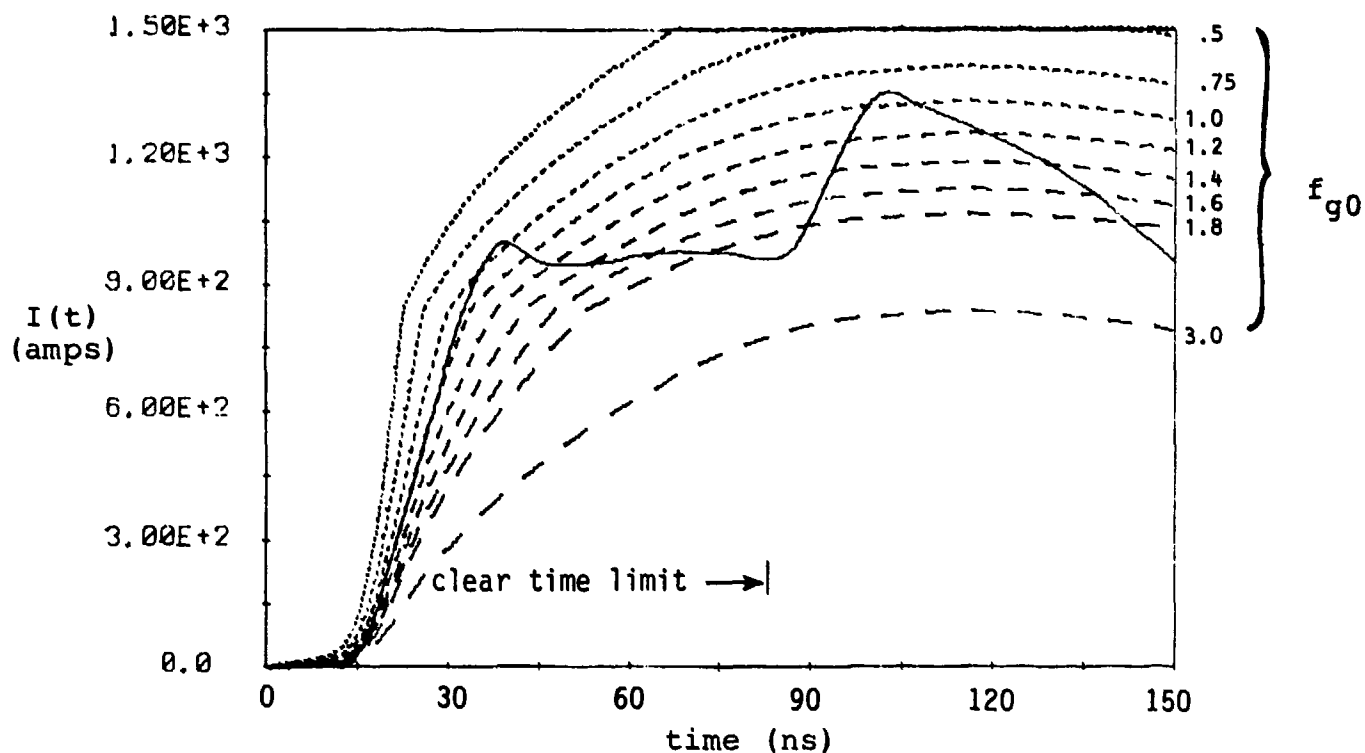E_c = 4.0 MV/m; f_{g0} Variations as Indicated

38

Figure 11. Comparison of Measured (——) and Baum Corona
Model (---) Results:

E_c = 4.5 MV/m; f_{g0} Variations as Indicated

Figure 12. Comparison of Measured (——) and Baum Corona
Model (---) Results:

f_{g0} = 0.5; E_c Variations as Indicated

39

Figure 13. Comparison of Measured (——) and Baum Corona Model (---) Results:

$f_{g0} = 0.75$; E_c Variations as Indicated

Figure 14. Comparison of Measured (——) and Baum Corona Model (---) Results:

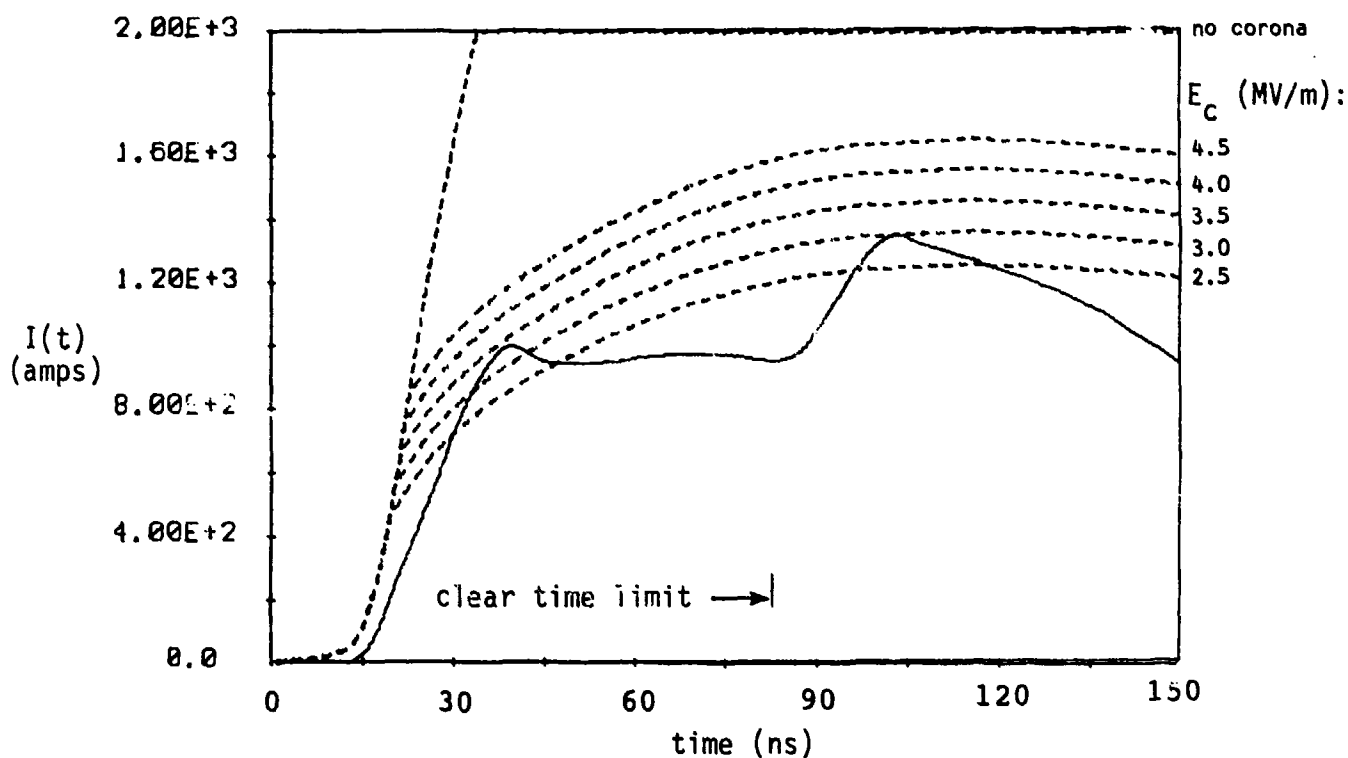$f_{g0} = 1.0$; E_c Variations as Indicated

Figure 15. Comparison of Measured (———) and Baum Corona
Model (---) Results:

$f_{g0} = 1.2$; E_c Variations as Indicated

Figure 16. Comparison of Measured (———) and Baum Corona
Model (---) Results;

$f_{g0} = 1.4$; E_c Variations as Indicated

Figure 17.   Comparison of Measured (———) and B. ʌm Corona
Model (---) Results;
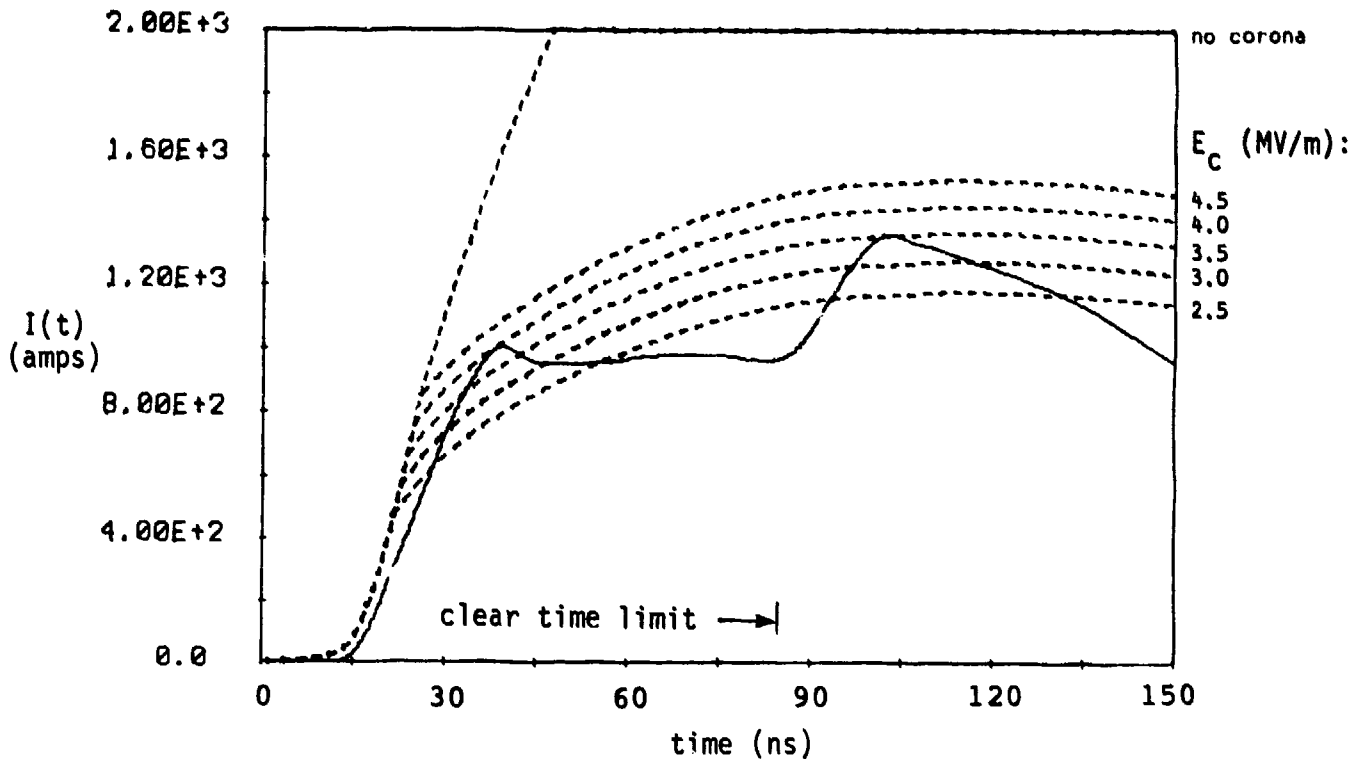
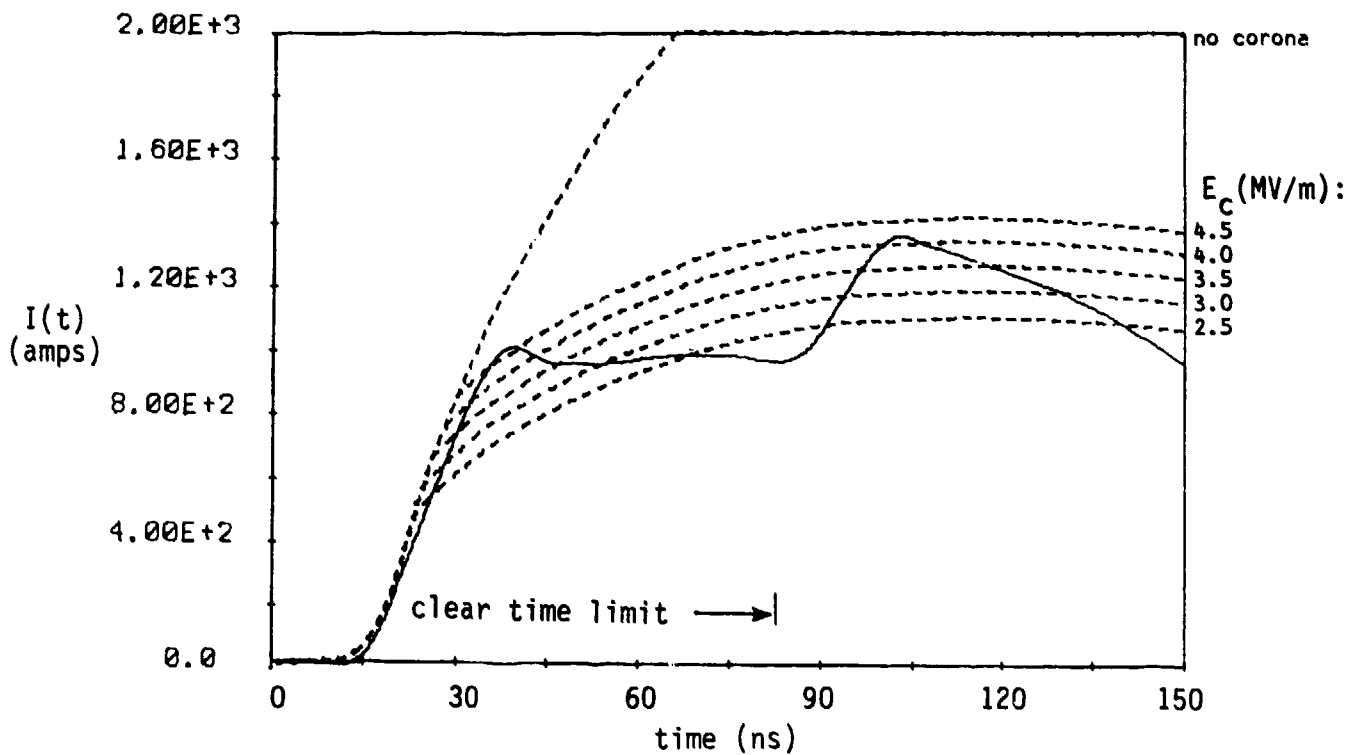f_{g0} = 1.6; E_c Variations as Indicated
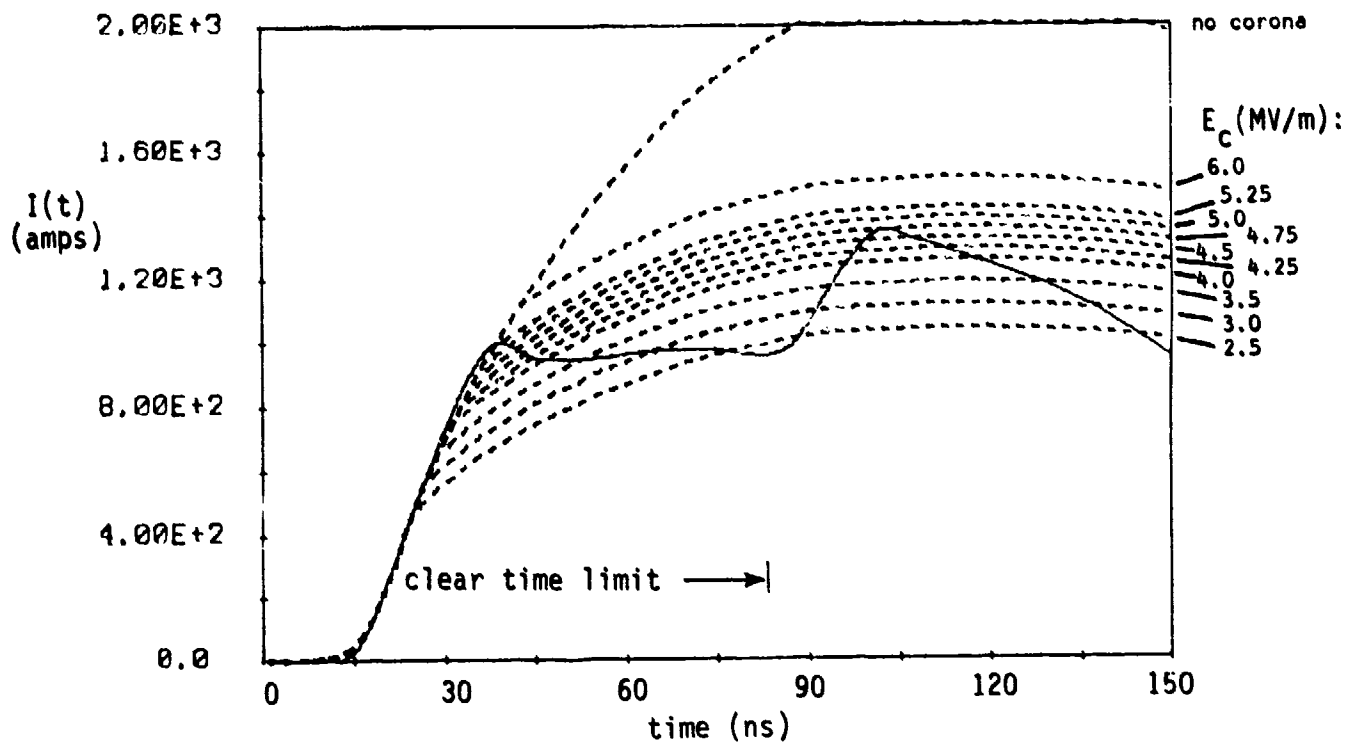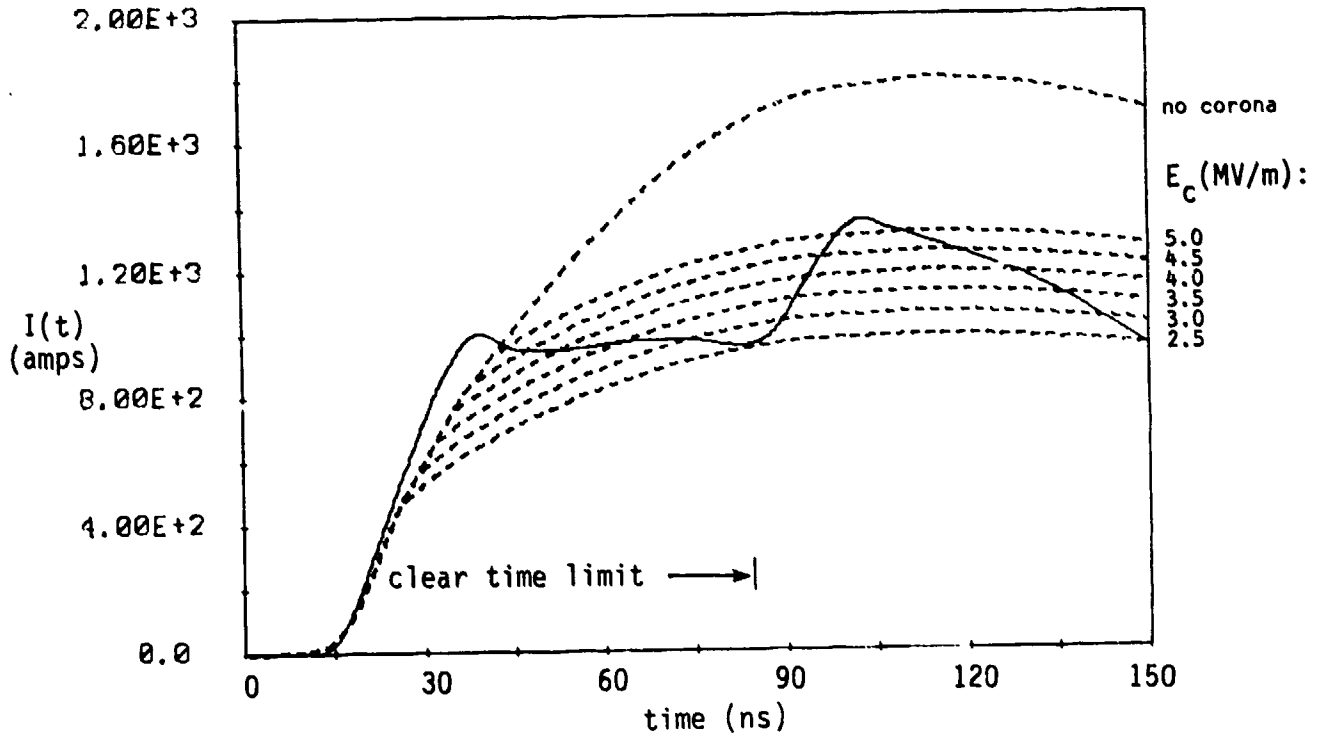

Figure 18.   Comparison of Measured (———) and Baum Corona
Model (---) Results:

f_{g0} = 1.8; E_c Variations as Indicated
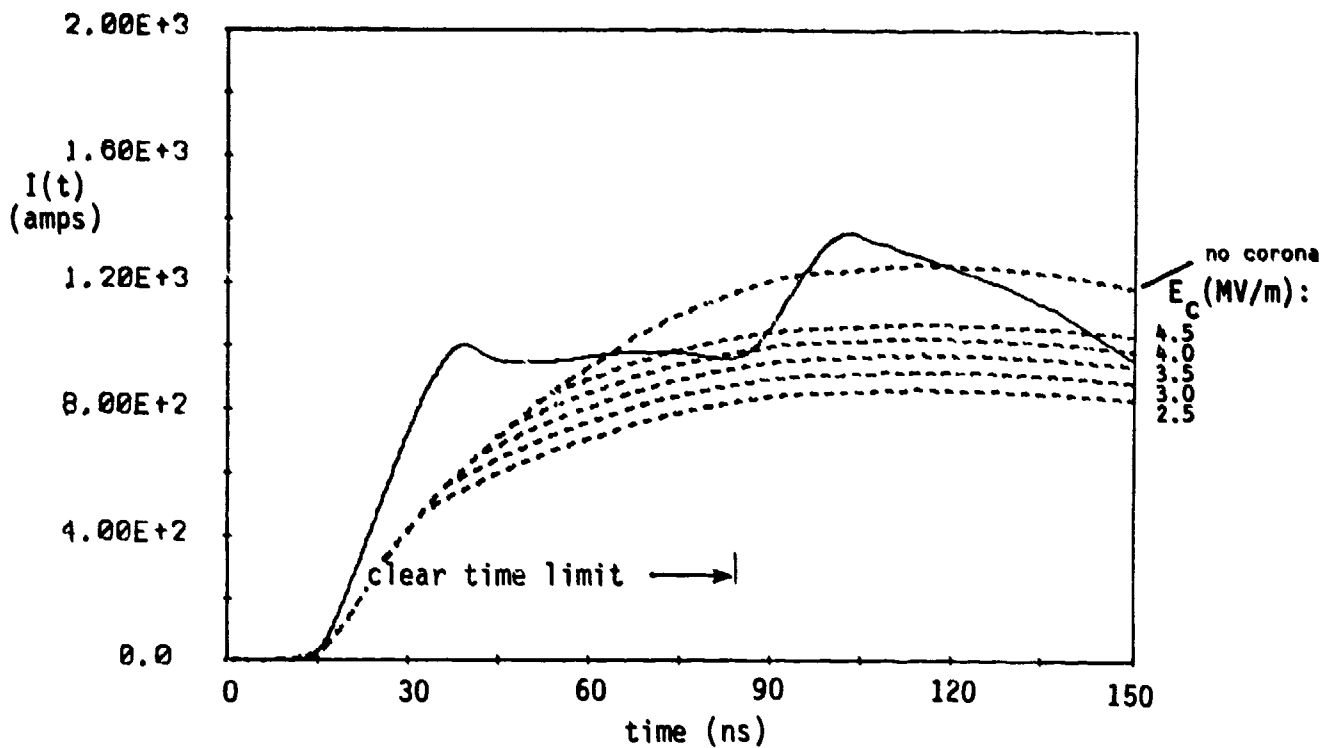
Figure 19.   Comparison of Measured (——) and Baum Corona
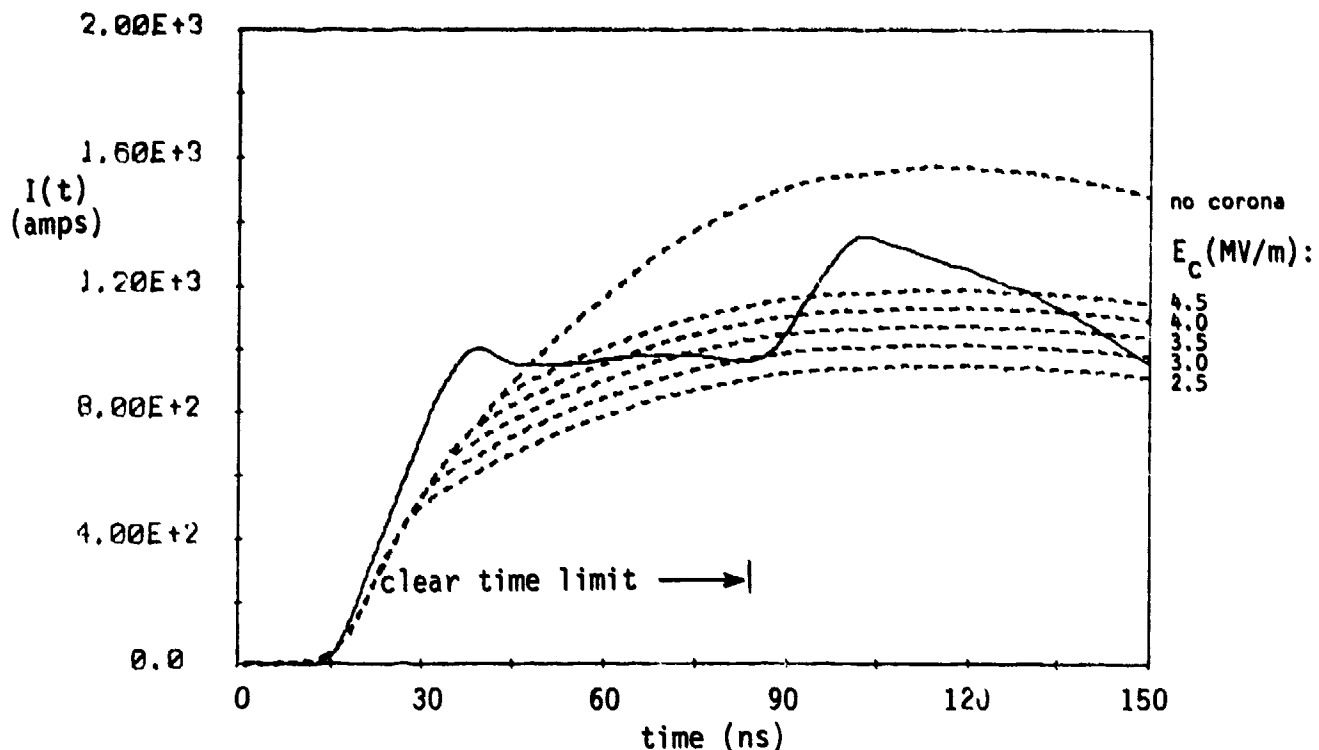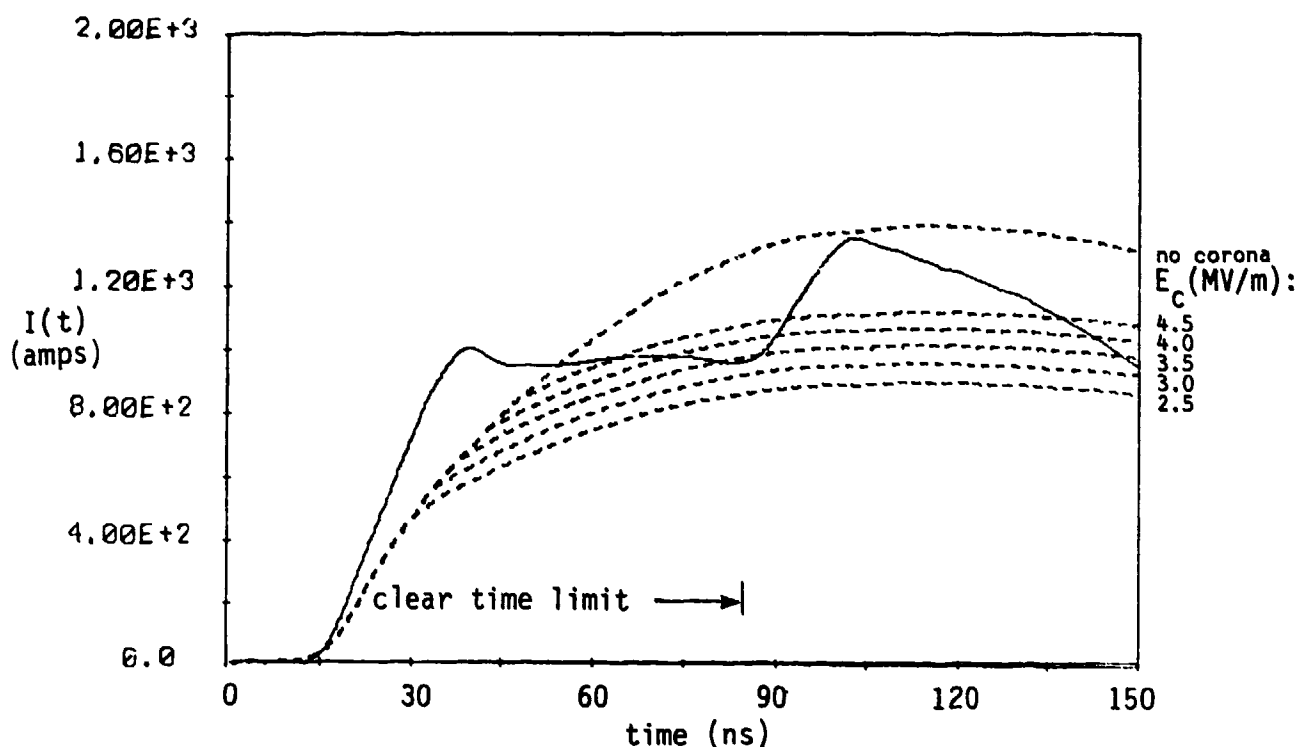Model (---) Results;

f_{g0} = 2.0; E_c Variations as Indicated
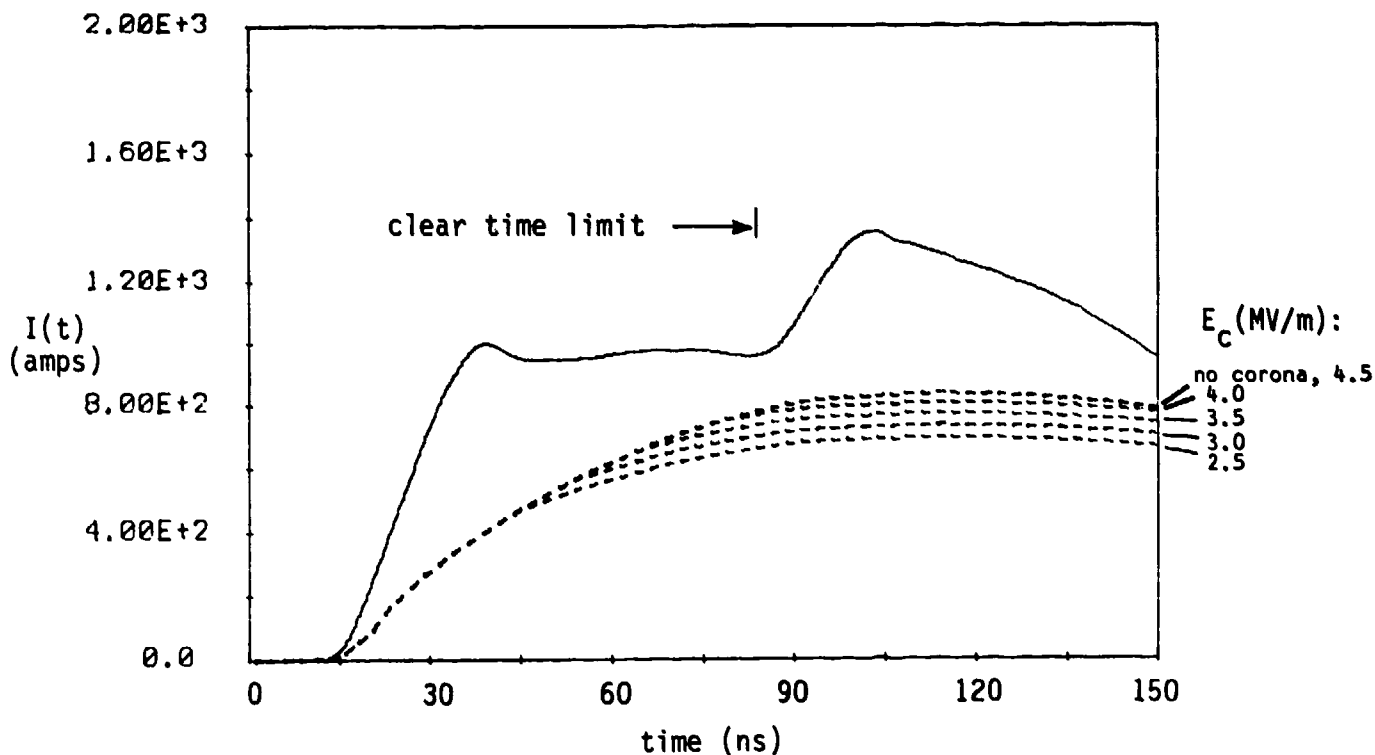
Figure 20.   Comparison of Measured (——) and Baum Corona
Model (---) Results:

f_{g0} = 3.0; E_c Variations as Indicated

2. Discussion of Results

In this model there are several parameters which are not well known from the geometry of the test configuration, and hence, may be varied in order to obtain a reasonable fit of the computed data to the measured results. These variables and the computed results are discussed in more detail below.

This subsection is comprised of the following elements: a list of the model variables with a brief description of each variable; known limitations on the range of each variable; a list of the specific values of each variable tested; and a results summary in which the results are described in terms of how changes in each variable affect the fit of the model to the data and how well, in general, the model could predict the results acquired experimentally.

Variables:

E_c E-field value at which breakdown occurs

f_{go} dimensionless factor to convert line geometry to equivalent coaxial transmission line or line above conducting plane

<u>Limitations:</u>

Peek's law constrains 2.5×10^6 V/m $< E_c < 4.5 \times 10^6$ V/m.

As indicated earlier, for a line in free space above a conducting ground plane, $f_{go} = 1/2\pi * \ln(2h/a_w)$. For a coaxial transmission line, $f_{go} = 1/2\pi * \ln(r_{outer}/r_{inner})$. In the experiment, the test wire ran diagonally from approximately 30 meters above ground to about 1 meter above the ground plane. This geometry does not readily translate into a constant value for f_{go}, although for this range of wire height, the range of f_{go} is fairly small: 1.14 to 1.68. In general, realistic values of f_{go} lie in the range $0.1 < f_{go} < 5.0$.

<u>Variations tested:</u>

E_c: 2.5×10^6, 3.0×10^6, 3.5×10^6, 4.0×10^6, 4.5×10^6 (all in V/m)

f_{go}: 0.5, 0.75, 1.0, 1.2, 1.4, 1.6, 1.8, 2.0, 3.0

Results:

Figures 7-11 show the effect of changing f_{go} while holding E_c constant. Essentially, higher values for f_{go} reduce the initial slope of the curve (i.e. the "no corona" section) and reduce the magnitude of the corona suppressed current. In all 5 figures, the curve for $f_{go} = 1.2$ appears to be the best fit. This corresponds to an equivalent geometry in which the test line would be approximately 10 meters above the ground plane. Alternatively, this corresponds to a equivalent coaxial cable with a ratio of r_{outer} to r_{inner} of about 1880 , or a coaxial cable with the test line used as the center conductor $(r = 1.07 \text{ cm})$ surrounded by an outer conductor of radius 20 meters.

Figures 12-20 indicate the effect of changing E_c while holding f_{g0} constant. Note that increasing values for E_c demonstrate delayed corona onset times, as expected. Figure 15 (showing variations in E_c for a constant $f_{go} = 1.2$ indicates $E_c = 5.25 \times 10^6$ V/m is approximately the value at which this model's prediction of corona onset matches the experimental data. It is possible that this value may be artificially high, since corona onset is not instantaneous, as this model assumes. In fact, corona is a complex function of air chemistry. It may be initiated earlier in time at a lower

E_c , but its full impact on the suppression of the line current may not be seen until the corona is fully developed (i.e., until a sufficient amount of the air surrounding the test line is ionized, essentially forming a capacitance between the line and the corona sheath).

In general, the model fit to the experimental data is fair. The model prediction of current suppression is less than actually noted. This may be due to several factors: (1) the model assumption of instantaneous corona formation neglects the current suppression effects during corona formation, (2) the capacitance assumed between the corona sheath and the test line may be too small, (3) the model assumes a perfectly conducting test line. A revision of the model to include inherent line losses might bring the predictions more in line with those seen experimentally.

C. The Engheta-Lee Corona Models

As previously mentioned, reference [7] takes a slightly different approach for the modeling of a line with corona. Starting from Maxwell's equations and the boundary conditions on the wire, the following expressions for current and charge on the surface of the conductor are derived:

$$\frac{1}{\epsilon_o}\frac{\partial Q'}{\partial z} + \mu_o \frac{\partial I}{\partial t} = 2\pi a_w \frac{\partial E_t}{\partial \rho}$$ (10a)

and

$$\frac{\partial I}{\partial z} + \frac{\partial}{\partial t}(Q') = -2\pi a_w J_\rho \quad .$$ (10b)

These equations are identical to those developed in [15].

With the definition that $v(z,t) \equiv Q'(z,t)/\epsilon_o$, this equation can be put into the standard form given in equation (9) as:

$$\frac{\partial v}{\partial z} + \mu_o \frac{\partial I}{\partial t} = 2\pi a_w \frac{\partial E_t}{\partial \rho}$$ (11a)

and

$$\frac{\partial I}{\partial z} + \frac{\partial}{\partial t}(\epsilon_o v) = - 2\pi a_w J_\rho \quad . \tag{11b}$$

Note that in this formulation there is no ground plane introduced. In comparing equations (11) with the previous equations (9) it is seen that the per-unit-length inductance and capacitance of the line have been replaced by the permeability and permittivity of free space, and that there is a source term in equation (11b). This source is proportional to J_ρ and in the Engheta-Lee paper, two models are discussed in which J_ρ takes one of two possible forms: one arising from considering the corona as a lossy conductor (conductivity model), and the other from considerations of Townsend's theory of corona (Townsend model) [8]. Both of these source terms will be discussed in more detail in this sub-section.

The other source term in equation (11a) is related to the radial derivative of the total electric field in the z direction. Unfortunately, the behavior of this component of the field is unknown, and not easily related to the incident electric field. In fact, this difficulty was discussed in [15] and resulted in a modified approach for the solution of the line response in that reference.

In the development in [7], this troublesome term is determined by examining the behavior of a single conductor in

free space without corona. For this case, reference [22] develops a set of equations similar to those of (11), and it is noted that the current source term, J_ρ, is zero and the source term for the first equation is related to the tangential component of the incident electric field. In the Engheta-Lee corona models, it is assumed that the excitation term in equation (11a) can be replaced with that arising from the incident field, and that the two telegrapher's equations for the line response then take the following form:

$$\frac{\partial v}{\partial z} + \mu_o \frac{\partial I}{\partial t} = \frac{4\pi}{\Omega(t)} E_z^{inc}(t) \tag{12a}$$

and

$$\frac{\partial I}{\partial z} + \frac{\partial}{\partial t}(\epsilon_o v) = -2\pi a_w J_\rho , \tag{12b}$$

where the factor Ω is a time-varying quantity given by

$$\Omega(t) = 2 \ln[2(ct - z\cos(\theta) + a_w\sin(\theta)) / (\Gamma a_w\sin(\theta))] \tag{13}$$

with Γ = exponential of Euler's constant $\cong$ 1.7810... and

θ = angle of E-field incidence with respect to the wire.

Notice that doing this assumes that the total field term, $\partial E_t / \partial \rho$, does not depend on and is not altered by the presence of the corona around the wire. The validity of this and other assumptions regarding the form of J_ρ will be ultimately validated in comparing the experimental response of the line with the data calculated as discussed below.

1. The Conductivity Model

a. Theory

In the conductivity model postulated by Engheta and Lee, it is assumed that when the line is driven into corona, the radial component of the corona current density J_ρ is proportional to the radial electric field E_ρ at the wire surface as

$$J_\rho = \sigma \ E_\rho \ U(|E_\rho| - E_c) \quad , \tag{14}$$

where E_c is the critical air breakdown electric field strength, σ is the effective conductivity of the corona and U( ) is the Heaviside unit step function. This step function assures that the conductivity effects of the corona are not seen in the model if the local field strength on the wire is below the critical air breakdown field strength.

This last expression involving the electric field may be related to the local charge density on the wire and can be rewritten as

$$J_\rho = \sigma \frac{Q'}{2\pi a_w \epsilon_o} U \left[\frac{Q'}{2\pi a_w \epsilon_o} - E_C \right] \quad . \tag{15}$$

In terms of the variable $v \equiv Q'/\epsilon_o$, this expression for the source term becomes

$$J_\rho = \sigma \frac{v}{2\pi a_w} U \left[\frac{v}{2\pi a_w} - E_C \right] \quad . \tag{16}$$

The conductivity model, therefore, requires a solution of equations (12a) and (12b) with J_ρ being determined by equation (16). It involves the specification of two independent parameters: the critical electric field strength E_C and the corona conductivity σ . The method of characteristics [21] was used in [7] to obtain a solution, however, in the present study, a direct time-marching solution of equations (12a) and (12b) was used. Comparisons between the responses using the two calculational methods yielded identical results.

For this model, a parametric study was performed using the baseline geometry, in order to ascertain the best choice for E_C and σ . Figures 21 through 35 present the results of these calculations.

Figure 21. Comparison of Measured (———) and Conductivity
Model (———) Results:

E_c = 1.0 MV/m; σ Variations as Indicated

Figure 22. Comparison of Measured (———) and Conductivity
Model (———) Results:

E_c = 1.5 MV/m; σ Variations as Indicated
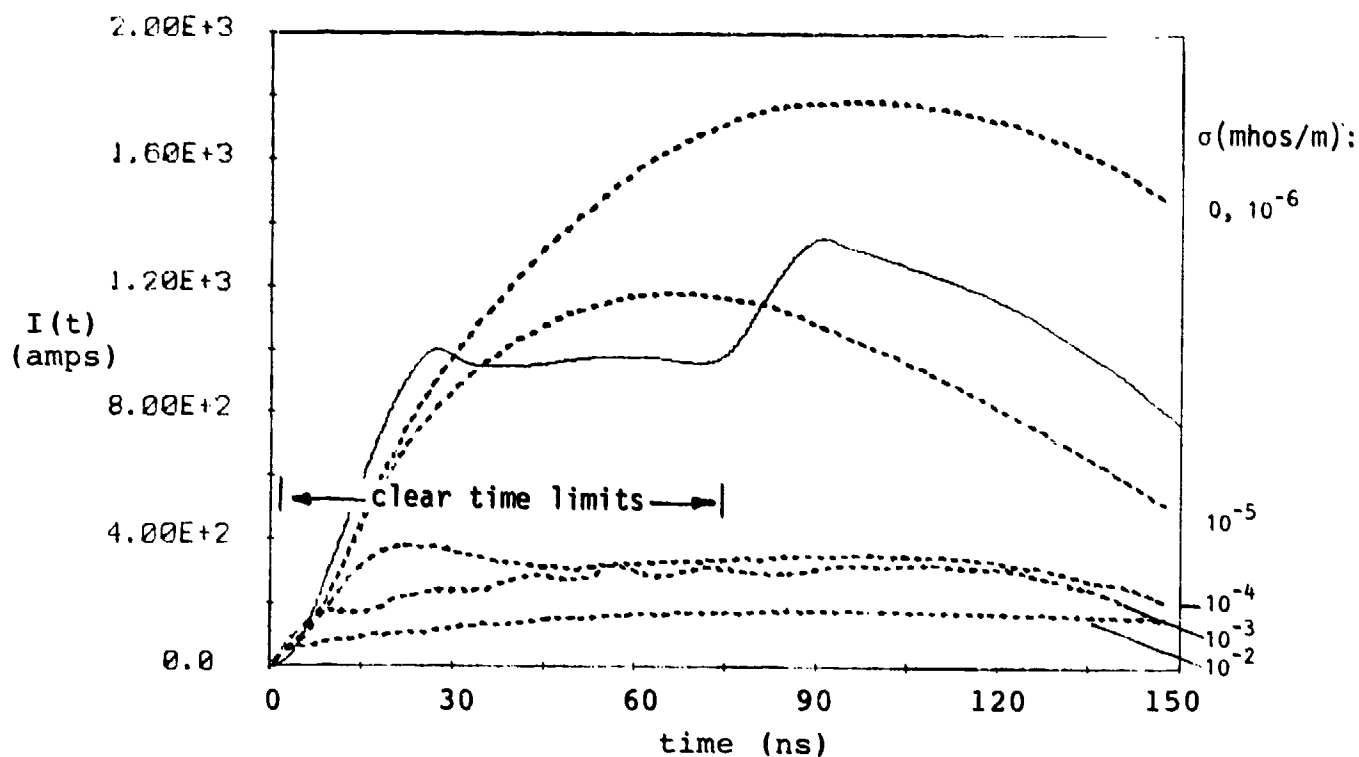
53

Figure 23. Comparison of Measured (——) and Conductivity
Model (---) Results:

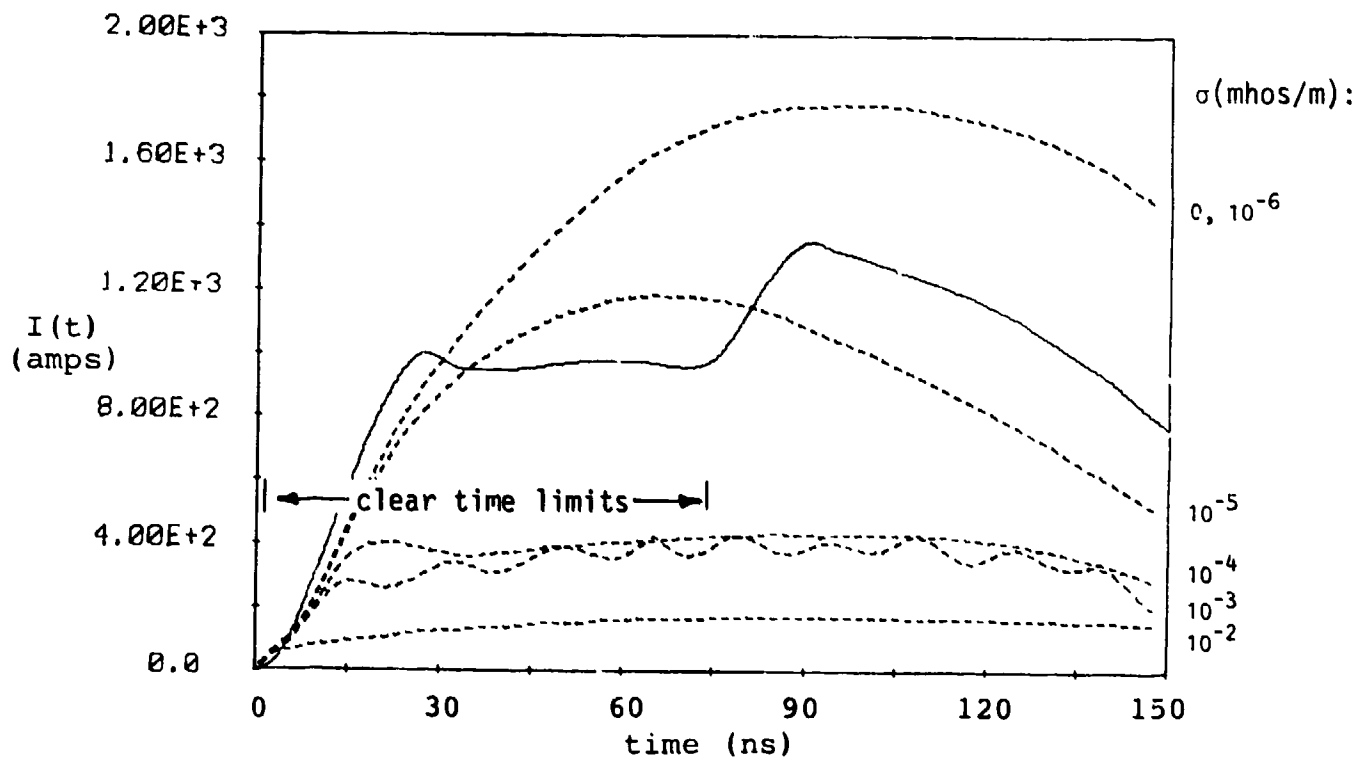E_c = 2.0 MV/m; σ Variations as Indicated

Figure 24. Comparison of Measured (——) and Conductivity
Model (---) Results:

E_c = 2.5 MV/m; σ Variations as Indicated

Figure 25. Comparison of Measured (——) and Conductivity Model (---) Results:

E_c = 3.0 MV/m; σ Variations as Indicated

Figure 26. Comparison of Measured (——) and Conductivity Model (---) Results:
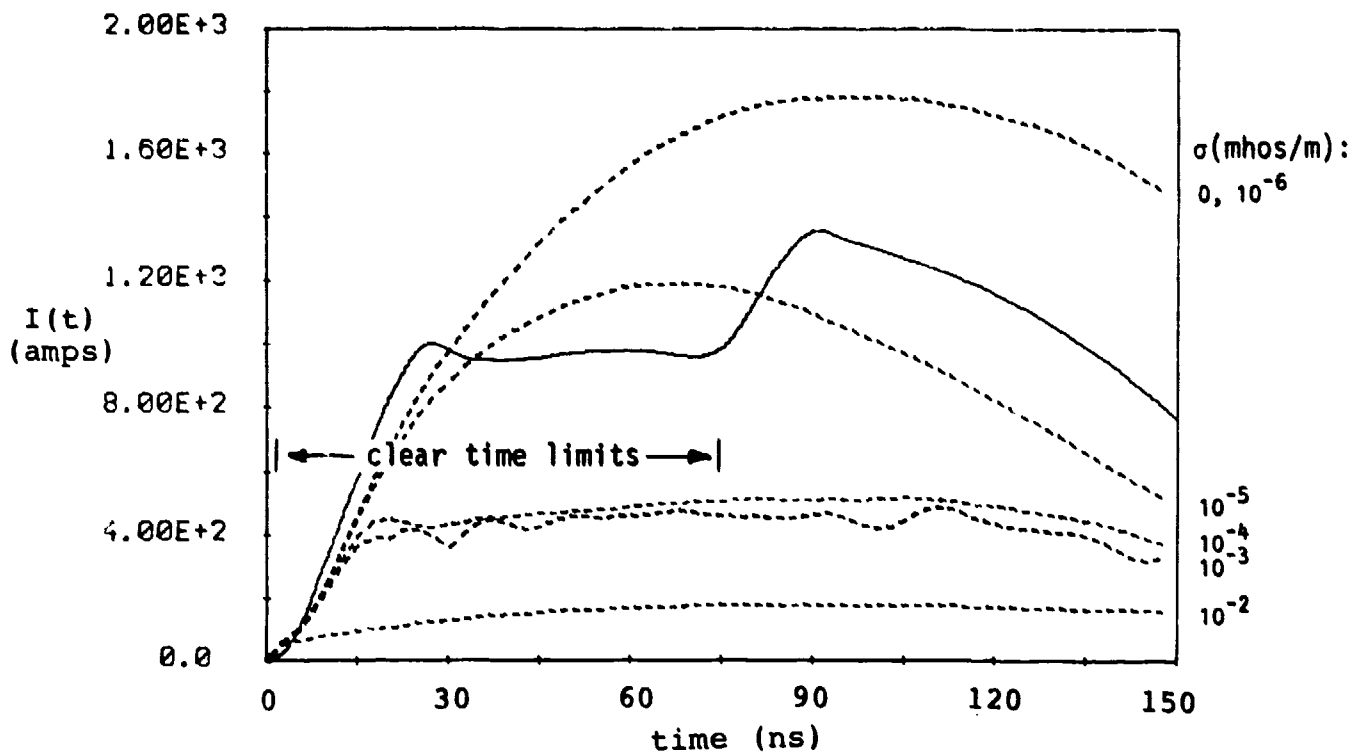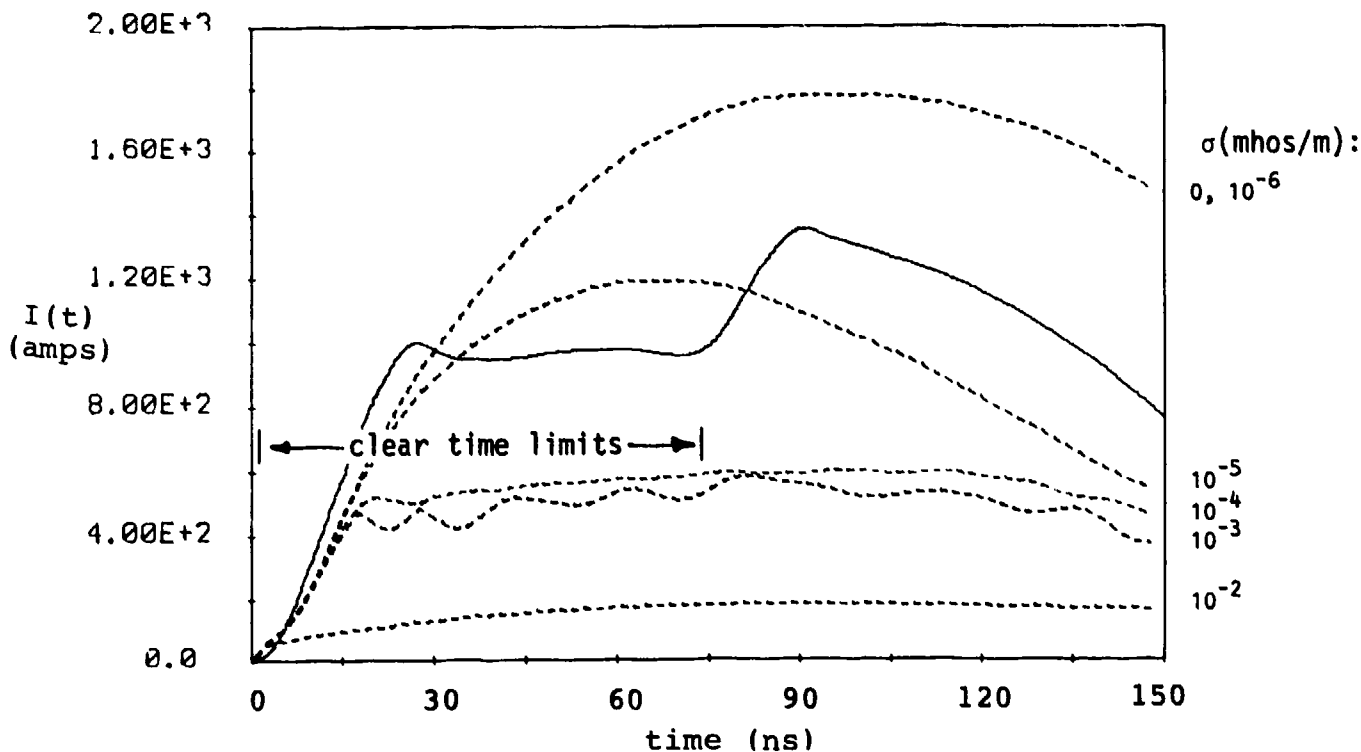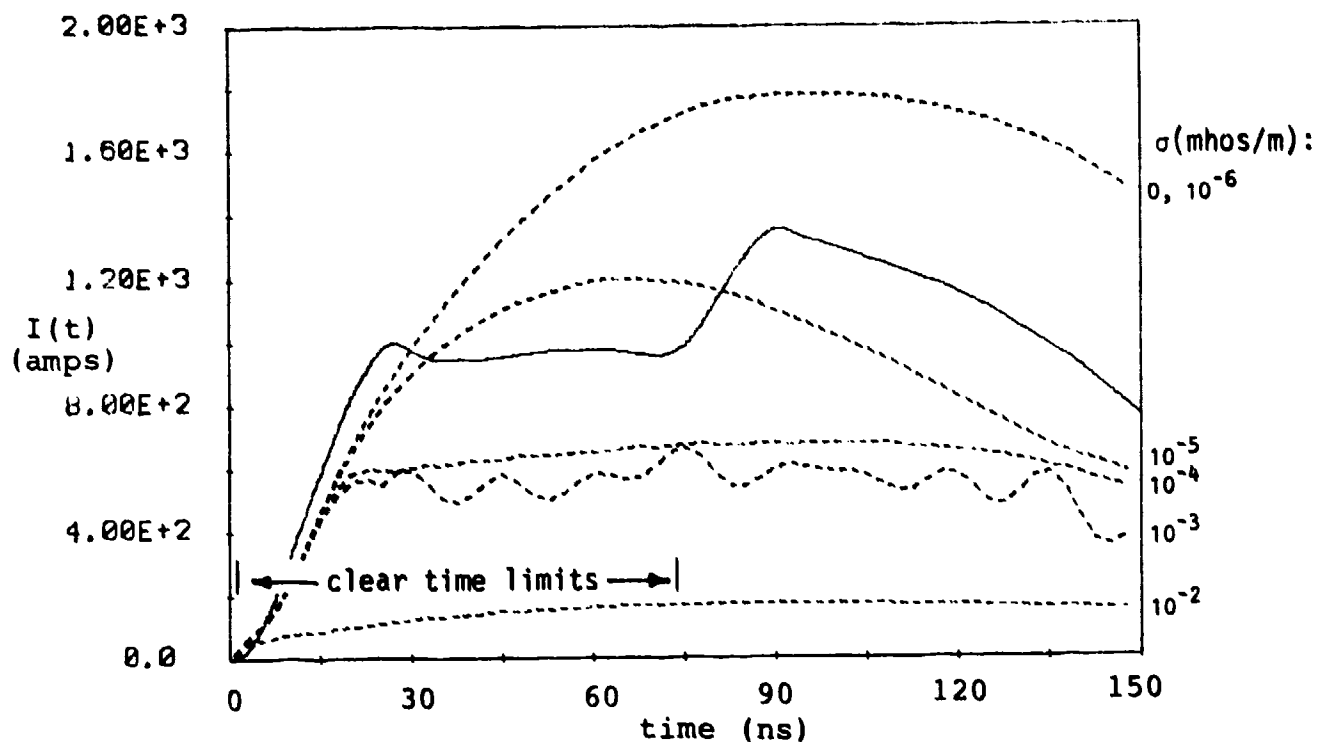
E_c = 3.5 MV/m; σ Variations as Indicated
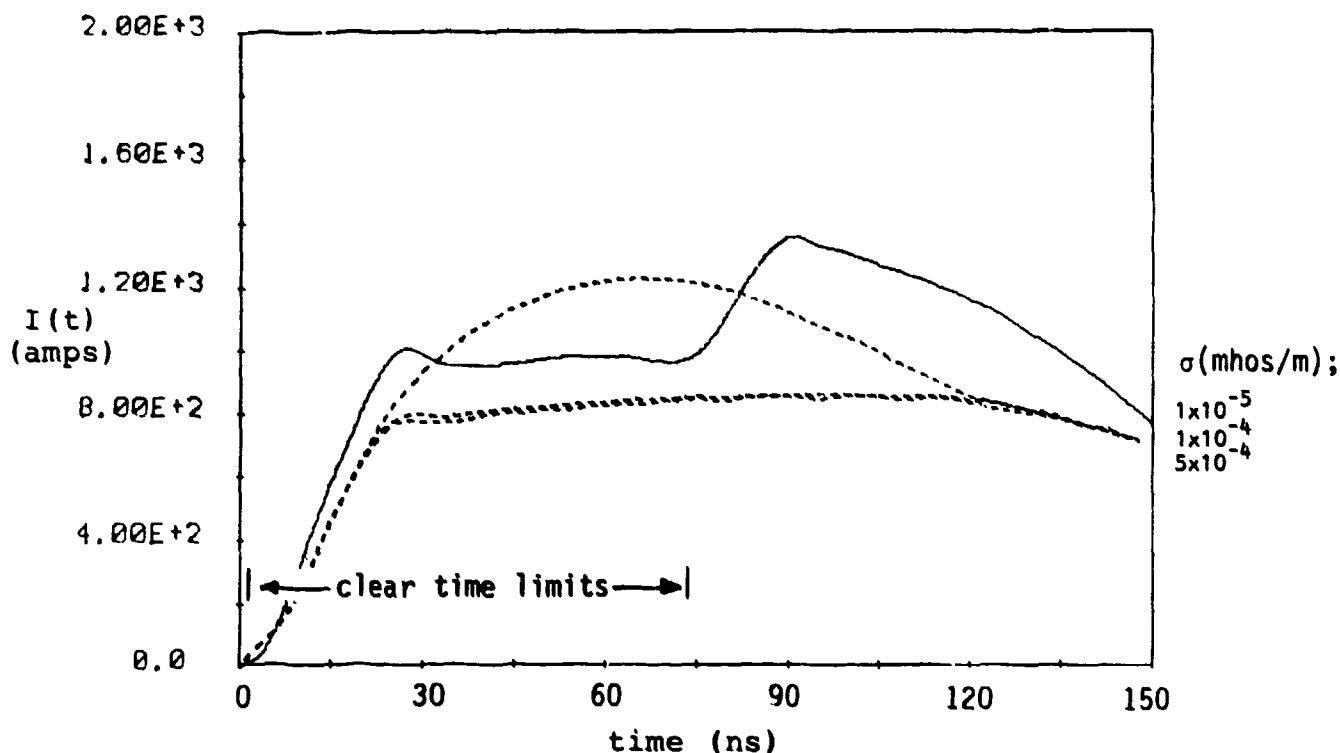
Figure 27. Comparison of Measured (——) and Conductivity
Model (- - -) Results:

E_c = 4.0 MV/m; σ Variations as Indicated
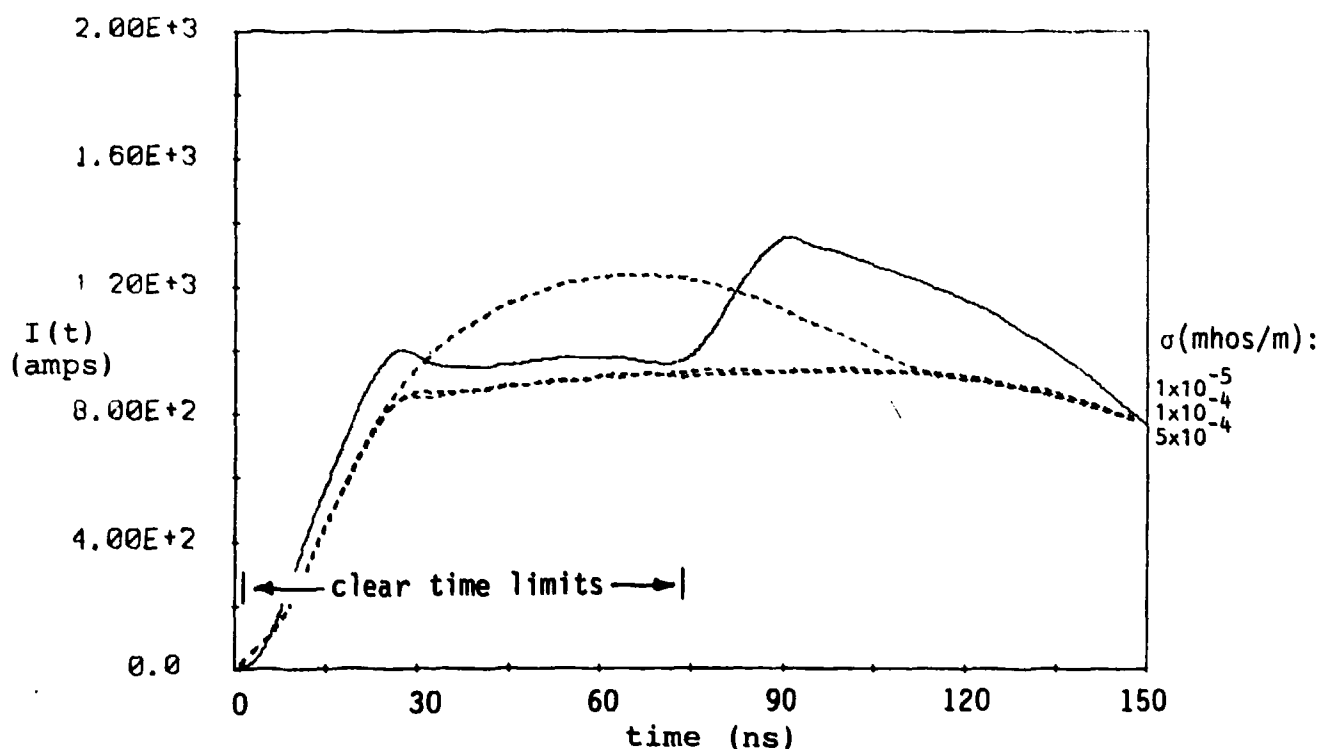
Figure 28. Comparison of Measured (——) and Conductivity
Model (- - -) Results:

$\dot{E}_c$ = 4.5 MV/m; σ Variations as Indicated

56
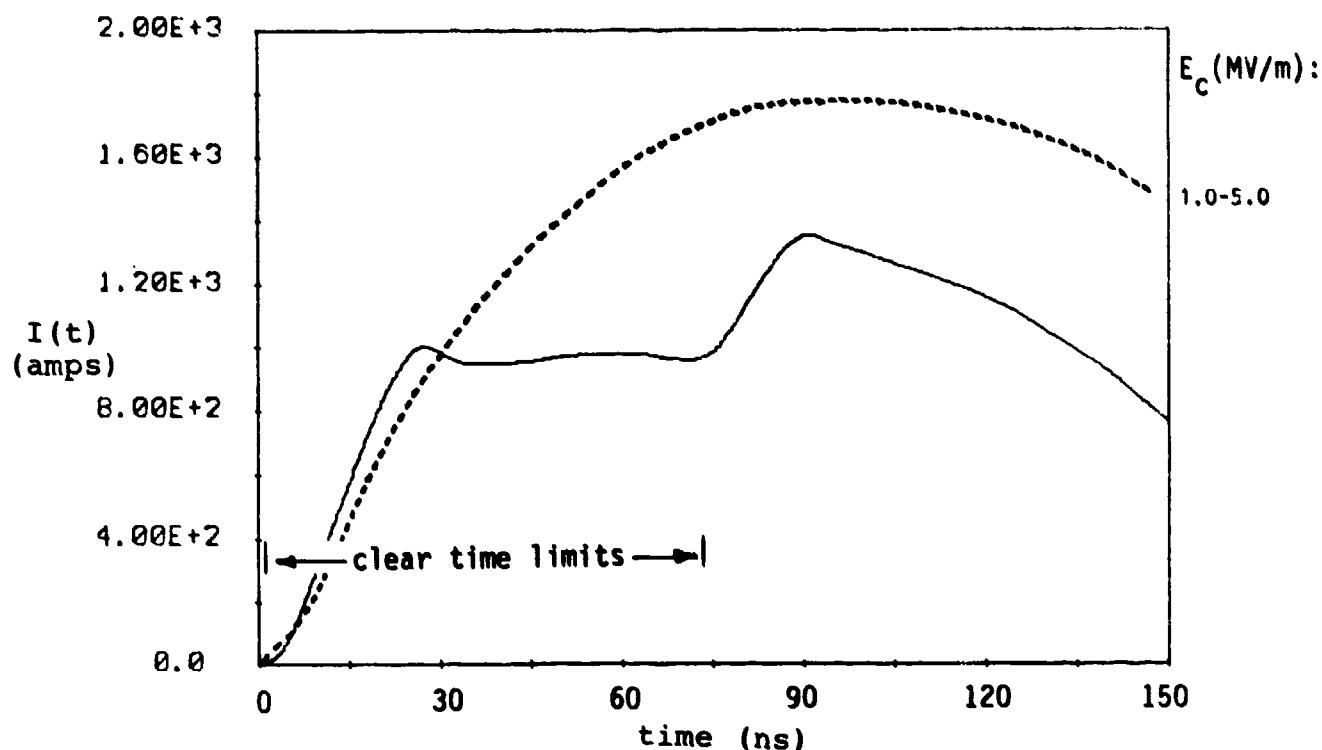
Figure 29.   Comparison of Measured (——) and Conductivity
             Model (- - -) Results:

$\sigma = 10^{-6}$ mhos/m; E_c Variations as Indicated
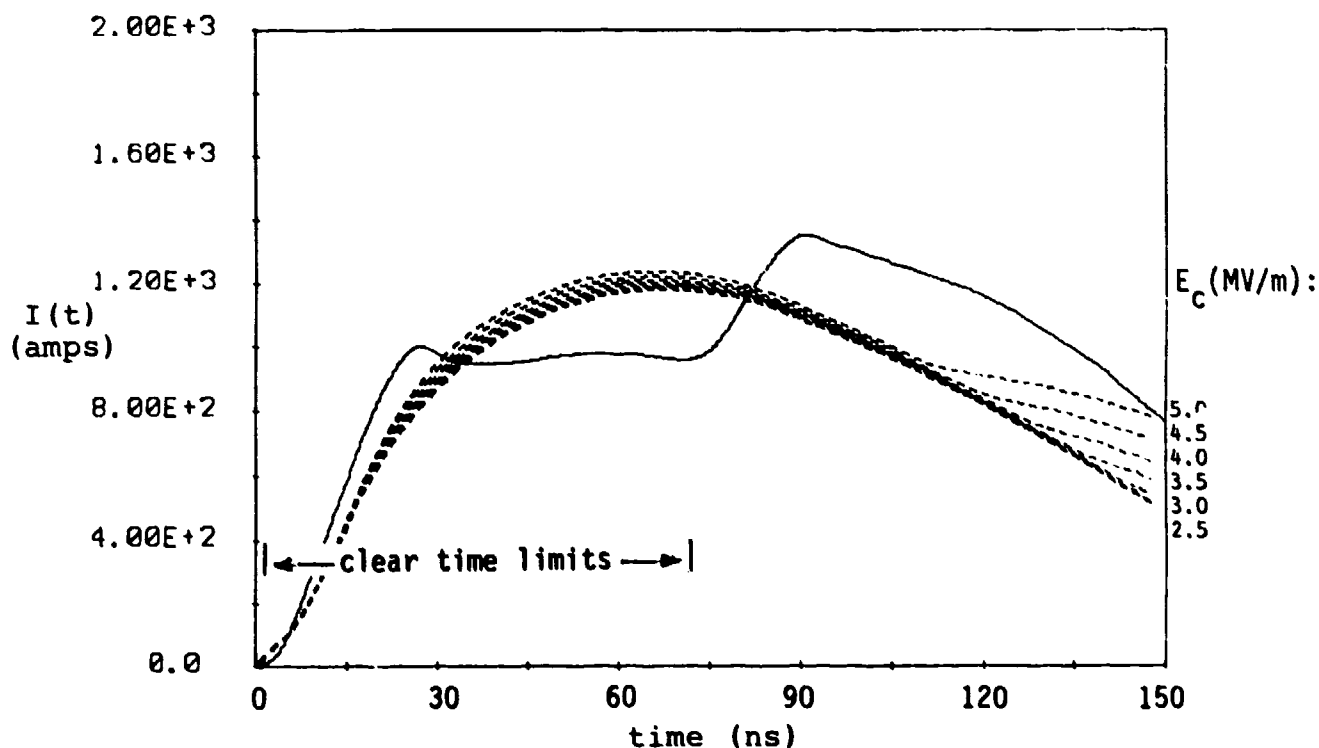
Figure 30.   Comparison of Measured (——) and Conductivity
             Model (- - -) Results:

$\sigma = 10^{-5}$ mhos/m; E_c Variations as Indicated

57
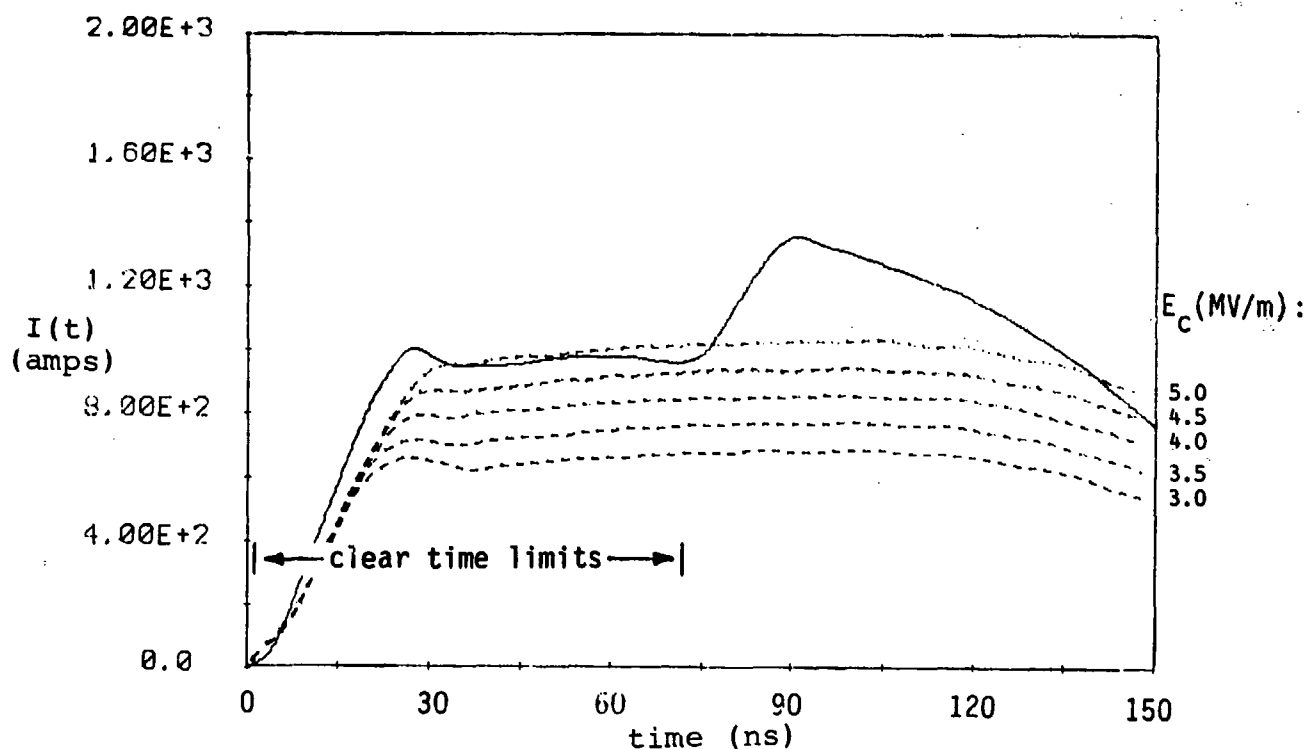
Figure 31. Comparison of Measured (——) and Conductivity Model (---) Results:

$\sigma = 5 \times 10^{-5}$ mhos/m; E_c Variations as Indicated

Figure 32. Comparison of Measured (——) and Conductivity Model (---) Results:

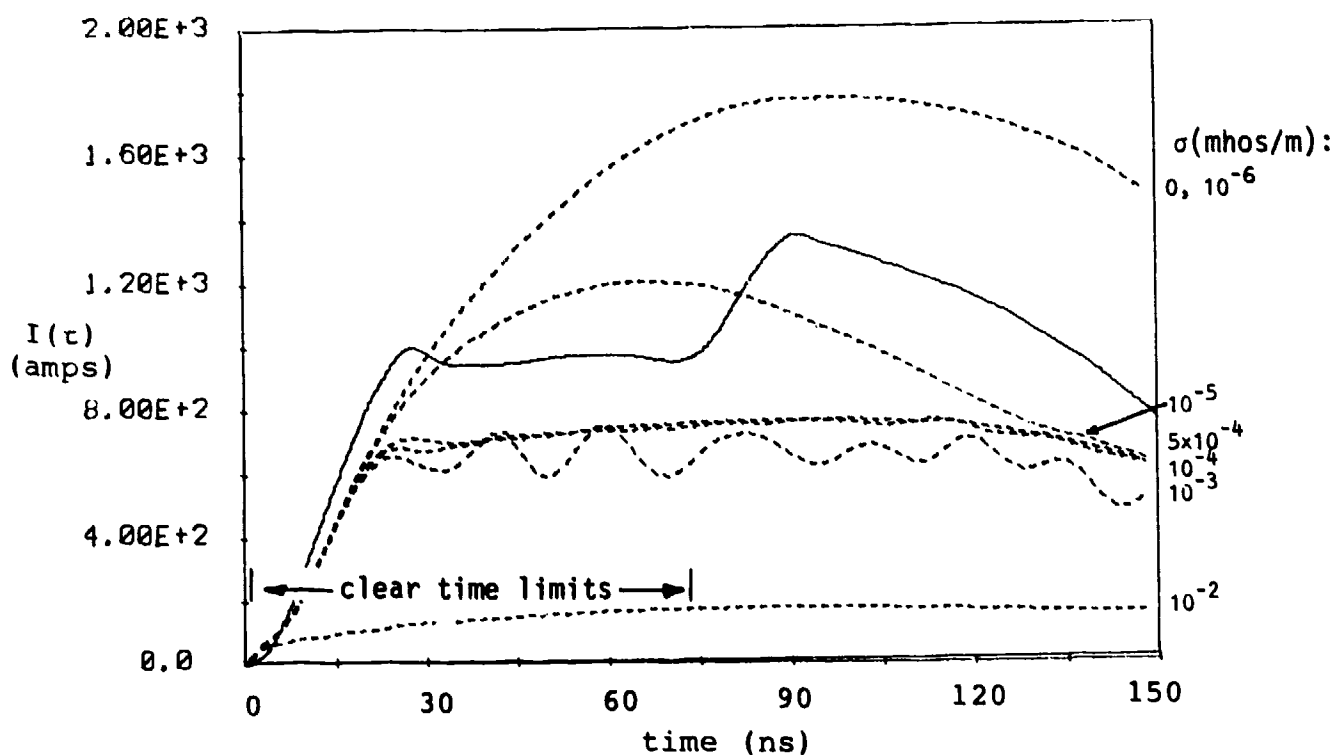$\sigma = 10^{-4}$ mhos/m; E_c Variations as Indicated

Figure 33. Comparison of Measured (——) and Conductivity Model (---) Results:

$\sigma = 5 \times 10^{-4}$ mhos/m; E_c Variations as Indicated
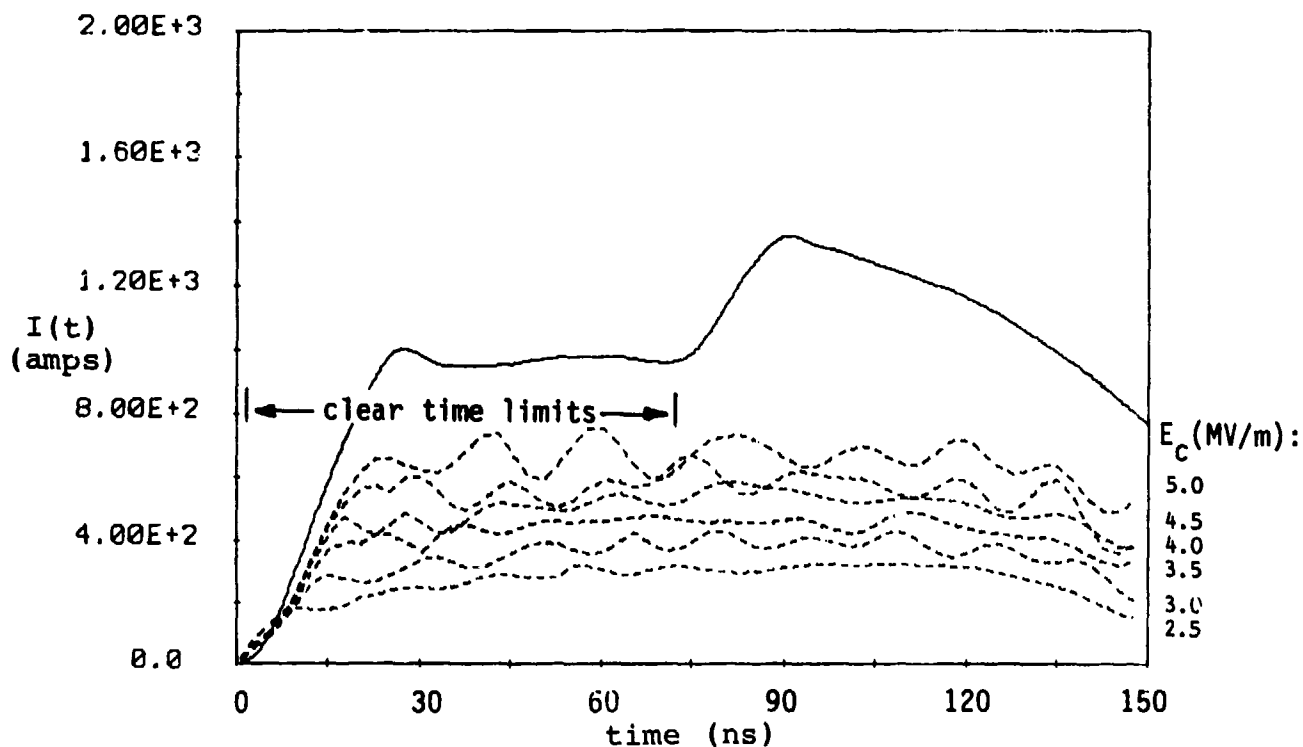
Figure 34. Comparison of Measured (——) and Conductivity Model (---) Results:

$\sigma = 10^{-3}$ mhos/m; E_c Variations as Indicated
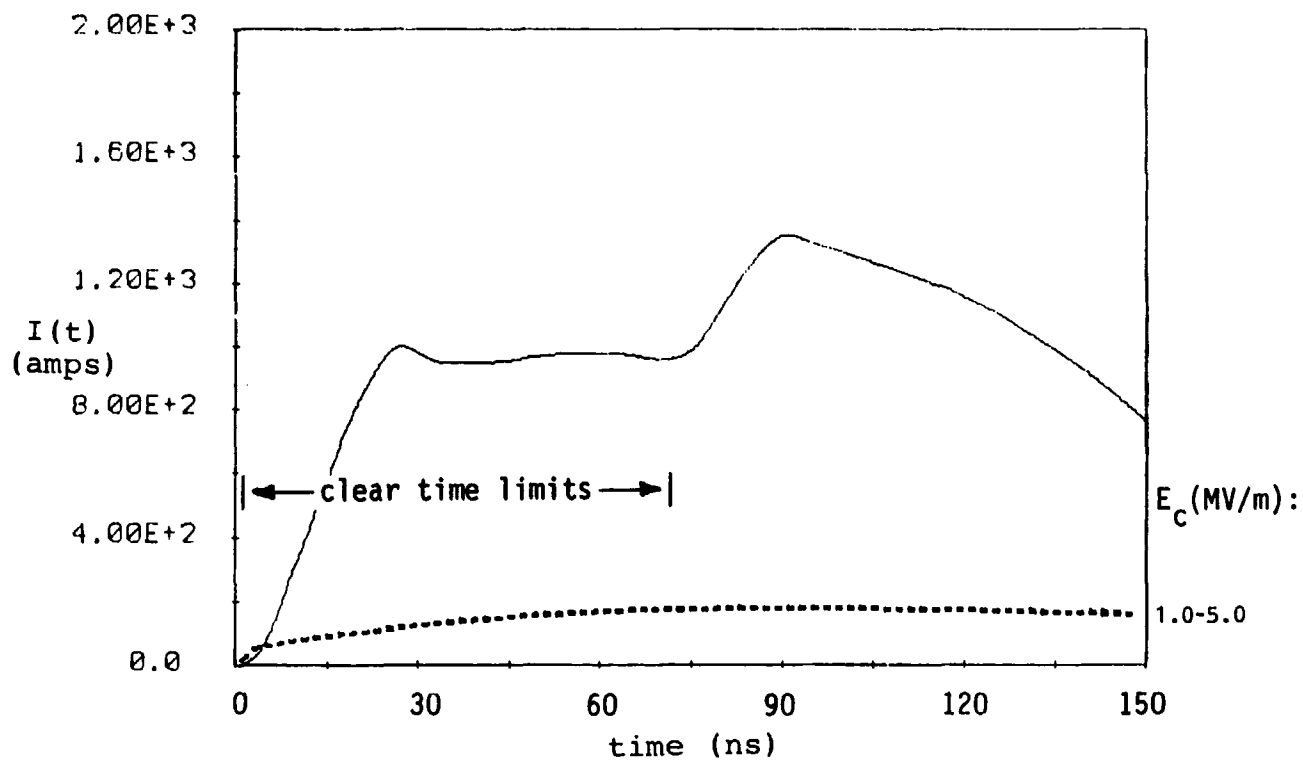
Figure 35. Comparison of Measured (——) and Conductivity Model (---) Results:
$\sigma = 10^{-2}$ mhos/m; E_c Variations as Indicated
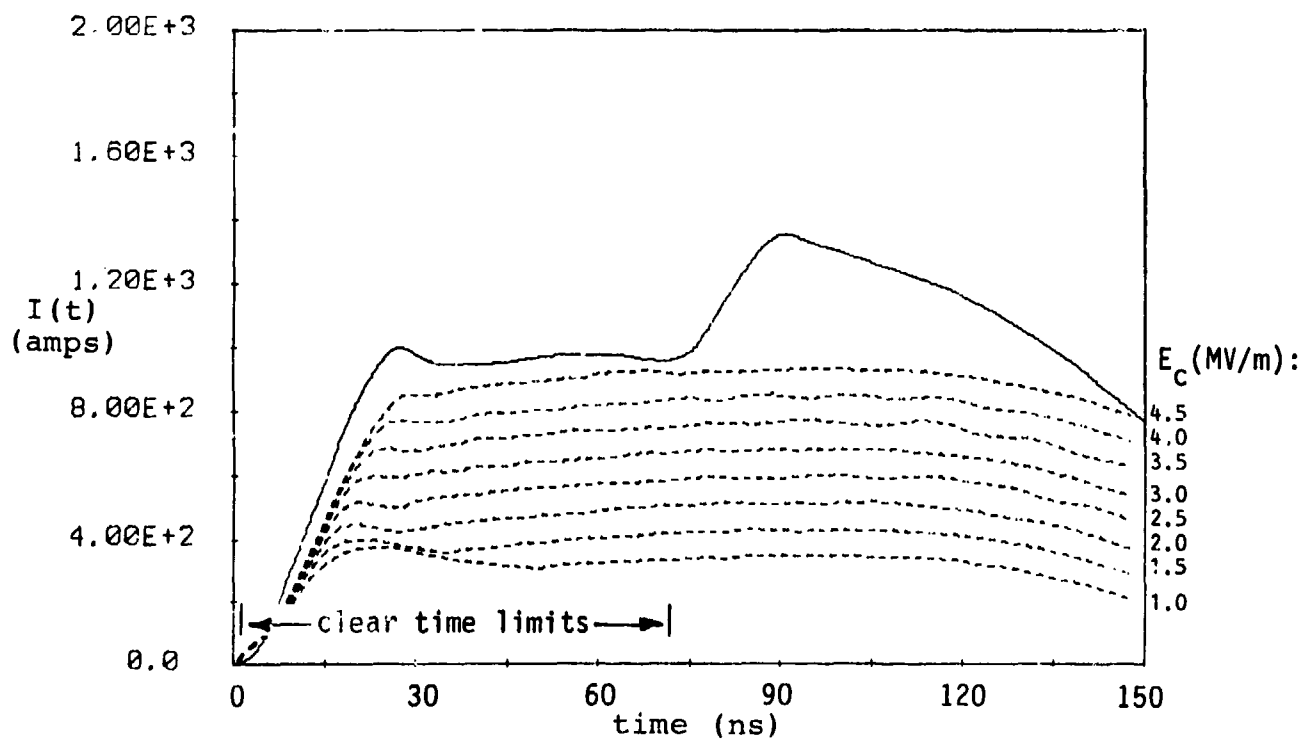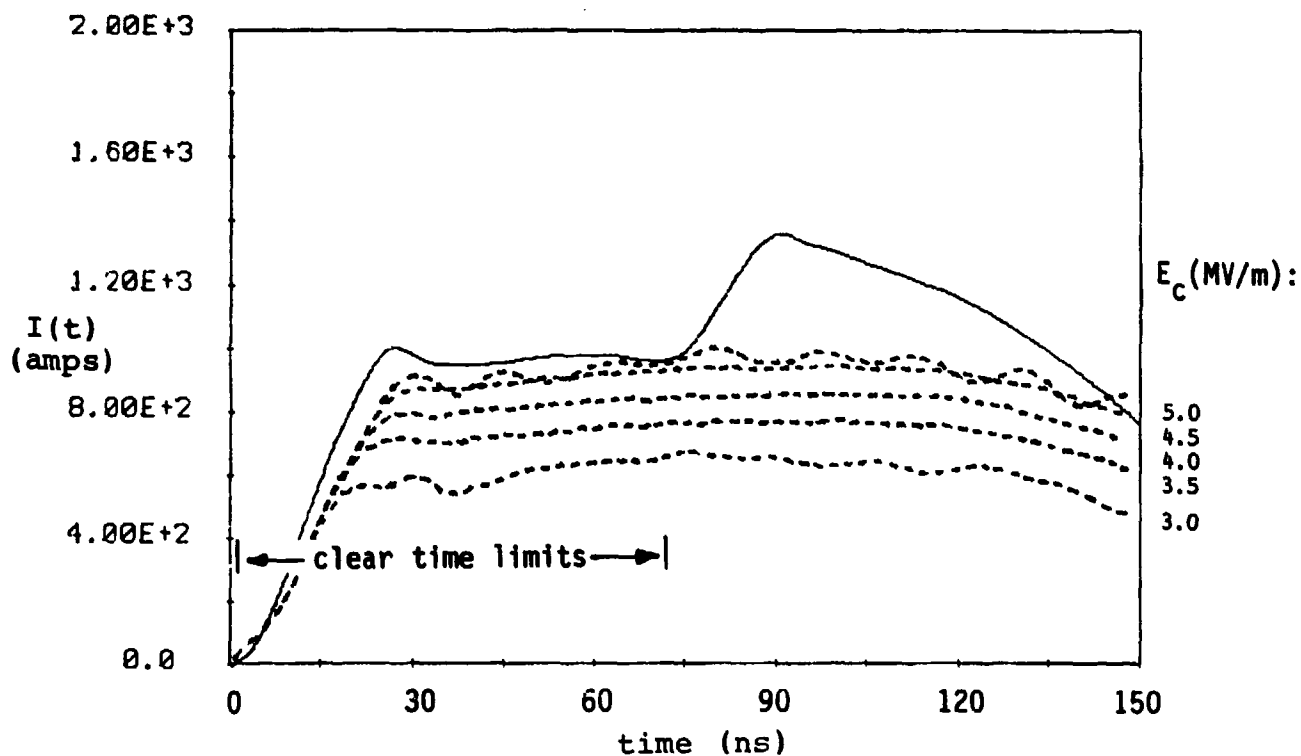
b. Discussion of Results

The following subsection discusses the limits of the parameters of this corona model and the resulting computed responses.

Variables:

E_c E-field value at which breakdown occurs

σ air conductivity

Limitations:

Peek's law constrains 2.5×10^6 V/m $< E_c < 4.5 \times 10^6$ V/m.

Air conductivity during corona is very difficult to measure since it is a function of the amount and polarity of ionization as well as of the local relative humidity and pressure (alternatively, it is a function of the mobility and number density of the charge carriers). Reference 6 suggests some possible values for use with this model. For comparison, some nominal conductivity values for well known materials are given in Table II below [taken from reference 22].

Material	Conductivity, σ(S/m)	Material	Conductivity, σ(S m)
Silver	6.17×10^7	Fresh water	10^{-3}
Copper	5.80×10^7	Distilled water	2×10^{-4}
Gold	4.10×10^7	Dry soil	10^{-5}
Aluminum	3.54×10^7	Transformer oil	10^{-11}
Brass	1.57×10^7	Glass	10^{-12}
Bronze	10^7	Porcelain	2×10^{-13}
Iron	10^7	Rubber	10^{-15}
Seawater	4	Fused quartz	10^{-17}

Table II.

Nominal Conductivity Values for Selected Materials

61

<u>Variations tested</u>:

E_c: 1.0 x 10^6, 1.5 x 10^6, 2.0 x 10^6, 2.5 x 10^6,

3.0 x 10^6, 3.5 x 10^6 (all in V/m)

σ: 10^{-6}, 10^{-5}, 10^{-4}, 10^{-3}, 10^{-2} (all in mhos/m)

<u>Results</u>:

Figures 21-28 show the predictions of this model for constant values of E_c . For larger values of E_c , the model predictions begin to approximate measured current values when $\sigma = 10^{-4}$ mhos/meter.

Holding σ constant while varying E_c is demonstrated in Figures 29-35. Extremely low values of σ ($\sigma < 10^{-6}\Omega^{-1}m^{-1}$) show no variation with E_c . This is to be expected, since for those values of σ , the air remains an insulator at even high field strengths. For $\sigma = 10^{-5}\Omega^{-1}m^{-1}$ some variation is seen with E_c , but the model fit to the experimental data is still not especially good. At $\sigma = 10^{-4}\Omega^{-1}m^{-1}$, the results predicted by the model are quite close to those seen experimentally, especially for higher values of E_c . At higher values of σ , the model predictions become irregular, possibly due to instabilities in the method

of solution used. These are especially noticeable at $\sigma = 10^{-3}\Omega^{-1}m^{-1}$. Values of σ above $10^{-3}\Omega^{-1}m^{-1}$ produce results well below the observed values.

2. The Townsend Model

a. Theory

The Townsend model as described in [7] assumes that the current term in equation (12b) has the form

$$J_\rho = \alpha_j \, Q' \left[\frac{|Q'|}{2\pi a_w \epsilon_o} - E_c \right] U \left[\frac{|Q'|}{2\pi a_w \epsilon_o} - E_c \right] \tag{17}$$

or, in terms of the variable v,

$$J_\rho = \alpha_j \epsilon_o v \left[\frac{v}{2\pi a_w} - E_c \right] U \left[\frac{v}{2\pi a_w} - E_c \right] . \tag{18}$$

The term α_j in the above equations is related to a Townsend ionization coefficient as discussed in [7], and in this model is a parameter to be varied to fit the experimental data. As in the previous case, a series of calculations for the baseline line geometry was made with α_j and E_c varying, and these results are presented in Figures 36 through 48.

63
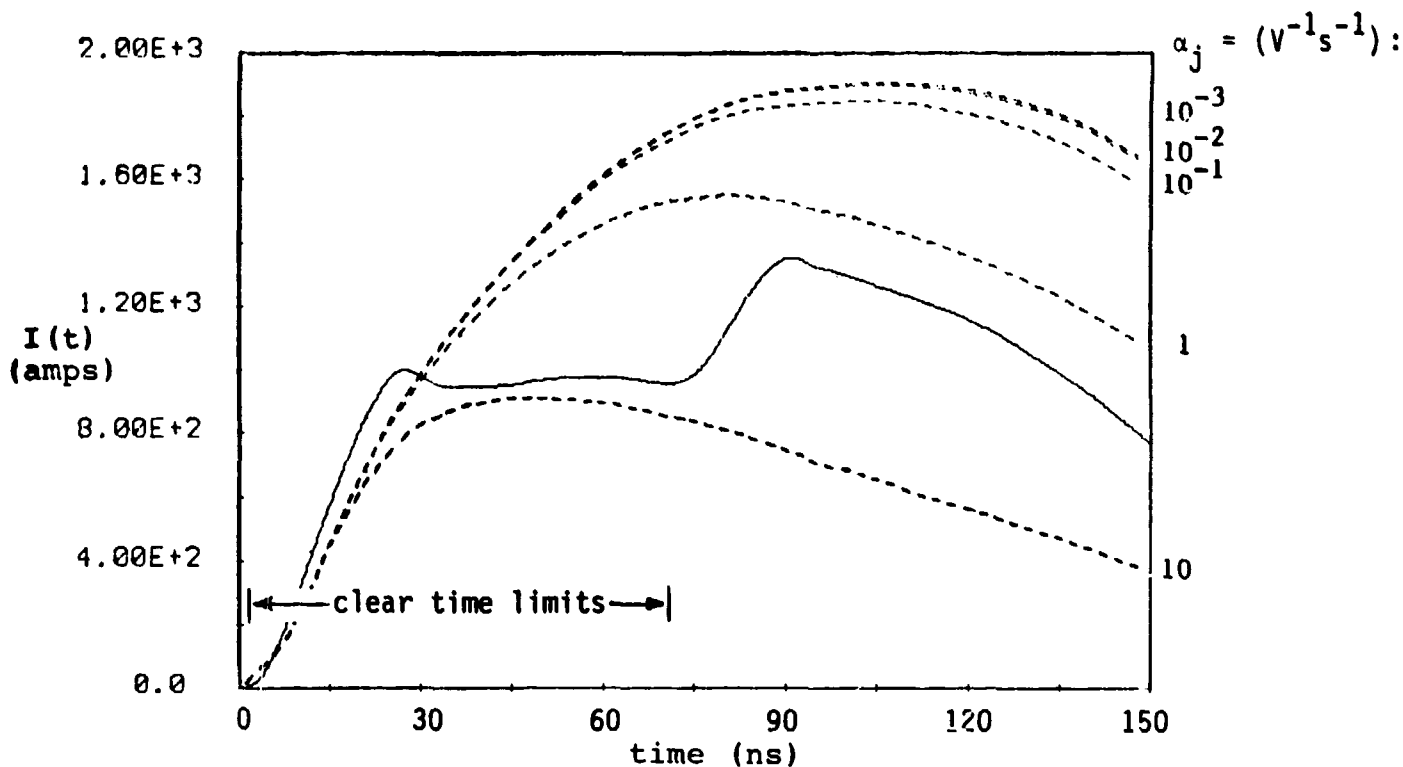
Figure 36.   Comparison of Measured (——) and Townsend
Model (- - -) Results:

E_c = 1.0 MV/m; α_j Variations as Indicated
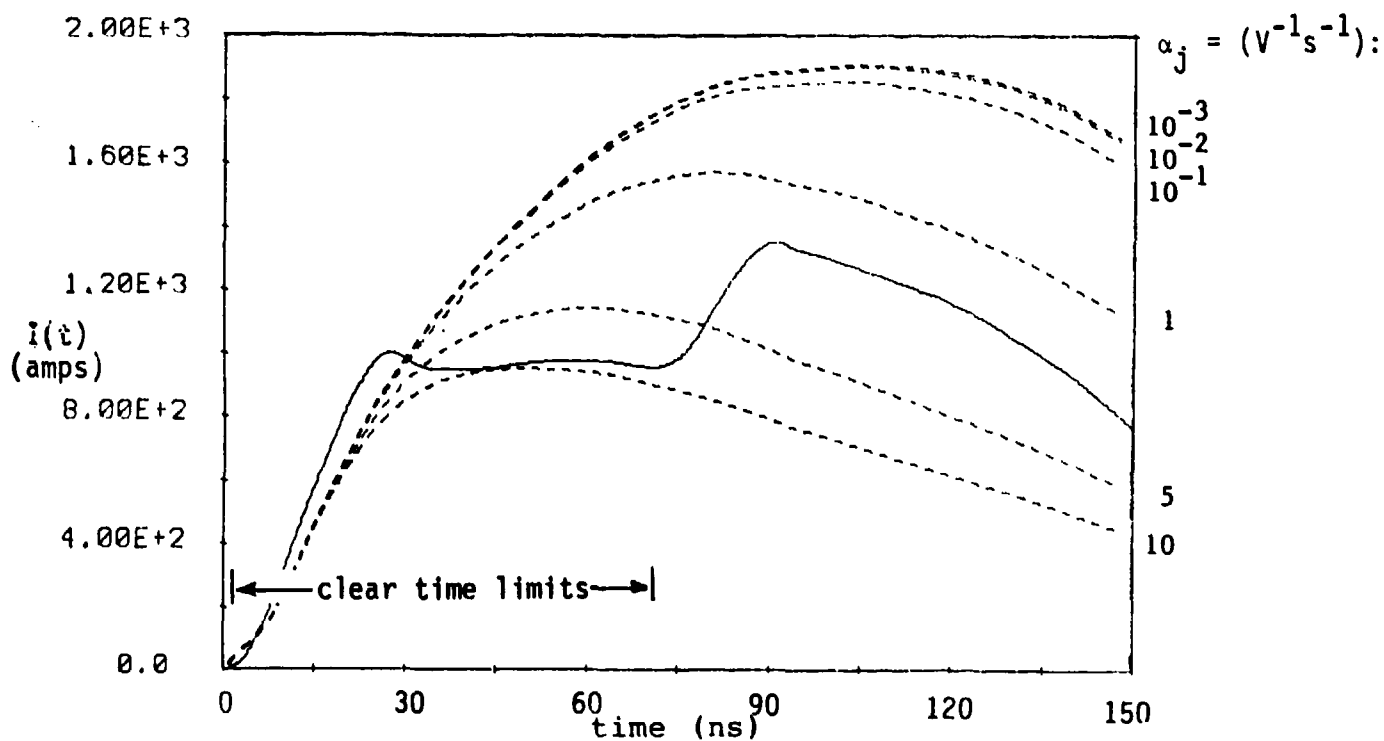
Figure 37.   Comparison of Measured (——) and Townsend
Model (- - -) Results:

E_c = 1.5 MV/m; α_j Variations as Indicated

64
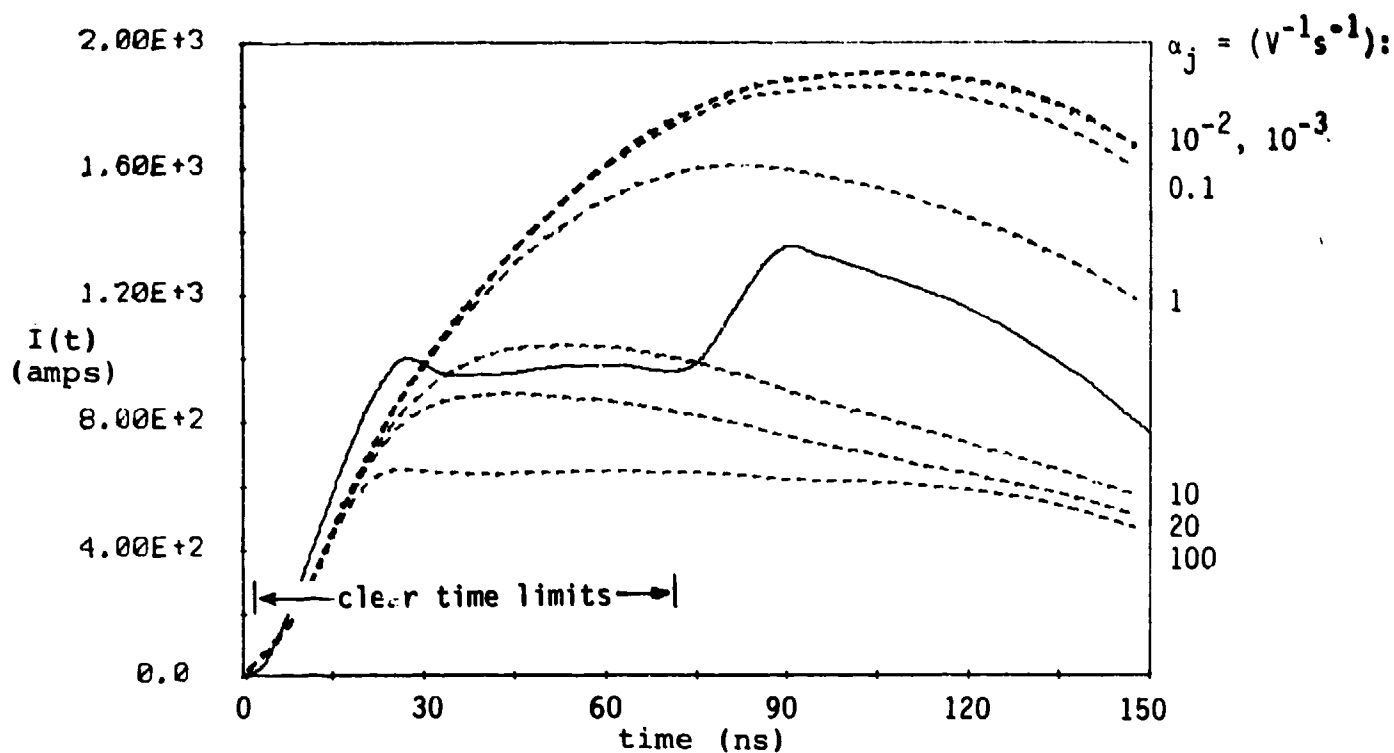
Figure 38. Comparison of Measured (——) and Townsend
Model (---) Results:

E_c = 2.5 MV/m; α_j Variations as Indicated
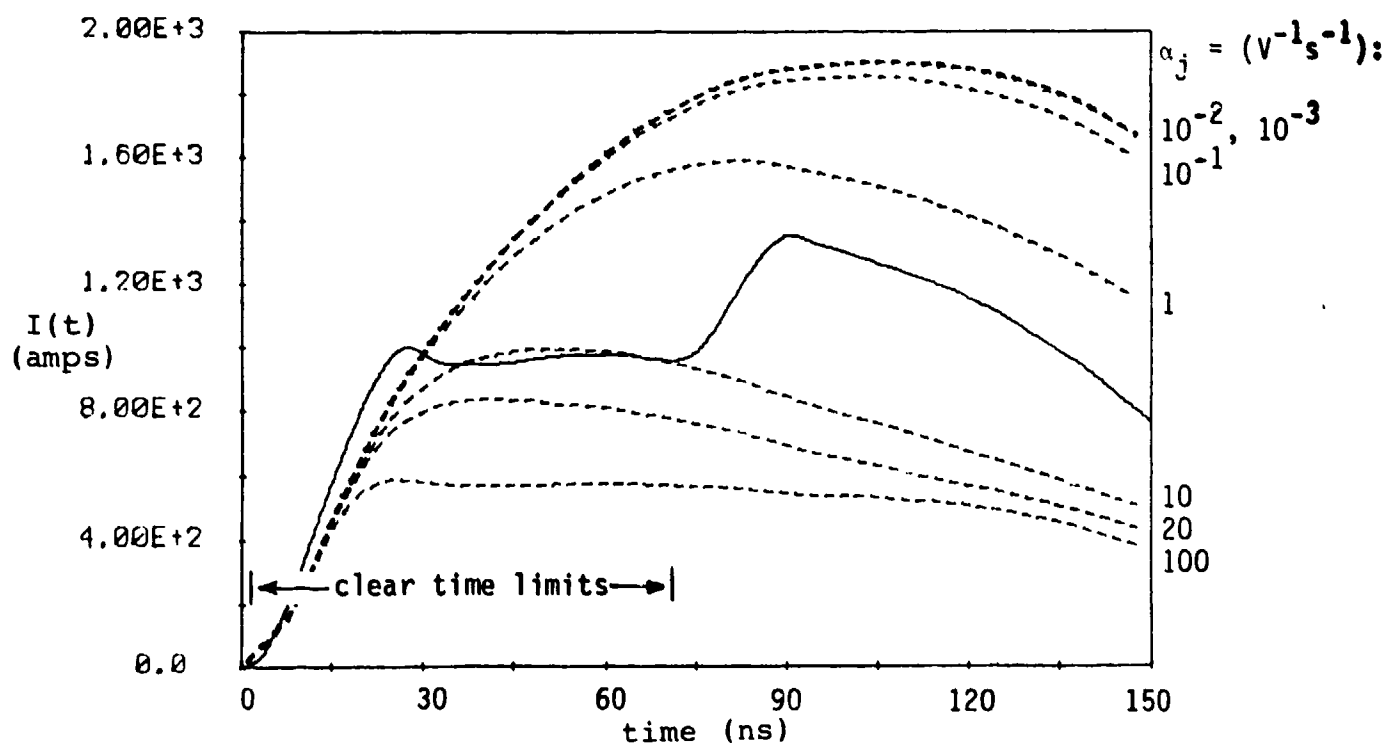
Figure 39. Comparison of Measured (——) and Townsend
Model (---) Results:

E_c = 2.0 MV/m; α_j Variations as Indicated
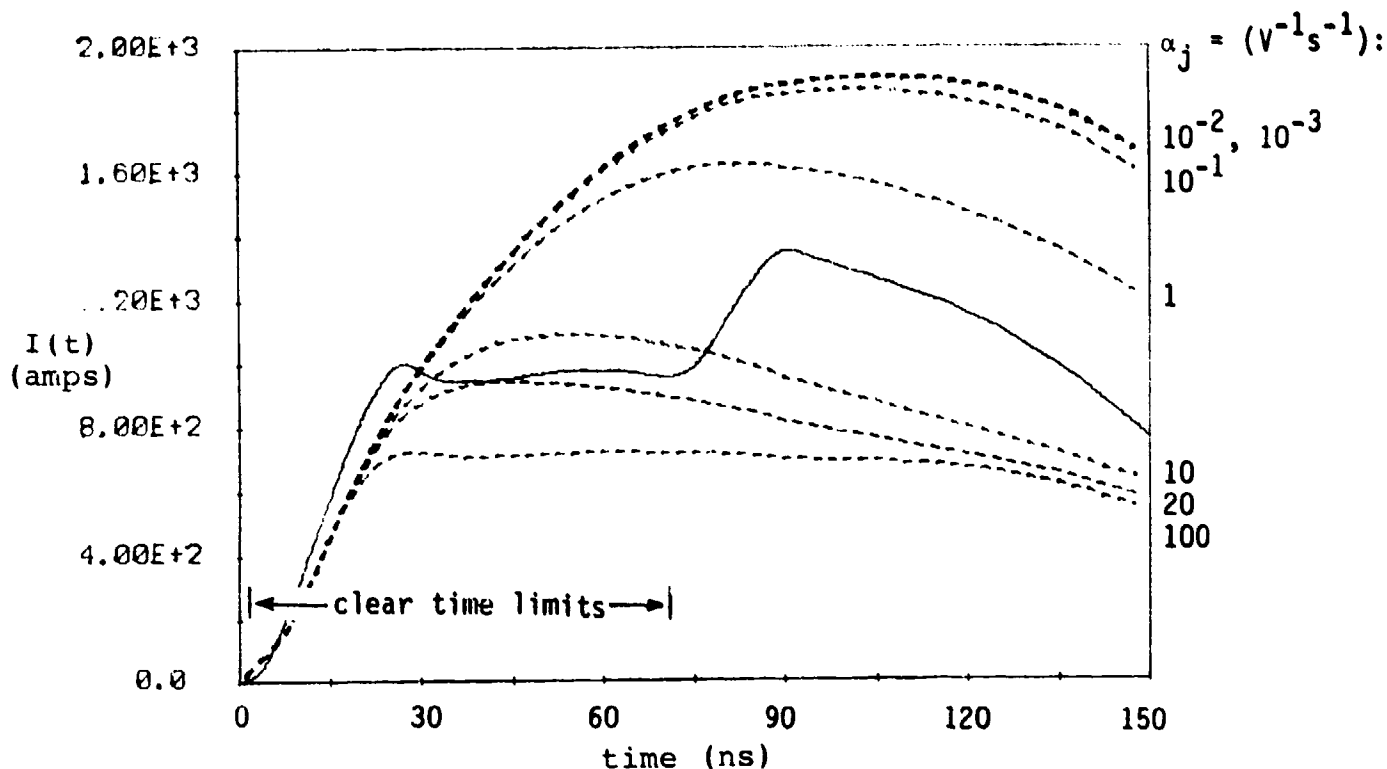
Figure 40. Comparison of Measured (——) and Townsend
Model (---) Results:

E_c = 3.0 MV/m; α_j Variations as Indicated
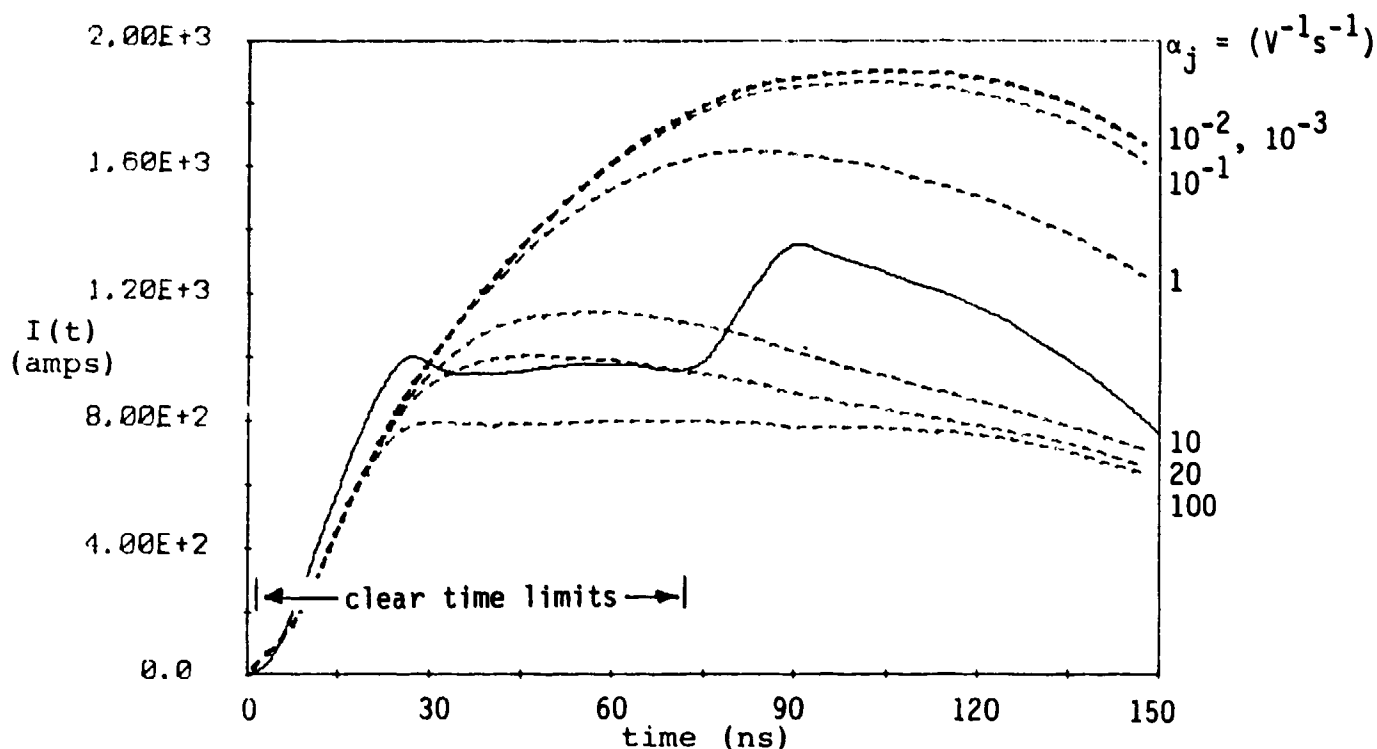
Figure 41. Comparison of Measured (——) and Townsend
Model (---) Results:

E_c = 3.5 MV/m; α_j Variations as Indicated

66
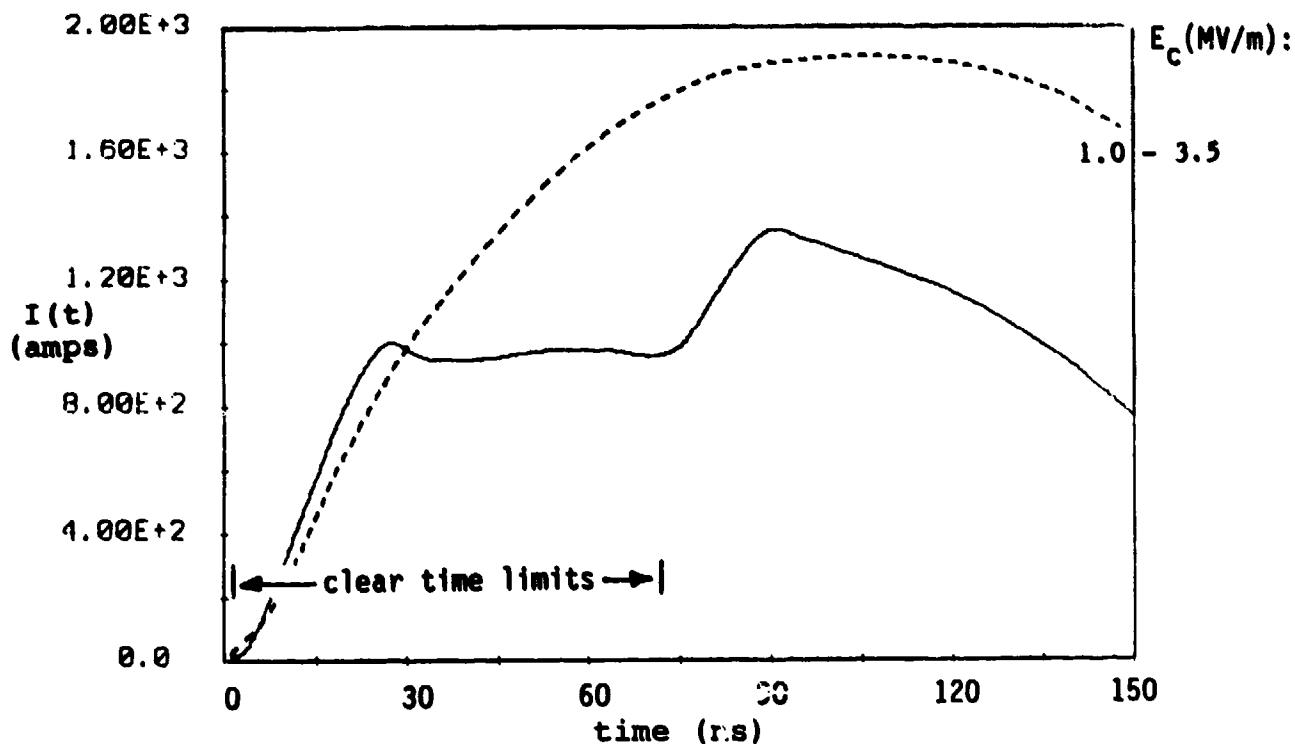
Figure 42. Comparison of Measured (———) and Townsend Model (---) Results:

$\alpha_j = 0.001$ $V^{-1}s^{-1}$; E_c Variations as Indicated
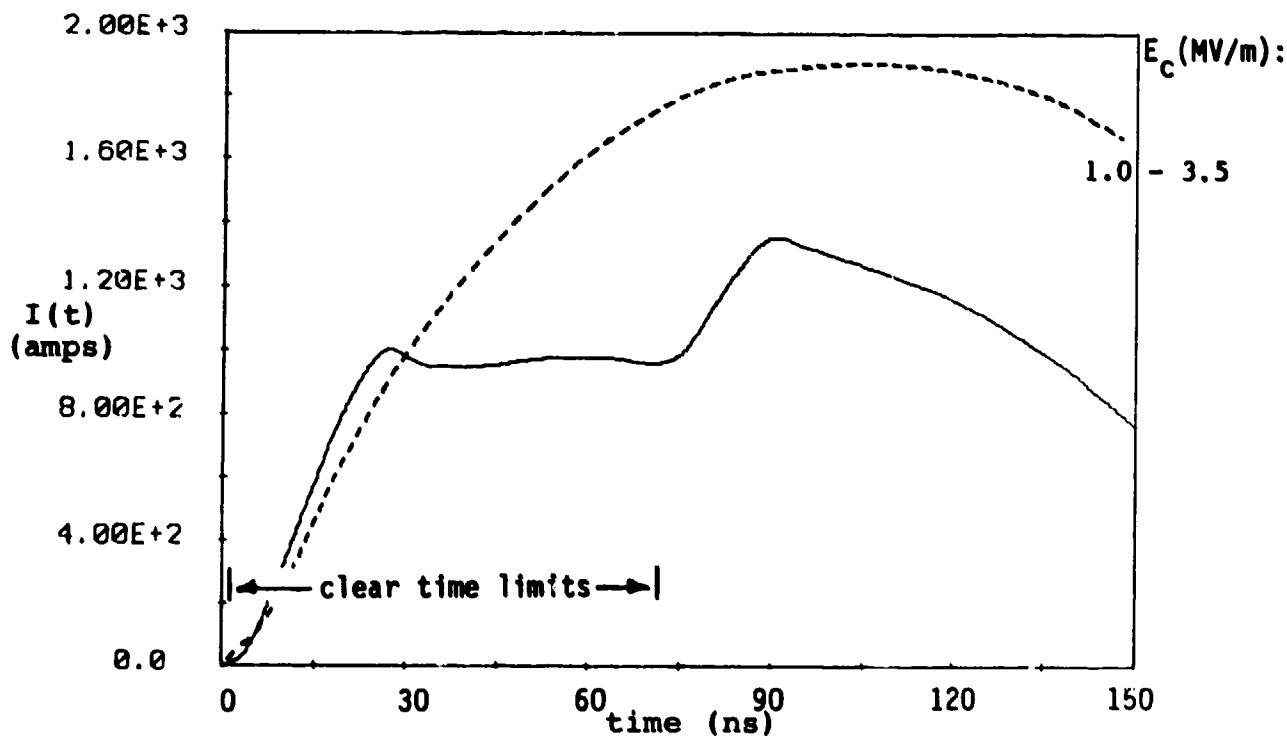
Figure 43. Comparison of Measured (———) and Townsend Model (---) Results:

$\alpha_j = 0.01$ $V^{-1}s^{-1}$; E_c Variations as Indicted
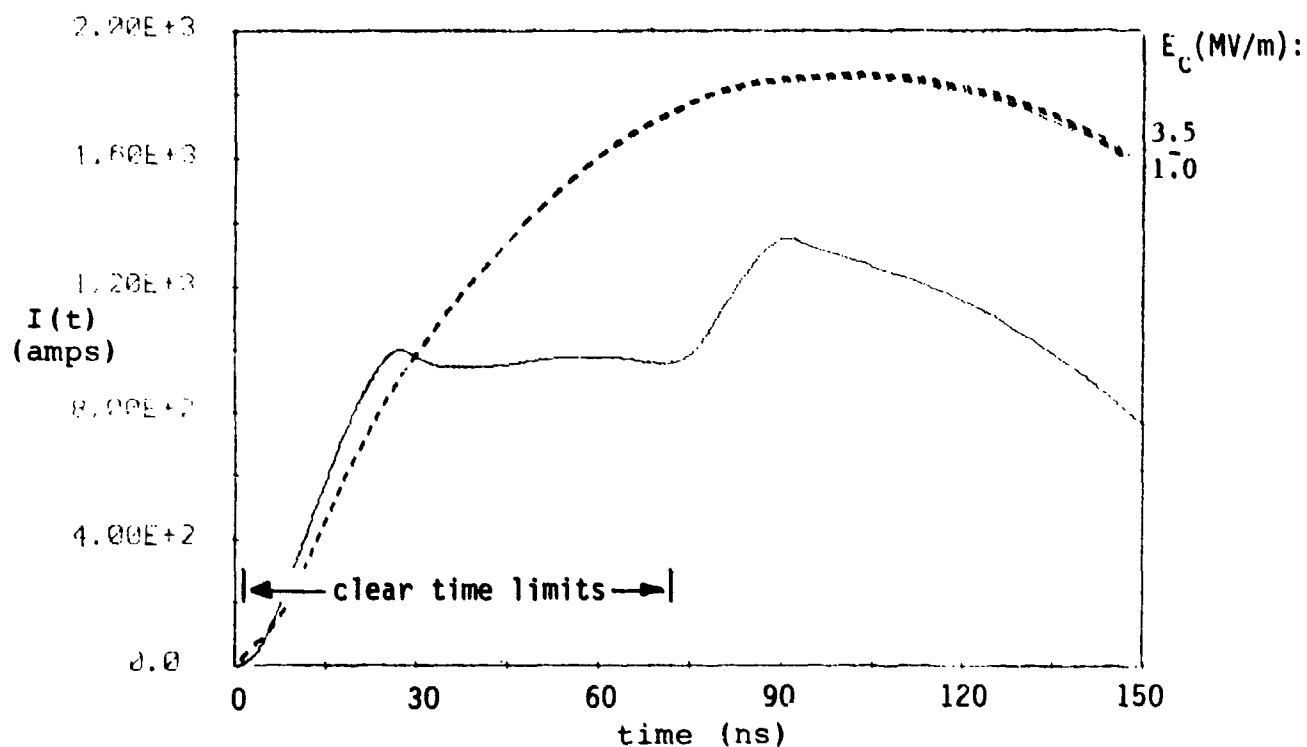
Figure 44. Comparison of Measured (——) and Townsend
Model (---) Results:

$\alpha_j = 0.1\ V^{-1}s^{-1}$; E_c Variations as Indicated
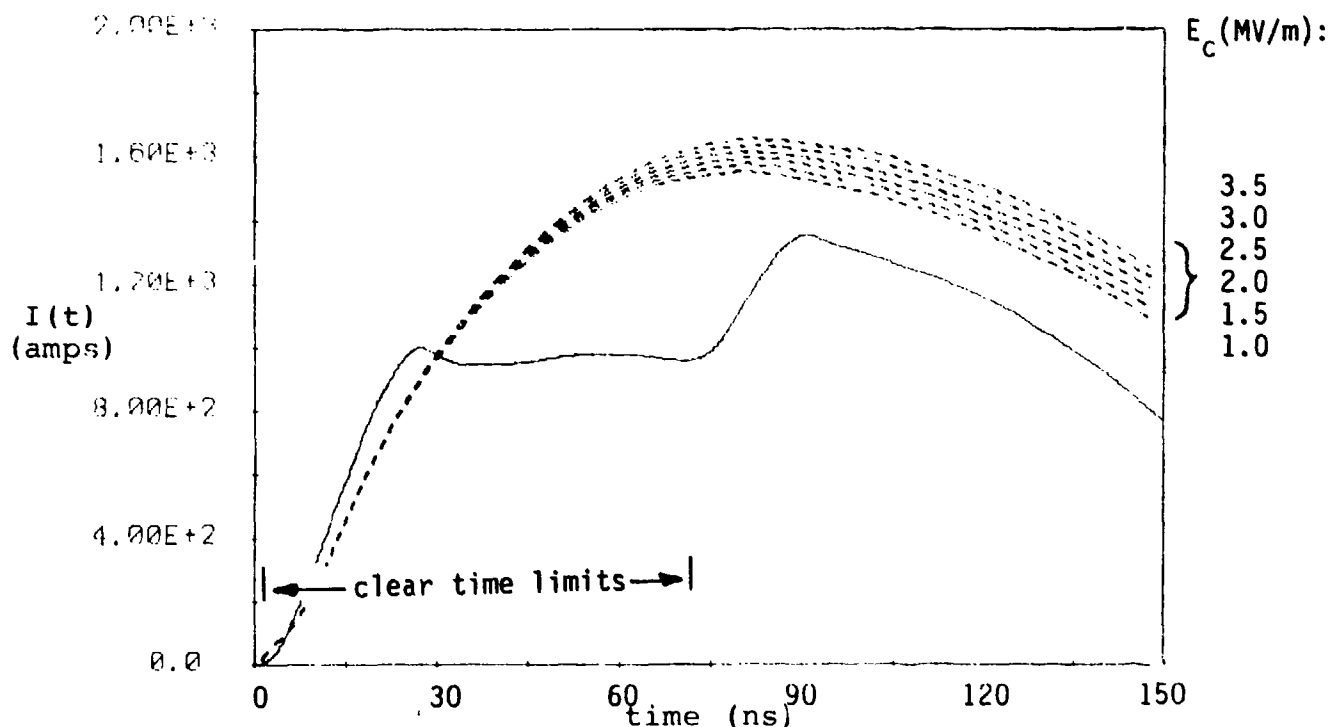
Figure 45. Comparison of Measured (——) and Townsend
Model (---) Results:

$\alpha_j = 1\ V^{-1}s^{-1}$; E_c Variations as Indicated
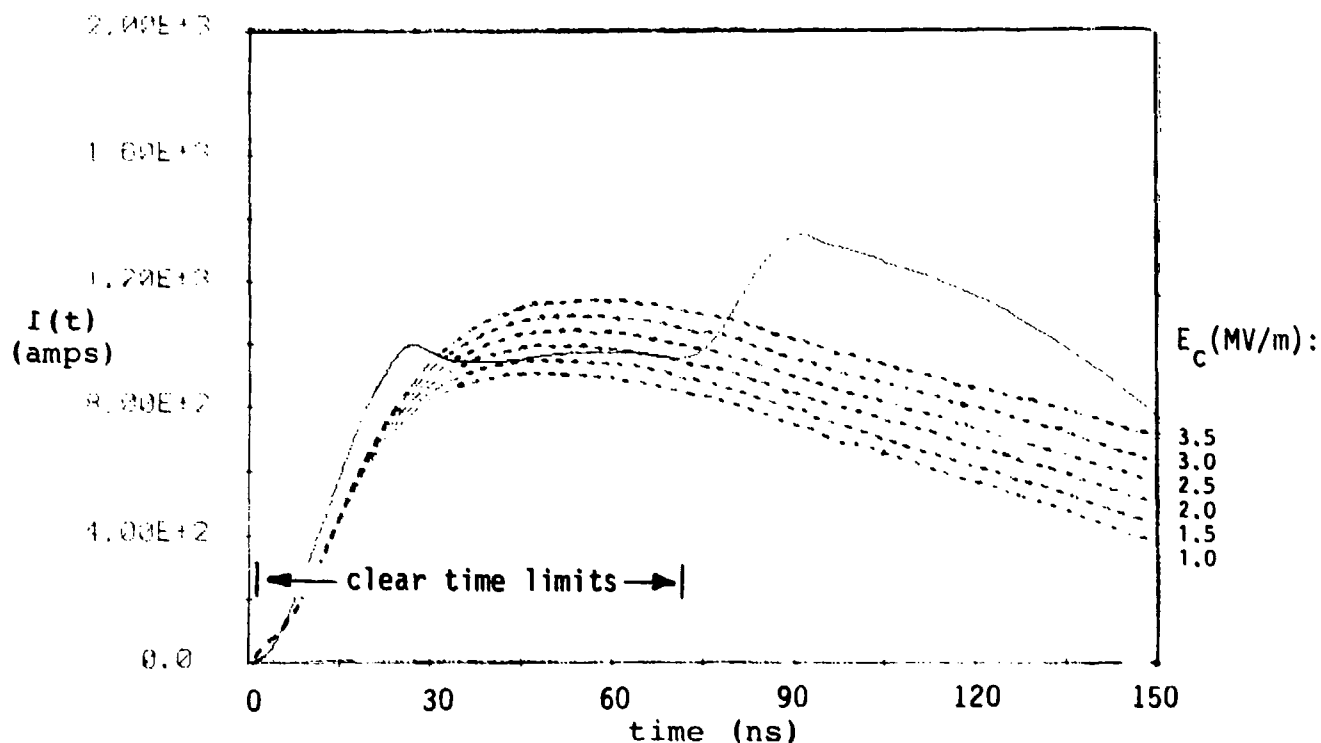
Figure 46. Comparison of Measured (——) and Townsend Model (---) Results:
$\alpha_j = 10 \text{ V}^{-1}\text{s}^{-1}$; E_c Variations as Indicated
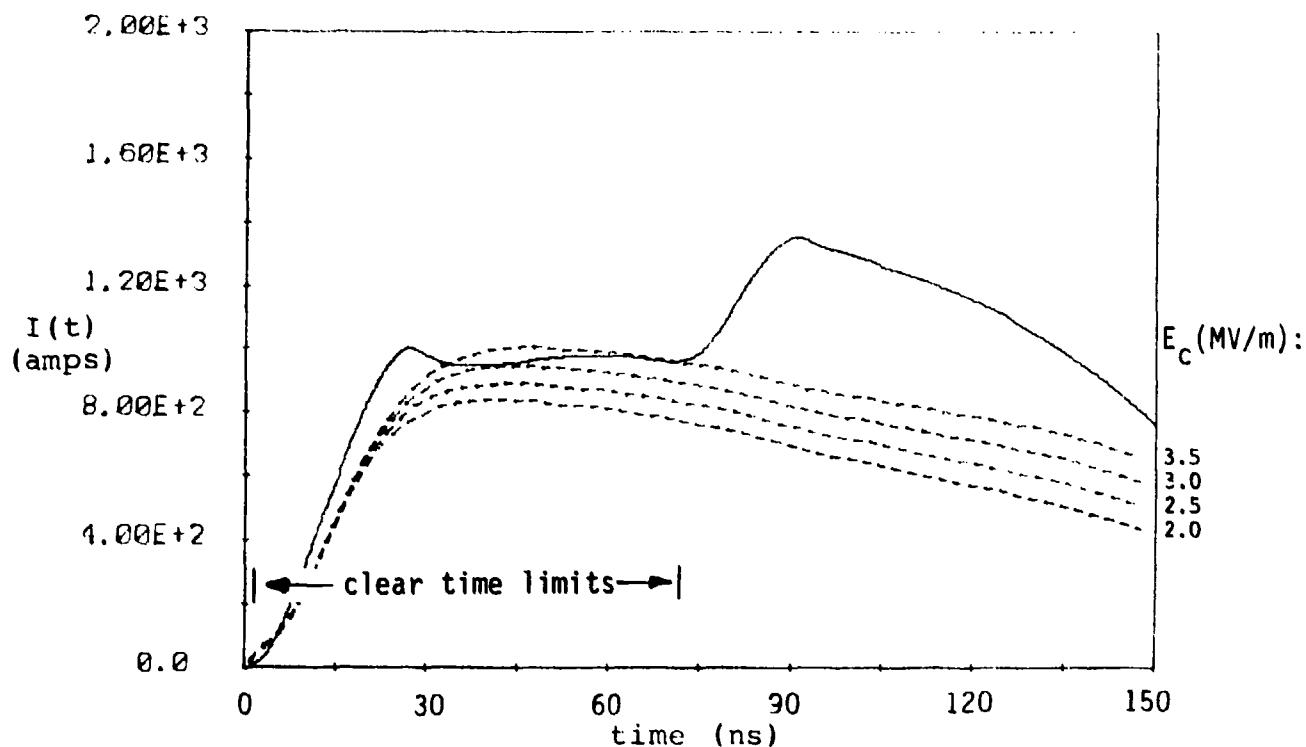
Figure 47. Comparison of Measured (——) and Townsend Model (---) Results:
$\alpha_j = 20 \text{ V}^{-1}\text{s}^{-1}$; E_c Variations as Indicated
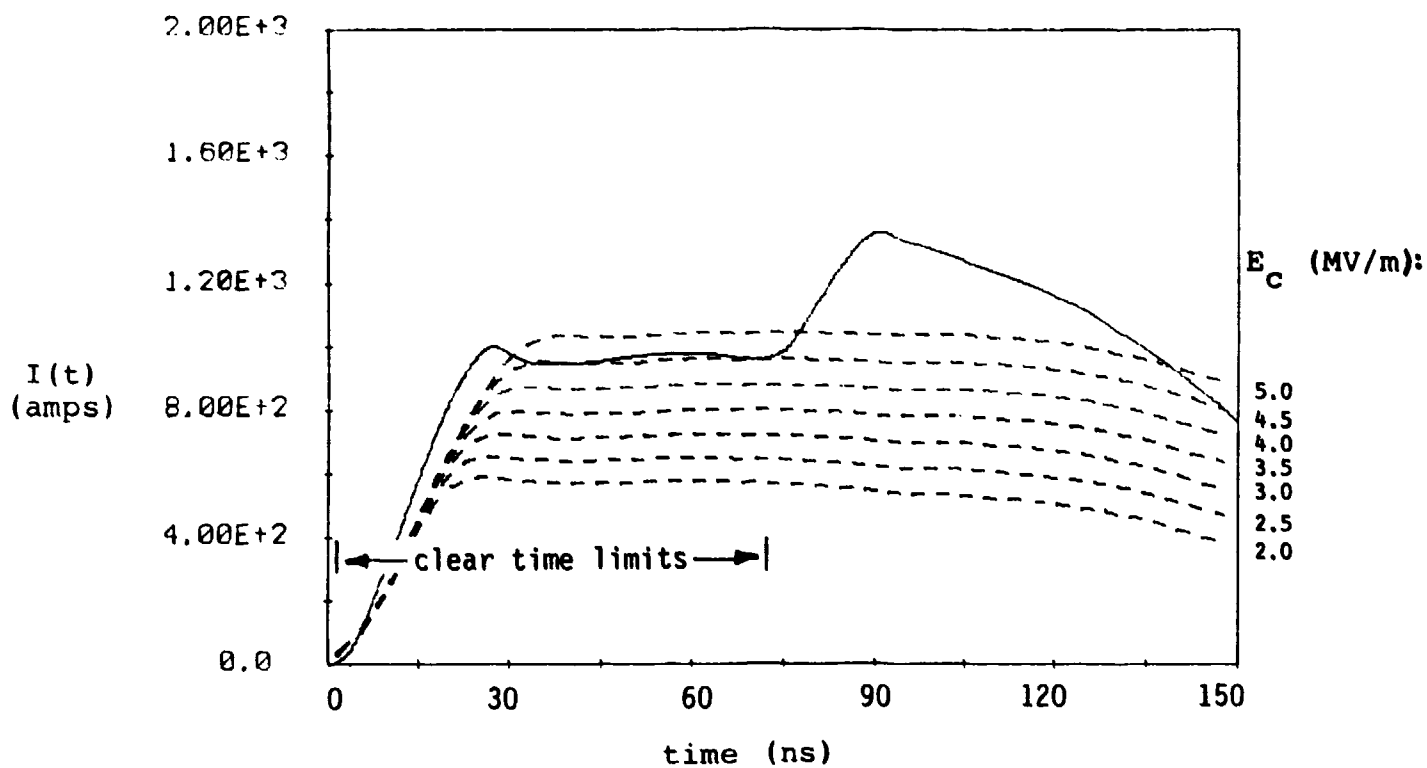
Figure 48. Comparison of Measured (——) and Townsend
Model (---) Results:
$\alpha_j = 100 \ V^{-1}s^{-1}$; E_C Variations as Indicated

b. Discussion of Results

The following is a discussion of the numerical studies made for the Townsend corona model:

<u>Variables</u>:

E_c E-field value at which breakdown occurs

α_j "Townsend ionization coefficient", essentially a measure of the efficiency of the avalanche process in generating successive electron-ion pairs (i.e. pairs that do not readily recombine, since those would not be part of the corona formation)

<u>Limitations</u>:

Peek's law constrains 2.5×10^6 V/m $< E_c < 4.5 \times 10^6$ V/m.

In Townsend's original model, α_j would equal 6.03×10^{-4} $V^{-1}s^{-1}$ for this test geometry. The transient nature of the driving E-field used here invalidates some of the assumptions leading to this value, and a dimensionless parameter α_{jc} (see Reference [7]) is introduced to fit the model to the results obtained experimentally. In the original Townsend model, $\alpha_{jc} = 1.0$. Reference [7] makes no

71

restrictions on the value of α_{jc} . Instead, nominal values
are suggested for α_j .

Variations tested:

E_c: 1.0 x 10^6, 1.5 x 10^6, 2.0 x 10^6, 2.5 x 10^6,
3.0 x 10^6, 3.5 x 10^6 (all in V/m)

α_j: 10^{-3}, 10^{-2}, 10^{-1}, 1, 5, 10, 20, 100 (all in $V^{-1}s^{-1}$)

Results:

From the graphs in Figures 36-41, one can see that for a
constant value of E_c , larger values of α_j lead to greater
suppression of the induced current seen on the line. In fact,
α_j = 100 $V^{-1}s^{-1}$ provides the best fit of the model to the
general form of the experimental data.

Holding α_j constant while varying E_c is demonstrated
in Figures 39-45. For smaller values of α_j , variations in
E_c show no effect (see Figures 42 and 43). For α_j > 0.1
$V^{-1}s^{-1}$, some "fanning" of the response curves can be seen,
with the results for higher E_c values demonstrating smaller
current suppression. This might be expected since as E_c
increases, the air will support greater field strengths and,

hence, greater induced currents on the test line, before
corona formation begins. The best fit of the model to the
data may be seen in Figure 48 where $\alpha_j = 100.0 \text{ V}^{-1}\text{s}^{-1}$. Here,
the range of E_c was extended beyond the range indicated above
and a surprisingly good fit was found when $E_c = 4.5$ MV/m.

D. The Mo Corona Model

1. Theory

The corona model developed by T.C. Mo and described in
reference [16] is different from the others in that the
details of the physics of the corona formation are used in
developing the solution. (Only the salient features of this
model will be summarized here, and the reader is referred to
the original report for a more detailed derivation of the
theory.)

The Mo model assumes that transmission line theory is
sufficient for describing the propagation of the current and
charge along the line. The telegrapher's equations used by Mo
can be put into our standard form as

$$\frac{\partial V}{\partial z} + L' \frac{\partial I}{\partial t} = E_z^{inc} \tag{19a}$$

and

$$\frac{\partial I}{\partial z} + C' \frac{\partial v}{\partial t} = F(v) \quad , \tag{19b}$$

where L' is defined as in equations (2) and (3) and C' is a constant given by equation (4).

Note that in Mo's original formulation, the factor of 2 in the logarithm term was omitted. In addition, in Mo's development, the term v is frequently referred to as the line voltage which, according to the discussions in reference [6], must have an additional contribution from the vertical component of the incident electric field. Actually, the term v used here is a measure of the local charge on the wire, as previously discussed.

In the Mo model, the effective source term in equation (19b) is shown to be:

$$F(v) = -g(v) v \quad , \tag{20}$$

where g(v) is a nonlinear conductance given by the relation

$$g(v) = \frac{s}{(a_c(v) - a_w)} \left[\frac{\ln (a_c(v)/a_w)}{\ln (2h/a_w)} \right]^2 \quad . \tag{21}$$

74

This term could have been moved to the left hand side of equation (19b) and treated as part of the unknown, but it is permissible to consider it as a "source" term and use the same calculational algorithm as used in the solution of the Engheta-Lee models.

In equation (21), a_c represents the effective corona radius and is determined in the same manner as in the Baum model, namely

$$a_c = \frac{|Q'|}{2\pi \, \epsilon_o \, E_c} \qquad \left[= \frac{v}{2\pi \, E_c} \right] \; .$$ (6)

The term s in equation (21) is an effective conductivity of the corona, and is itself a nonlinear, time dependent function of the local electric field in the corona. In this model, the behavior of the parameter s is determined by a rate equation of the form

$$\frac{ds}{dt} = \alpha(E_\rho', p) \, \mu_e \, |E_\rho'| \, s \quad ,$$ (22)

where E_ρ' is the radial electric field at the corona boundary and is given by

$$E_\rho' = \frac{v}{\ln(2h/a_w)} \quad \frac{\ln(a_c/a_w)}{(a_c - a_w)} \tag{23}$$

The term $\alpha(E_\rho', p)$ is an approximate empirical formulation of the Townsend ionization coefficient given by

$$\alpha(E_\rho', p) = 990.0 \, p \, \exp -(2.72 \times 10^4 \, p/E_\rho') \cdot \exp(\xi) \tag{24}$$

$$\text{with} \quad \xi = (0.042 \, (2.72 \times 10^4 \, p/E_\rho' - 3.4)^2)) \quad , \tag{24a}$$

where p is the ambient air pressure in mm-Hg, and μ_e is the electron mobility, estimated to be on the order of 0.275 m^2/v-s [24].

The solution of the line current using this model, therefore, involves solving equations (19a) and (19b) in conjunction with the rate equation (22) at each time step. In order to begin the solution, it is necessary to specify an initial value for the parameter s (denoted by s_o). This is a quantity that may be specified independently of other parameters, and thus, can be regarded as a "tuning" parameter for the corona model.

Assuming that the air pressure is fixed at 621 mm-Hg (ambient or station (i.e. not corrected to STP) barometric pressure measured by National Weather Service at the time and for the altitude at which the baseline corona measurements were made), the only other free parameters in this model are the line height h and the critical electric field strength E_c. For the parametric study using the Mo model, the parameter h was held constant at 20 meters since the response is not extremely sensitive to this parameter, and s_o and E_c were varied. Figures 49 through 60 present the results predicted by this model compared with those acquired for the experiment baseline geometry.
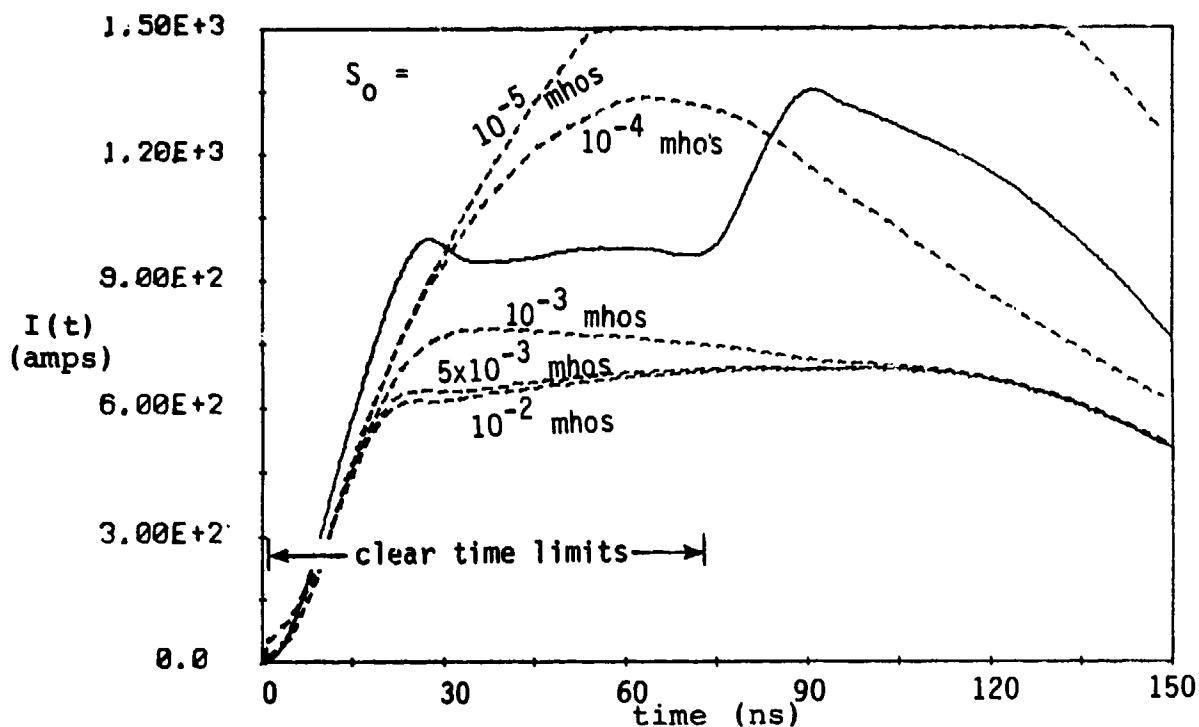
Figure 49. Comparison of Measured (——) and Mo Corona
Model (---) Results:

$\mu_e = 2 \times 10^{-4} \ m^2/V\text{-}s$; $E_c = 3 \ MV/m$; S_o as Indicated
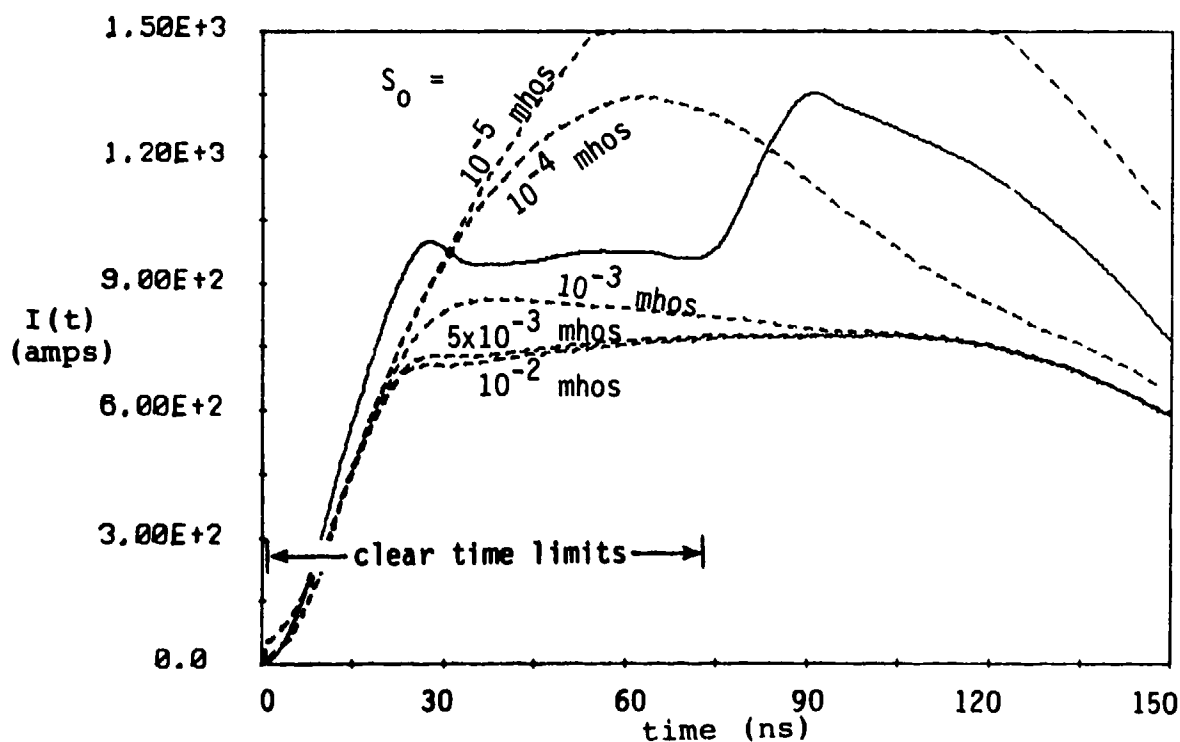
Figure 50. Comparison of Measured (——) and Mo Corona
Model (---) Results:

$\mu_e = 2 \times 10^{-4} \ m^2/V\text{-}s$; $E_c = 3 \ MV/m$; S_o as Indicated

78
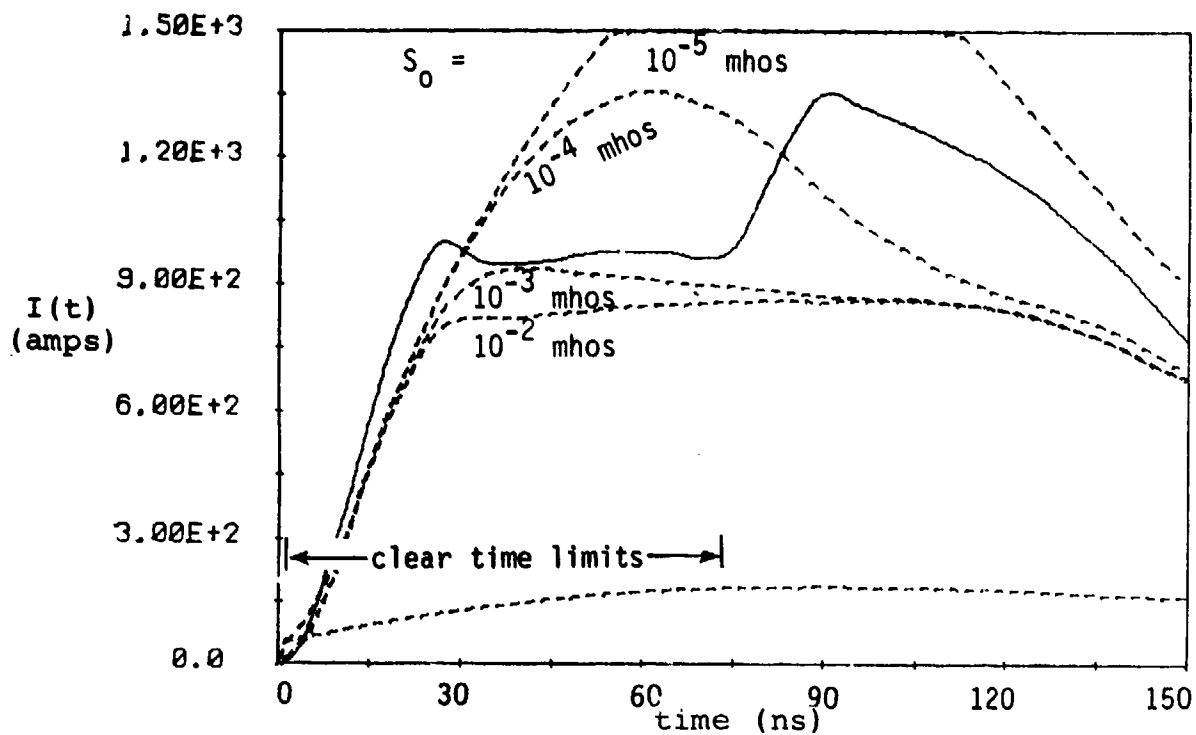
Figure 51. Comparison of Measured (——) and Mo Corona
Model (---) Results:

$\mu_e = 2 \times 10^{-4}$ m^2/V-s; $E_c = 4.0$ MV/m; S_o as Indicated
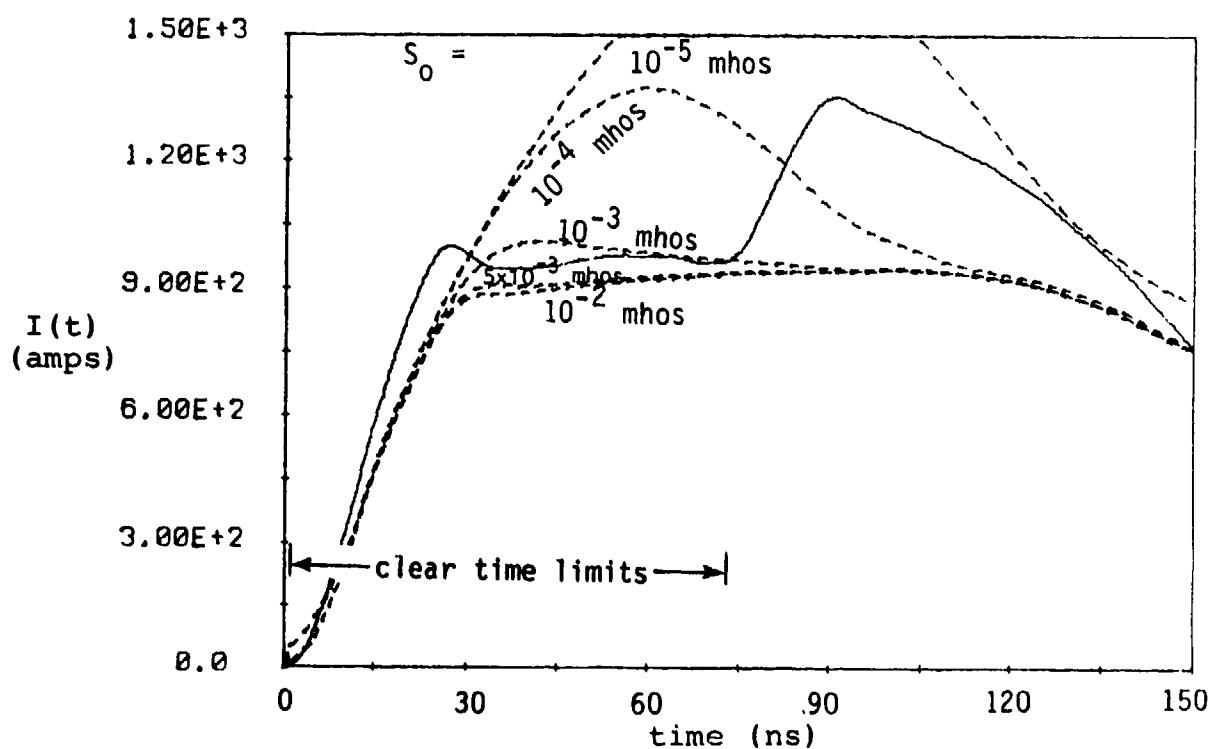
Figure 52. Comparison of Measured (——) and Mo Corona
Model (---) Results:

$\mu_e = 2 \times 10^{-4}$ m^2/V-s; $E_c = 4.5$ MV/m; S_o as Indicated
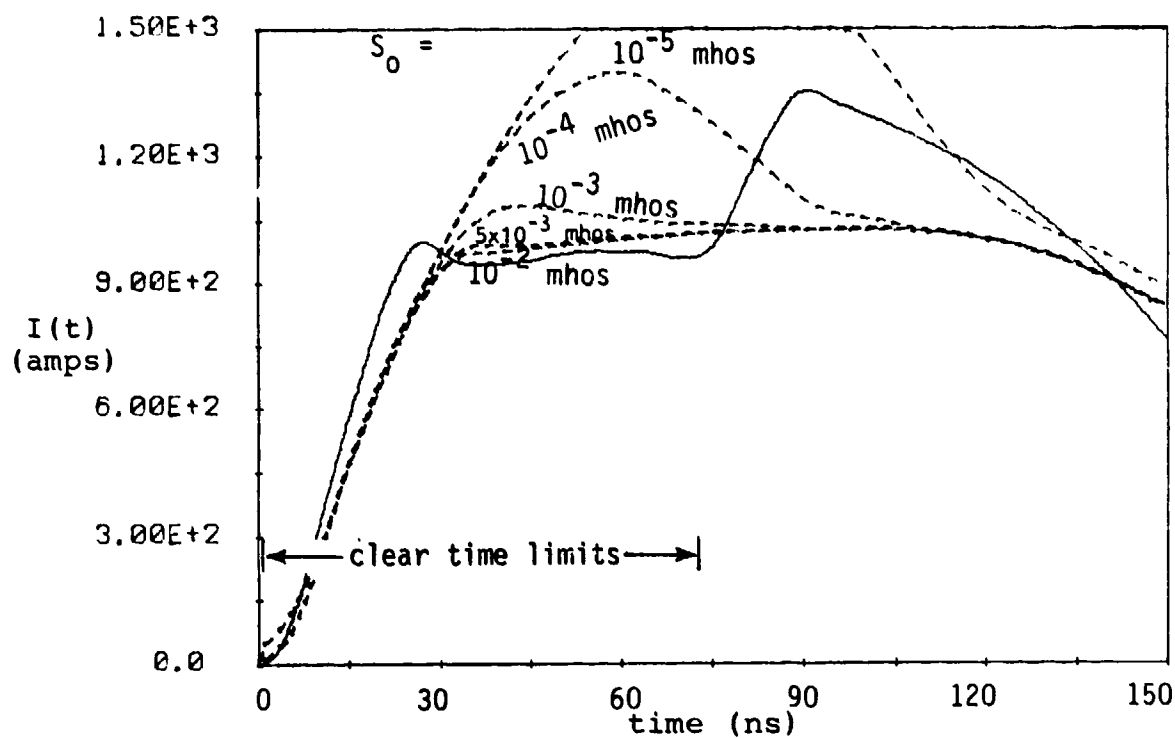
Figure 53. Comparison of Measured (———) and Mo Corona
Model (---) Results:
$\mu_e = 2 \times 10^{-4}$ m^2/V-s; $E_c = 5.0$ MV/m; S_o as Indicated
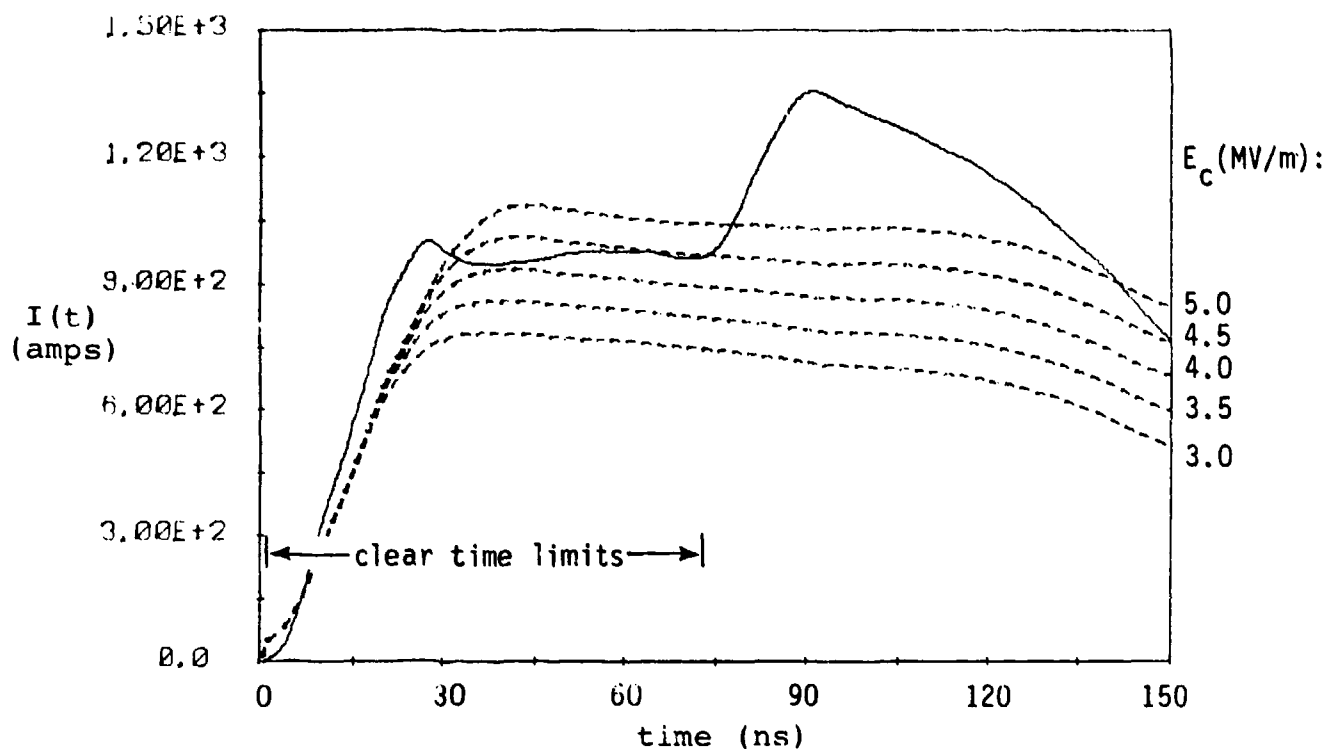
Figure 54. Comparison of Measured (——) and Mo Corona
Model (———) Results:

$\mu_e = 2 \times 10^{-4}$ m^2/V-s; $S_o = 10^{-3}$ mhos; F_c as Indicated
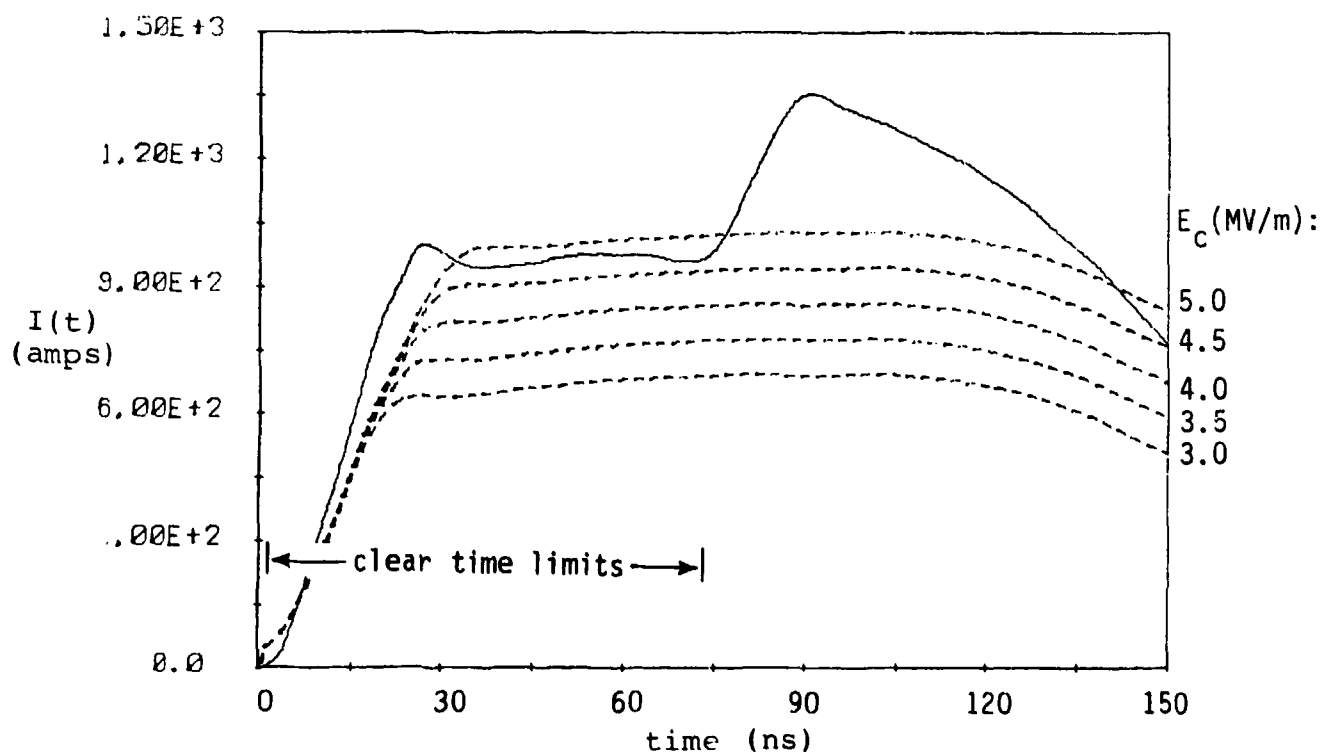
Figure 55. Comparison of Measured (——) and Mo Corona
Model (———) Results:

$\mu_e = 2 \times 10^{-4}$ m^2/V-s; $S_o = 5 \times 10^{-3}$ mhos; E_c as Indicated

81
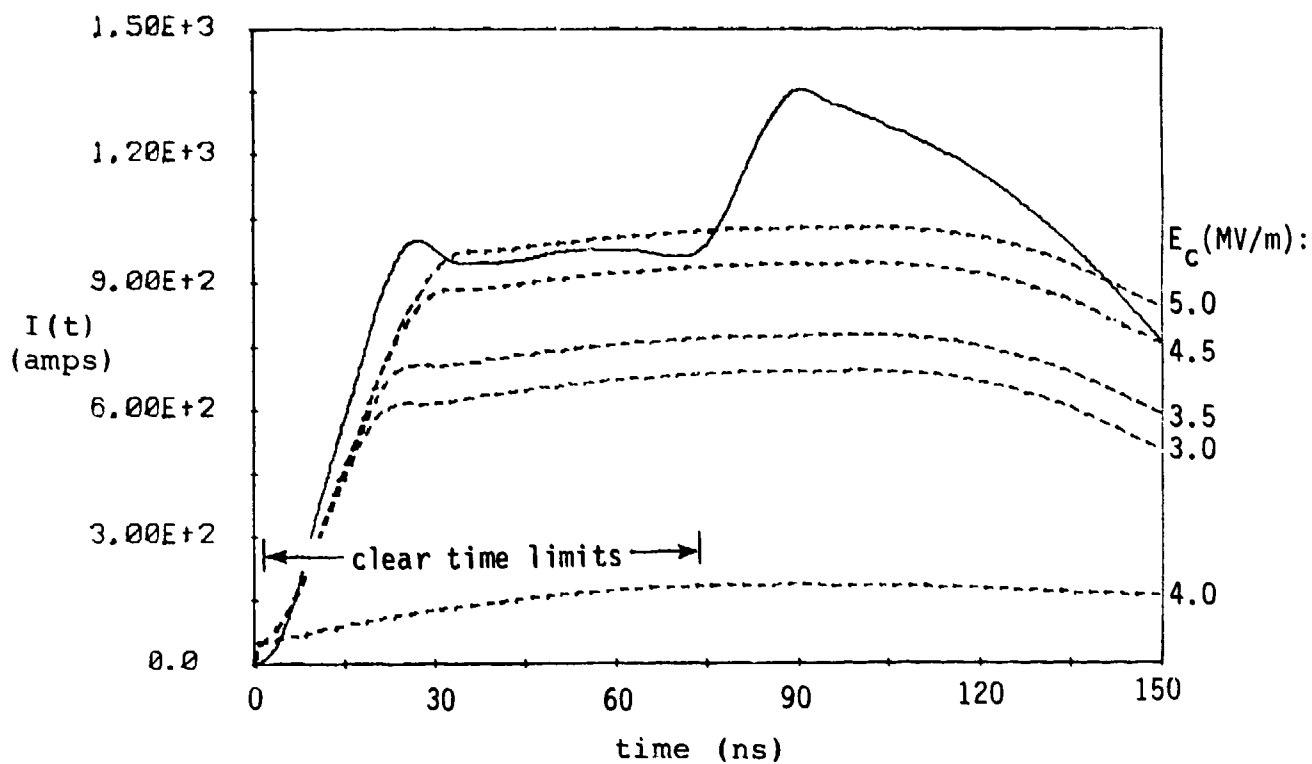
Figure 56. Comparison of Measured (——) and Mo Corona
Model (---) Results:

$$\mu_e = 2 \times 10^{-4} \ m^2/V\text{-}s; \ S_o = 10^{-2} \ mhos; \ E_c \ as \ Indicated$$
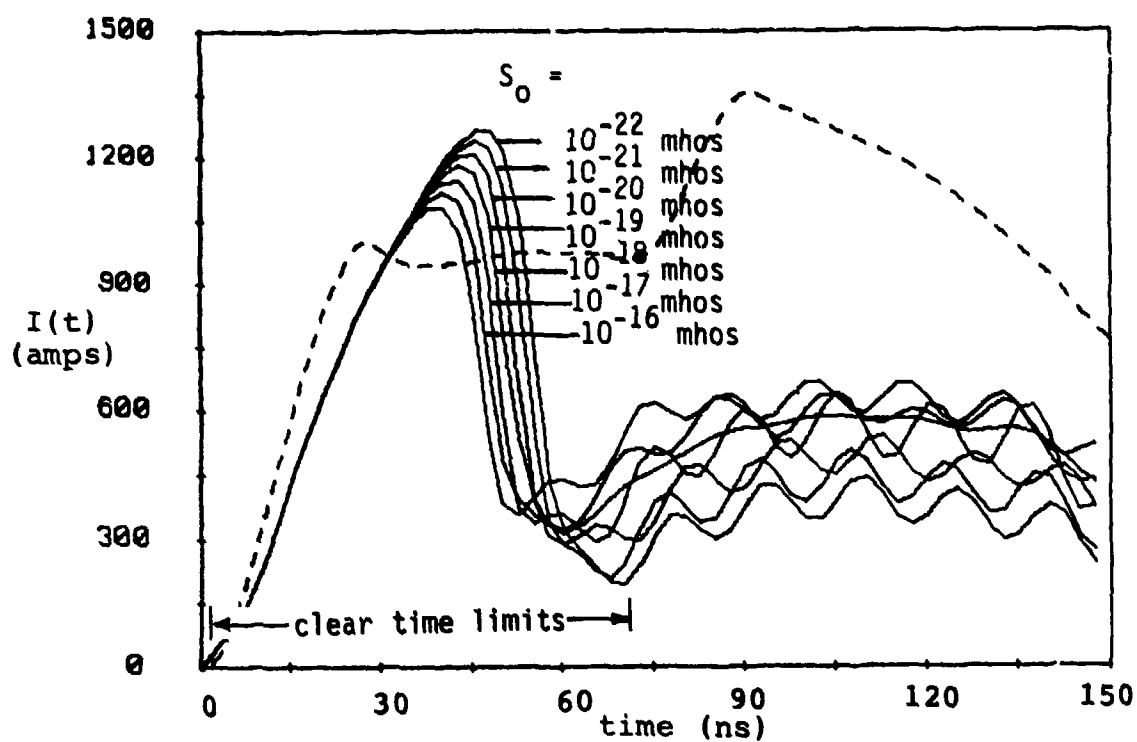
Figure 57. Comparison of Measured (·····) and Mo Corona Model (━━) Results:
$\mu_e = 0.275$ m^2/V-s; $E_c = 3$ MV/m; S_o as Indicated
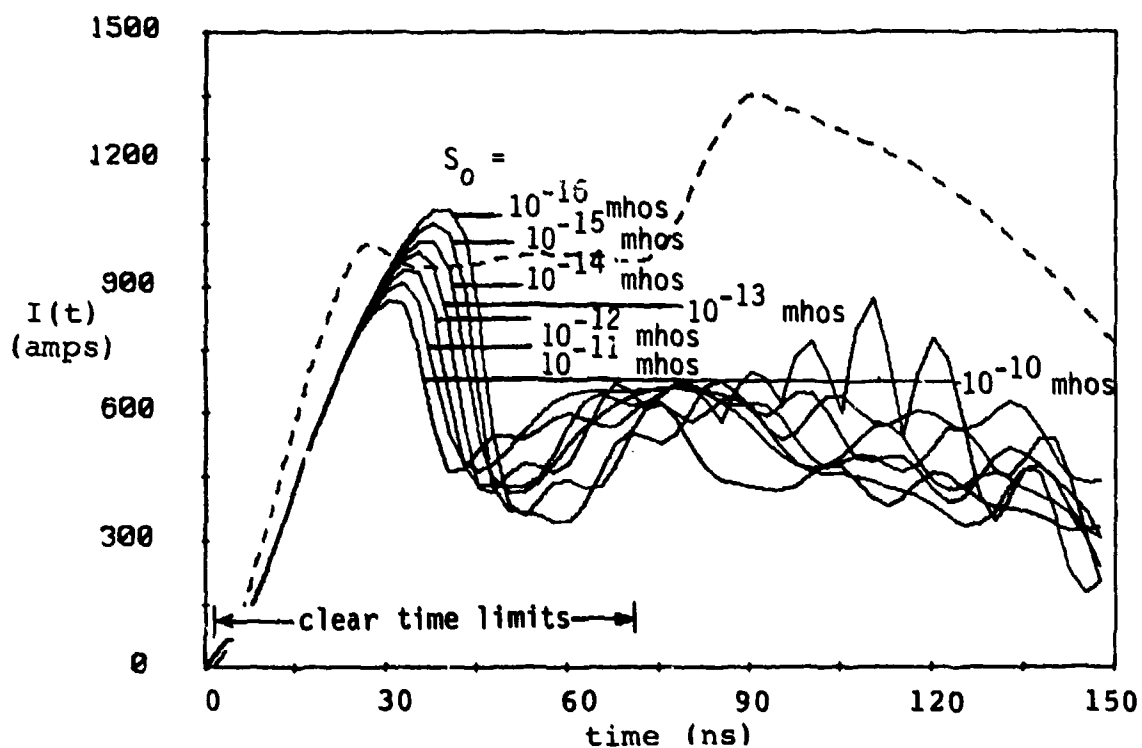
Figure 58. Comparison of Measured (·····) and Mo Corona Model (━━) Results:
$\mu_e = 0.275$ m^2/V-s; $E_c = 3$ MV/m; S_o as Indicated

83
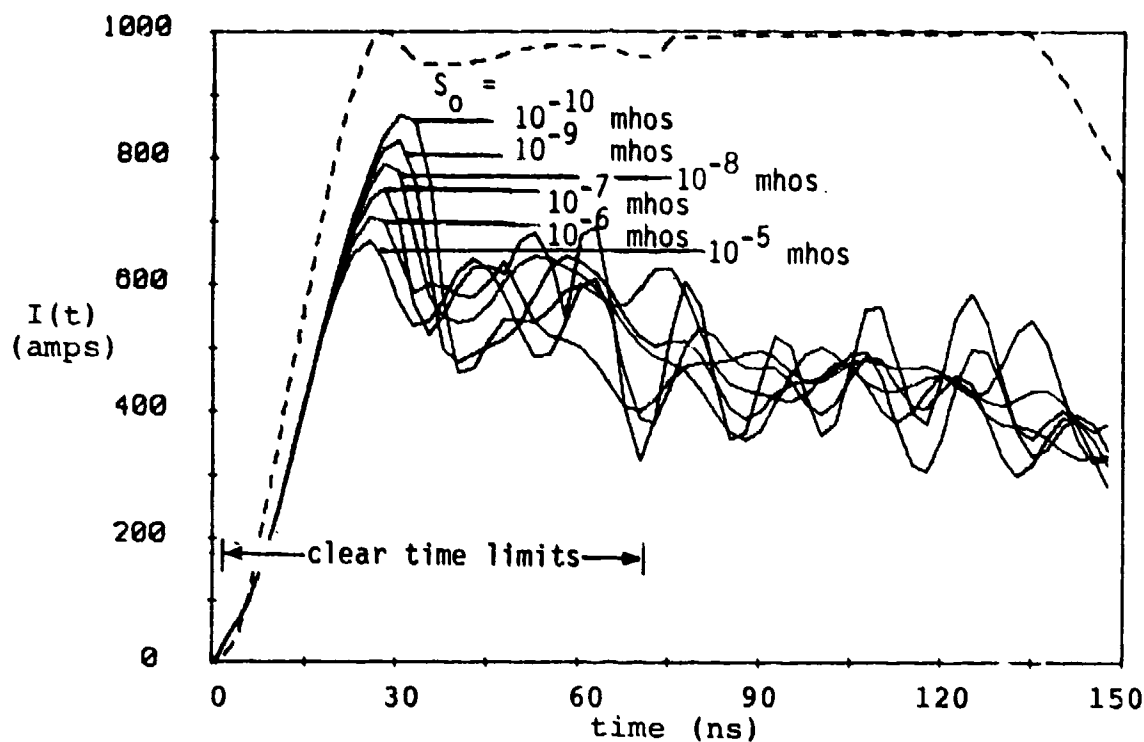
Figure 59. Comparison of Measured (----) and Mo Corona Model (——) Results:

$\mu_e = 0.275$ m^2/V-s; $E_c = 3$ MV/m; S_o as Indicated
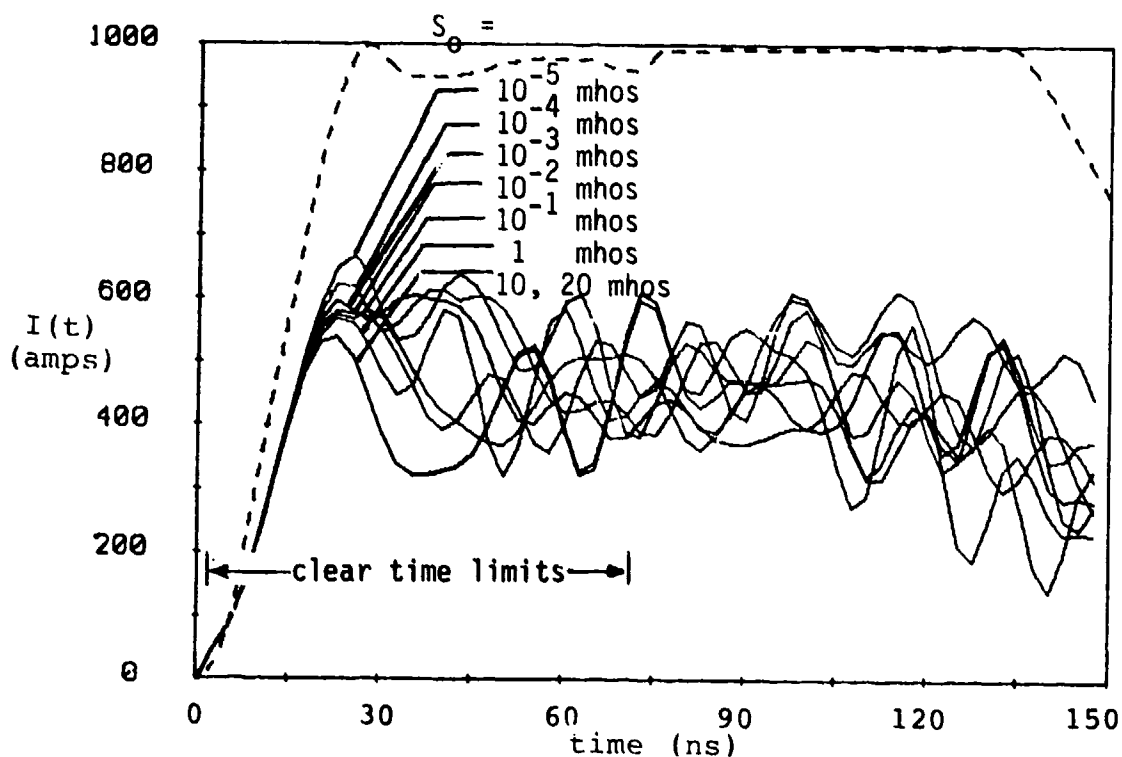
Figure 60. Comparison of Measured (-----) and Mo Corona Model (——) Results:

$\mu_e = 0.275$ m^2/V-s; $E_c = 3$ MV/m; S_o as Indicated

2. Discussion of Results

Variables:

E_c E-field value at which breakdown occurs

s_o parameter related to initial value of air
conductivity

Limitations:

Peek's law constrains 2.5×10^6 V/m $< E_c < 4.5 \times 10^6$ V/m.

As indicated for the conductivity model, air conductivity
during corona is very difficult to measure since it is a
function of many parameters including amount and polarity of
ionization, local pressure, and relative humidity.
Alternatively, it is a function of the mobility and number
density of the charge carriers. Here, two values were tried
for the mobility of the charge carriers: 0.275 (for electrons)
and 0.0002 (for ions) [24] (both values given in
$meters^2$/volt-second and representing typical mobilities for
electrons and ions, respectively). An empirical formula for
Townsend's ionization coefficient was formulated to fit the
data of von Engel [16].

85

<u>Variations tested</u>:

E_c: 3.0×10^6, 3.5×10^6, 4.0×10^6, 4.5×10^6 (all in V/m)

s_o: 10^{-3}, 10^{-4}, 10^{-5} (all in mhos or Siemens)

<u>Results</u>:

Originally, an ion mobility [24] of $\mu_{ion} = 0.0002$ m^2/V-s was tried in the Mo model (see Figures 49 - 56). This value is approximately correct for both positive and negative ions. Here, however, it was anticipated that the primary charge carriers were positive. It was hypothesized that the test line became positively charged as a result of its interaction with the simulated EMP. Electrons appearing very near the wire were quickly sucked into the wire and the displacement current noted during corona is anticipated to be due primarily to positive ions moving away from the wire [20]. The results obtained using such a mobility (see Figures 49-56) fit the acquired data almort as well as did those of the conductivity model.

Alternatively, a mobility characteristic of electrons [24] ($\mu_e = 0.275$ m^2/V-s) was also tried. If the line was indeed

charged positively, it was conjectured that electrons might actually be the charge carriers of interest [20]. In the model used, numerical instabilities developed in the late time portions of the curves (see Figures 57-60) and the fit to the acquired data was in general quite poor.

E. The Kudyan-Shih Corona Model

1. Theory

The model proposed by Kudyan and Shih [13] for investigating the propagation of surges on a line with corona involves modeling the corona by a nonlinear circuit. The v-i propagation relations along the wire assumed by these authors are of the following form:

$$\frac{\partial v}{\partial z} = -L' \frac{\partial i}{\partial t} \tag{25a}$$

and

$$\frac{\partial i}{\partial x} = -\frac{\partial Q'}{\partial t} \tag{25b}$$

where Q' is the charge per-unit-length on the wire, and is related to the voltage on the wire (with respect to the ground-plane) as

$$Q'(z,t) = C'(z,t) \, v(z,t) \quad . \tag{25c}$$

C' is an effective nonlinear capacitance. Kudyan and Shih postulate that the circuit model shown in Figure 58 adequately describes the Q-v relationship along the wire, and that a simple circuit analysis can be used to determine the effective line and corona capacitance at any time and position.

In applying this approach to the distributed field excitation of the line, we again define the local variable $v \equiv Q'/C'$ and write the forced telegrapher's equations as in equations (9a) and (9b), where the v-Q relationship for the corona region is assumed to be described by the circuit presented in Figure 61. In this figure there are two parallel nonlinear circuits representing the effects of a positive and negative corona. The batteries labeled as V_c account for the air breakdown electric field thresholds. In this model, the values are assumed to be identical for the positive and negative coronas. The resistance and capacitance values of the nonlinear elements are not determined from first principles, but estimated from comparisons with experimental line

$$V_+(t) = V_2(t) + V_c$$

$$V_-(t) = V_3(t) - V_c$$
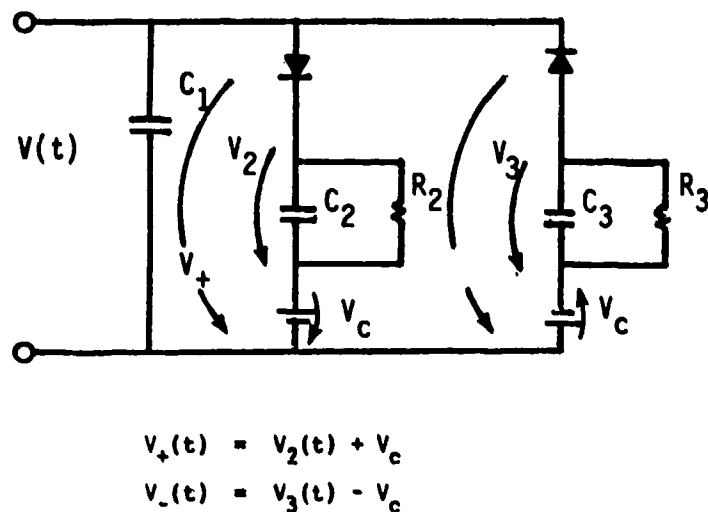
(a) Nonlinear model circuit for an element of line in corona
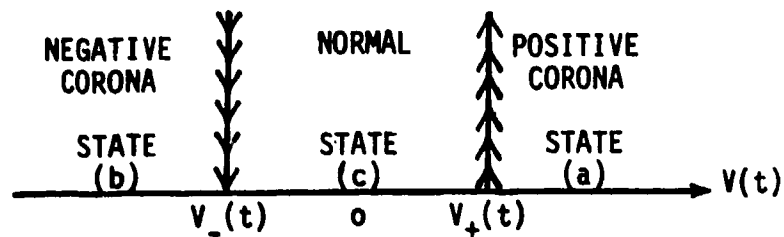
(b) At a given instant, the circuit will be in one of three
     possible states (negative corona, normal, or positive corona).

Figure 61. Circuit Model for Element of Transmission
            Line in Kudyan-Shih Corona Model

89

responses. For simplicity, it is assumed $R_1 = R_2$ and $C_1 = C_2$ although in reality these values may be expected to differ from each other.

As discussed in [13], the circuit can be in one of three states, depending on the voltage of the line and the past history of the line. By defining a positive corona model voltage v^+ as

$$v^+(t) = v_2(t) + V_C \ , \tag{26}$$

where v_2 represents the voltage across the corona capacitance C_2, and a corresponding negative corona model voltage

$$v^-(t) = v_3(t) - V_C \ , \tag{27}$$

it is possible to define the three corona states and the voltages across the capacitive elements as follows:

<u>For $v(t) > v^+(t)$:</u>   (positive corona state)

$$v_2(t) = v_2(t-\Delta t) + [v(t)-V_C-v_2(t-\Delta t)] \ (1-e^{-\Delta t/(R_2 C_2)}) \tag{28}$$

$$v_3(t) = v_3(t-\Delta t) \ e^{-\Delta t/(R_3 C_3)}) \ . \tag{29}$$

For $v(t) < v^-(t)$:   (negative corona state)

$$v_2(t) = v_2(t-\Delta t) \, e^{-\Delta t/(R_2 C_2)}) \tag{30}$$

and

$$v_3(t) = v_3(t-\Delta t) + [v(t)-V_c-v_3(t-\Delta t)] \, (1-e^{-\Delta t/(R_3 C_3)}) \ . \tag{31}$$

For $v^-(t) < v(t) < v^+(t)$:   (normal state)

$$v_2(t) = v_2(t-\Delta t) \, e^{-\Delta t/(R_2 C_2)}) \tag{32}$$

and

$$v_3(t) = v_3(t-\Delta t) \, e^{-\Delta t/(R_3 C_3)}) \ . \tag{33}$$

With a knowledge of the voltage across each of the capacitors in the model, it is possible to write the total charge per-unit-length stored as

$$Q'(t) = C_1' v(t) + C_2' v_2(t) + C_3' v_3(t) \ . \tag{34}$$

The above expression for the charge can be separated into a constant capacitance term involving C_1' and the

remaining terms. This permits the equations (9) to be re-written as though they contained source terms as:

$$\frac{\partial V}{\partial z} + L' \frac{\partial I}{\partial t} = E_z^{inc} \qquad (35a)$$

and

$$\frac{\partial I}{\partial z} + C_1' \frac{\partial V}{\partial t} = -\frac{\partial}{\partial t}\left[C_2' v_2(t) + C_3' v_3(t) \right] \qquad (35b)$$

and the finite-difference, time marching solution developed for the previous models can be used to obtain a solution for the line current.

Figures 62 through 71 present some of the results of a variation of parameters study for this corona model.
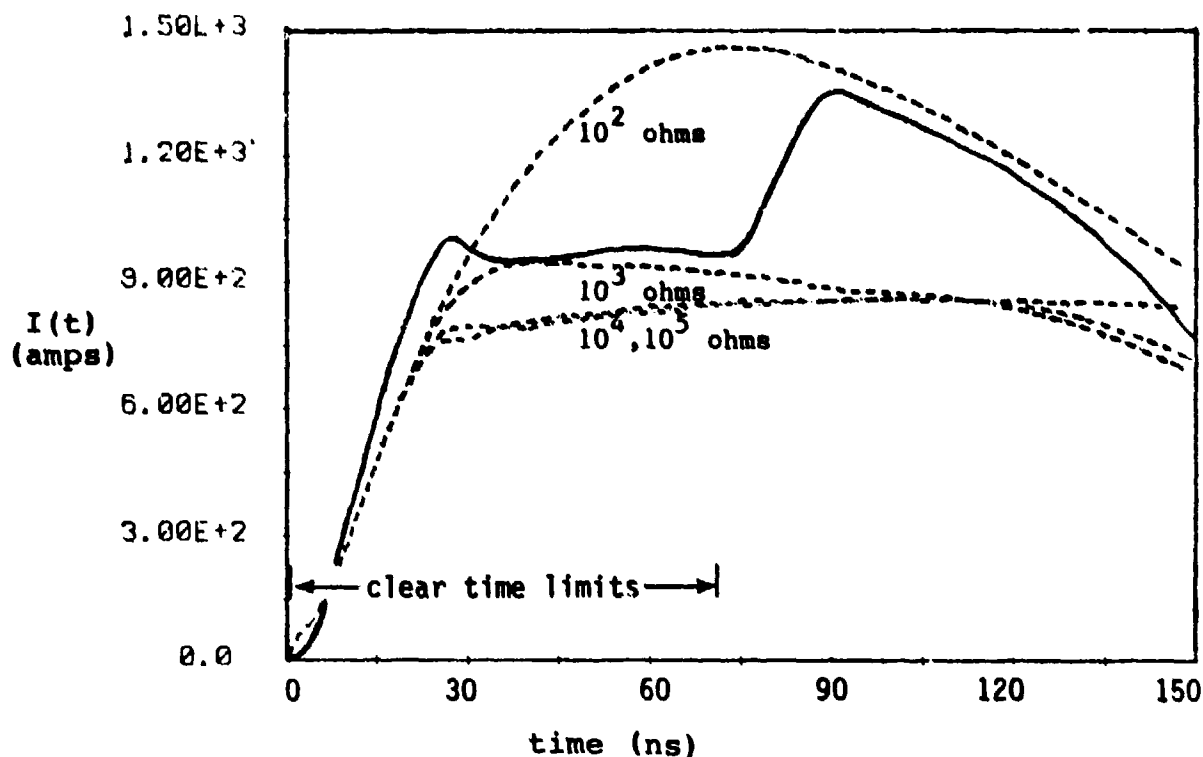
Figure 62. Comparison of Measured (———) and Kudyan/Shih Model (---) Results:

$E_c = 4$ MV/m; R_1, R_2 as Indicated; $C_1, C_2 = 10^{-9}$F
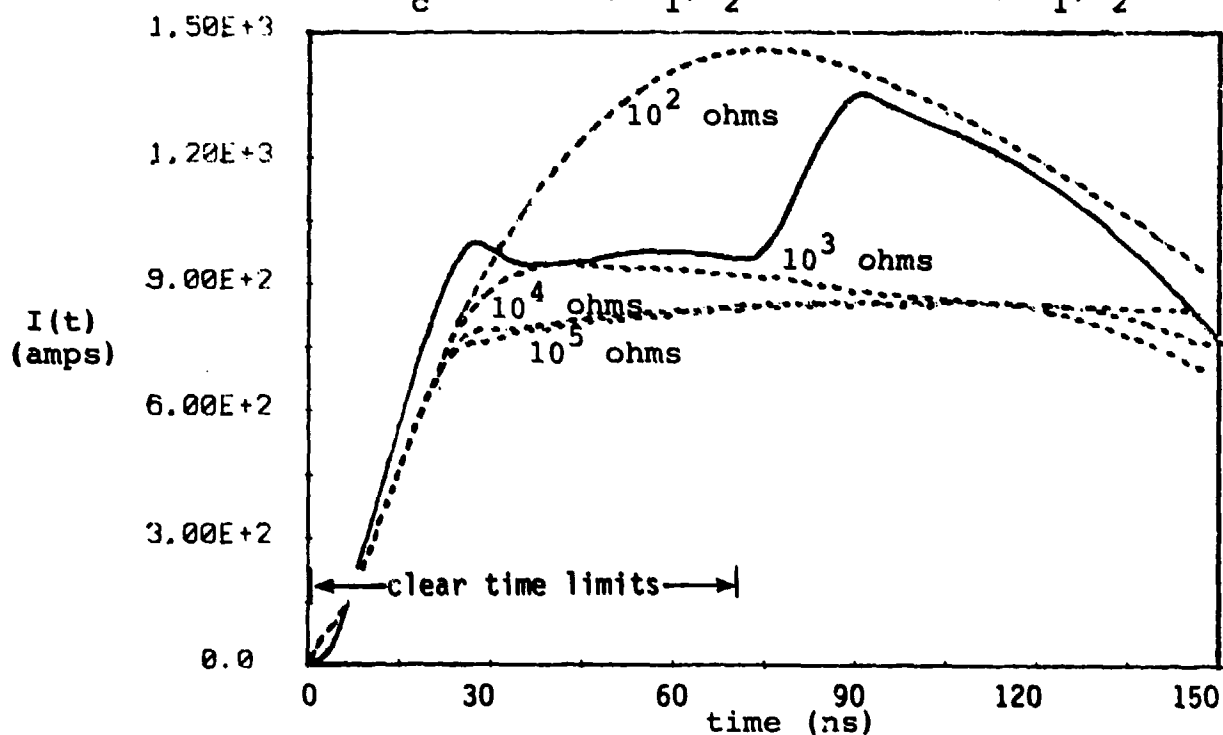
Figure 63. Comparison of Measured (———) and Kudyan/Shih Model (---) Results:

$E_c = 4$ MV/m; R_1, R_2 as Indicated; $C_1, C_2 = 5 \times 10^{-10}$F
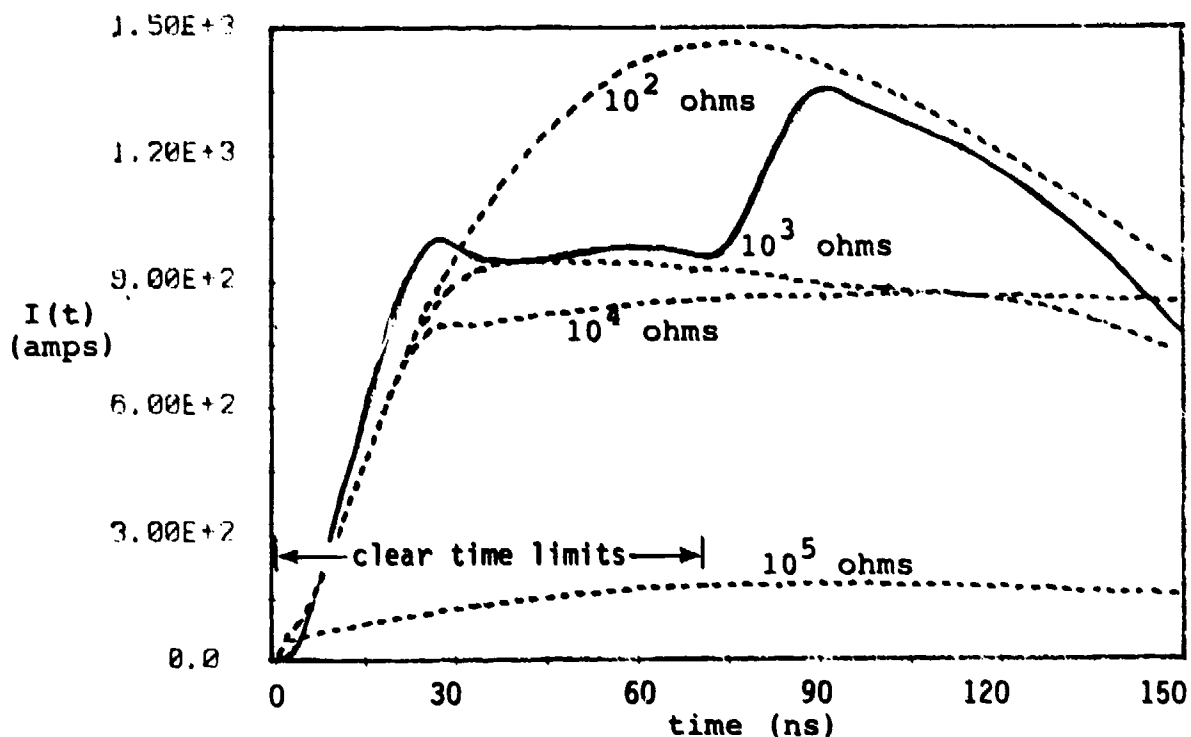
Figure 64. Comparison of Measured (——) and Kudyan/Shih Model (---) Results:

$E_c = 4$ MV/m; R_1, R_2 as Indicated; $C_1, C_2 = 10^{-10}$F
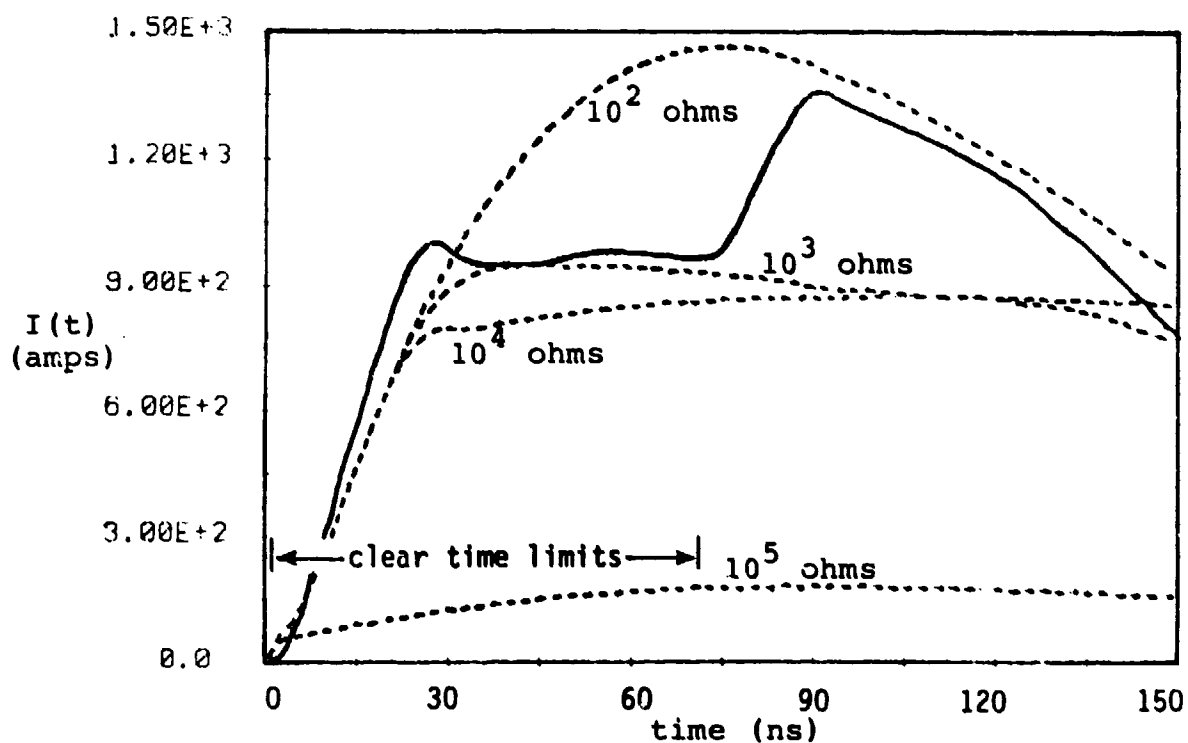
Figure 65. Comparison of Measured (——) and Kudyan/Shih Model (---) Results:

$E_c = 4$ MV/m; R_1, R_2 as Indicated; $C_1, C_2 = 5\times10^{-10}$F

94

1.50E+3

1.20E+3

10^2 ohms

9.00E+3

I(t)
(amps)

6.00E+3

3.00E+3

|←—clear time limits——→|

10^3 ohms

$10^4,10^5$ ohms

0.0

0   30   60   90   120   150

time (ns)
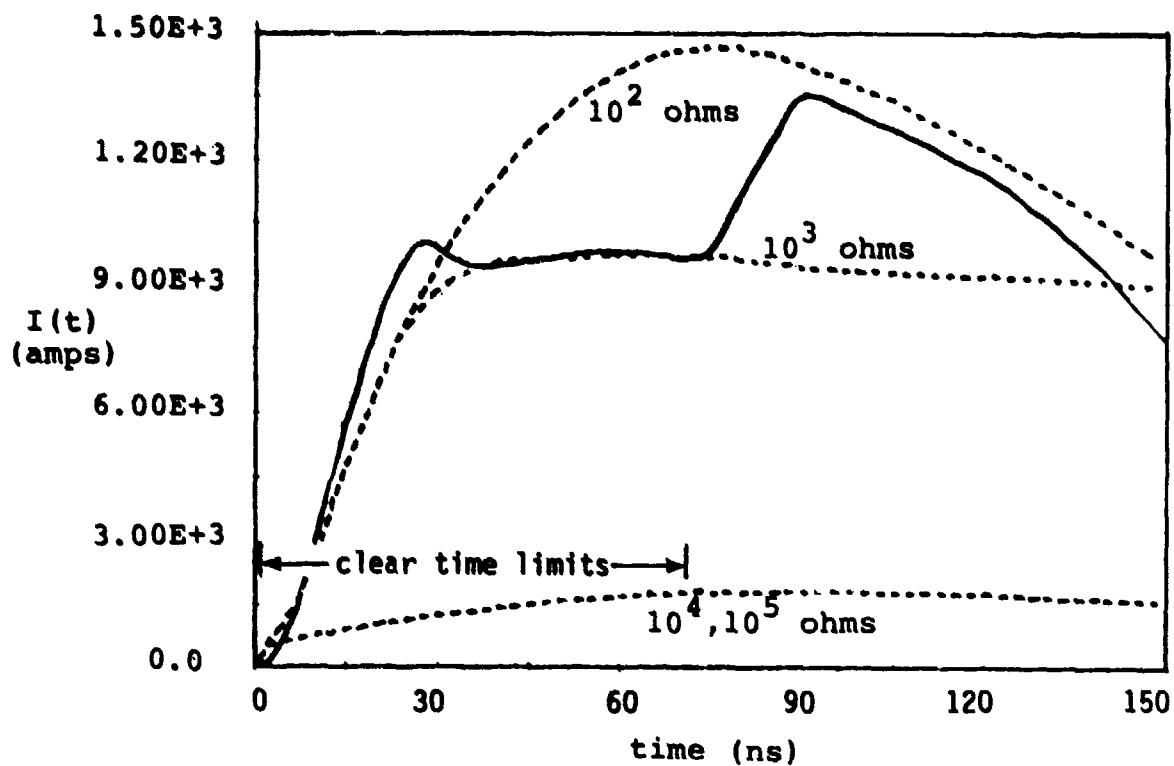
Figure 66. Comparison of Measured (——) and Kudyan/Shih Model (---) Results:

$E_c = 4$ MV/m; R_1,R_2 as Indicated; $C_1,C_2 = 10^{-11}$F
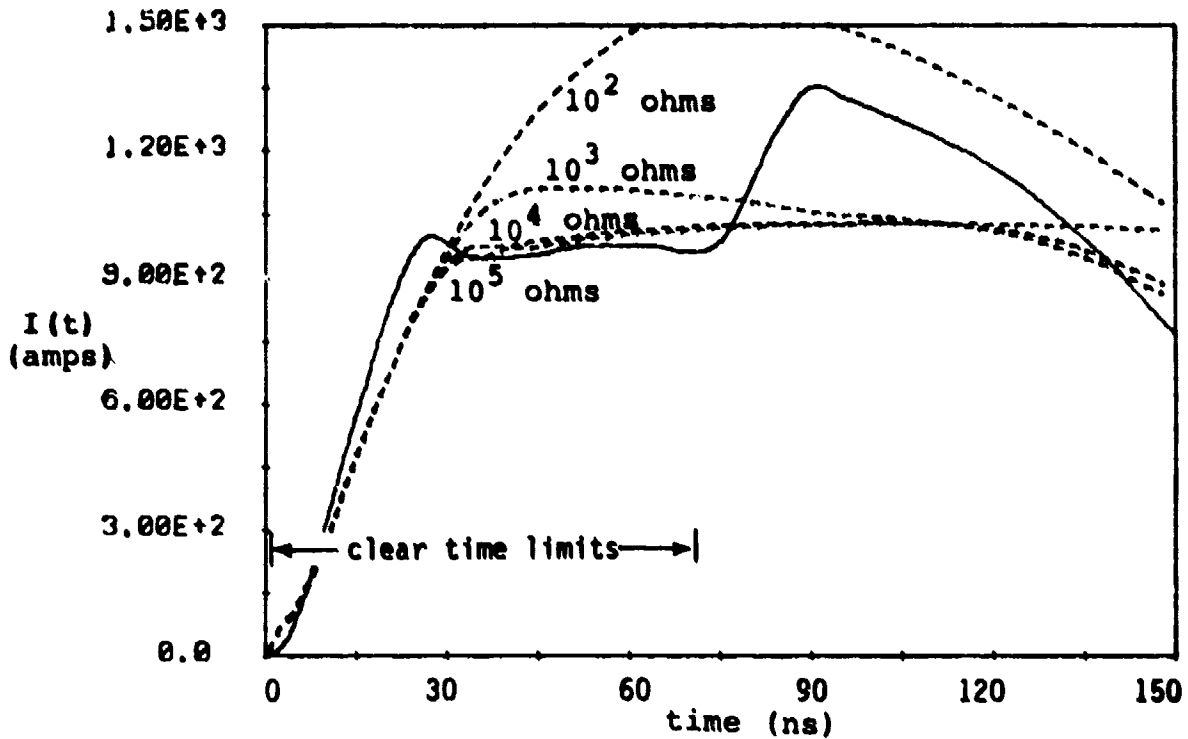
Figure 67. Comparison of Measured (——) and Kudyan/Shih Model (---) Results:

$E_c = 5$ MV/m; R_1, R_2 as Indicated; $C_1, C_2 = 10^{-9}$F
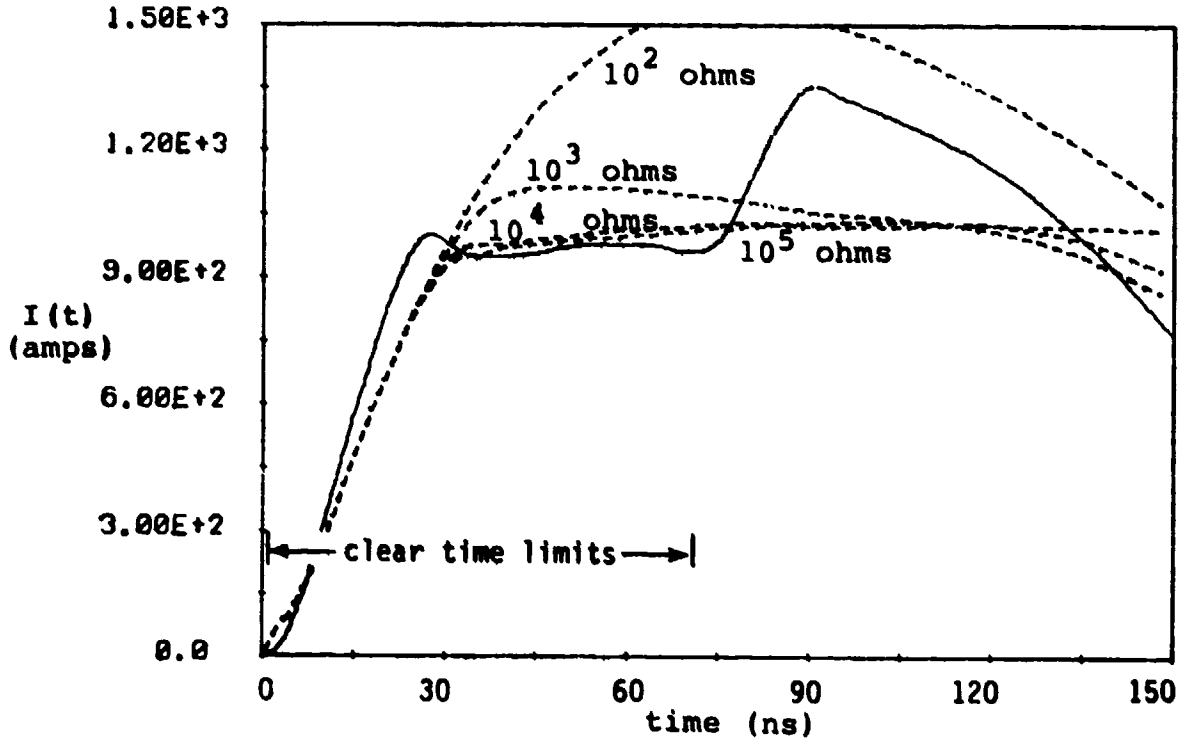
Figure 68. Comparison of Measured (——) and Kudyan/Shih Model (---) Results:

$E_c = 5$ MV/m; R_1, R_2 as Indicated; $C_1, C_2 = 5 \times 10^{-10}$F
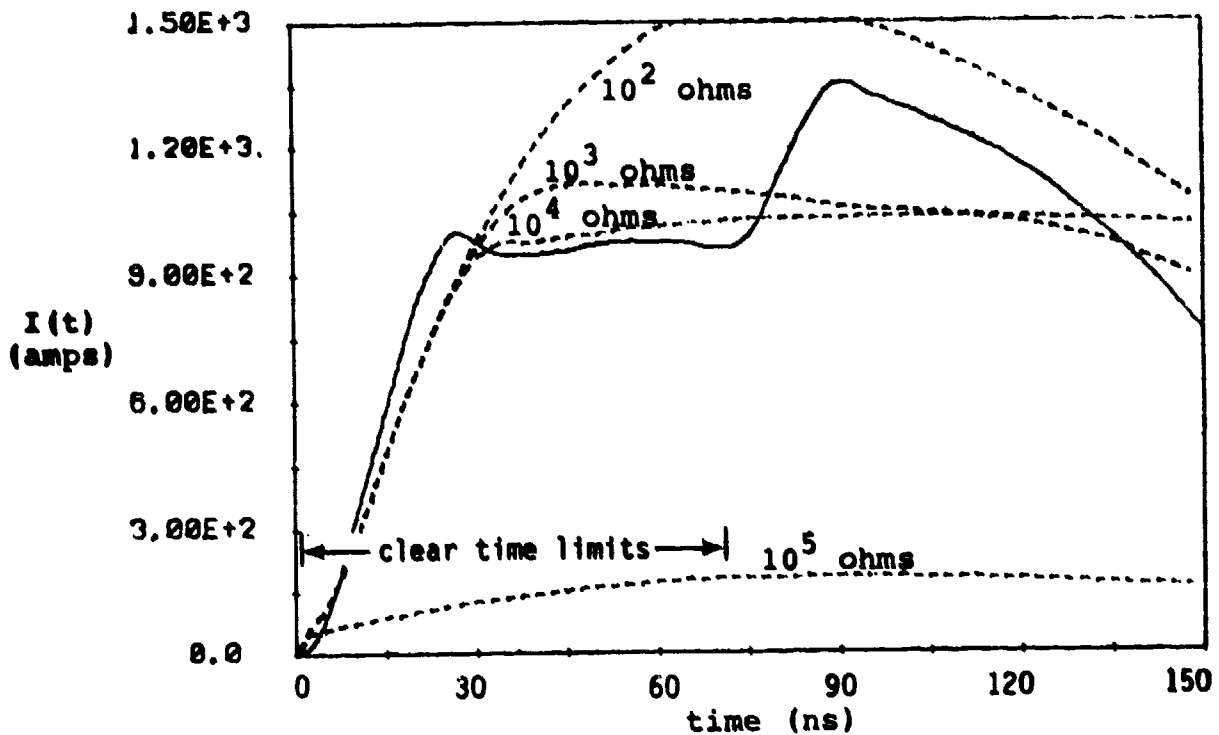
Figure 69. Comparison of Measured (——) and Kudyan/Shih
Model (---) Results:

$E_c = 5$ MV/m; R_1, R_2 as Indicated; $C_1, C_2 = 10^{-10}$ F
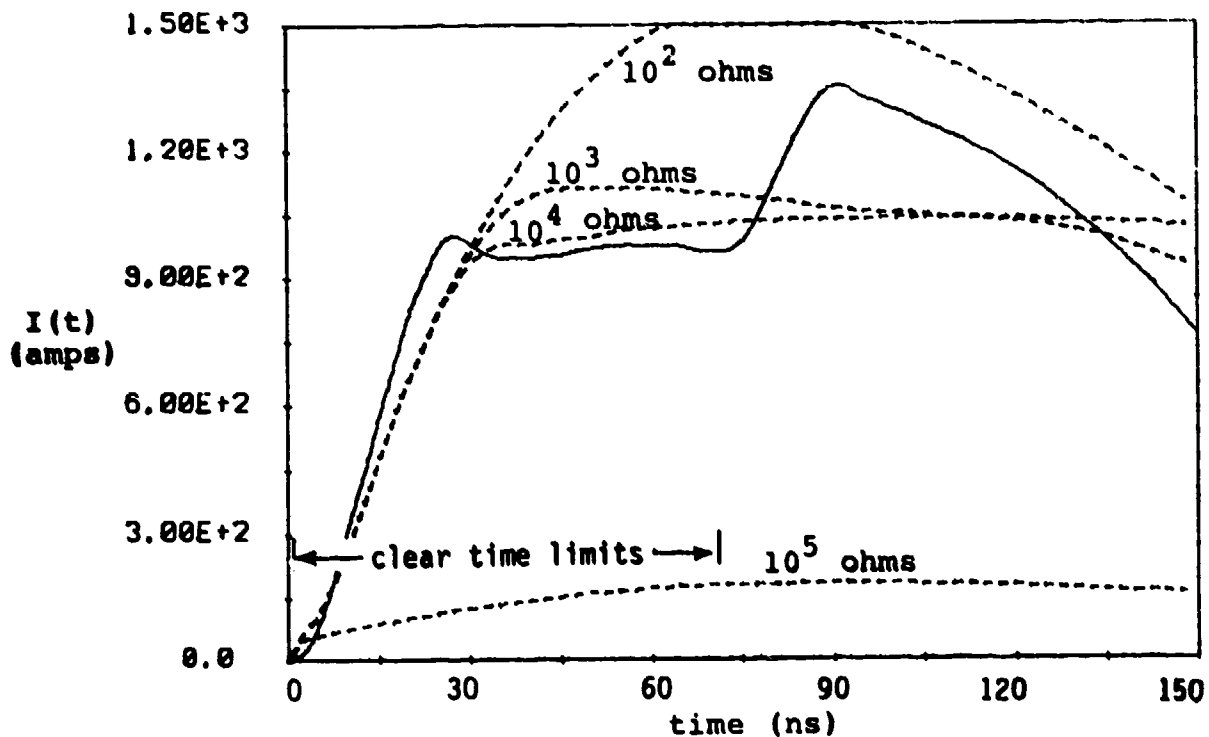
Figure 70. Comparison of Measured (——) and Kudyan/Shih
Model (---) Results:

$E_c = 5$ MV/m; R_1, R_2 as Indicated; $C_1, C_2 - 5 \times 10^{-11}$ F
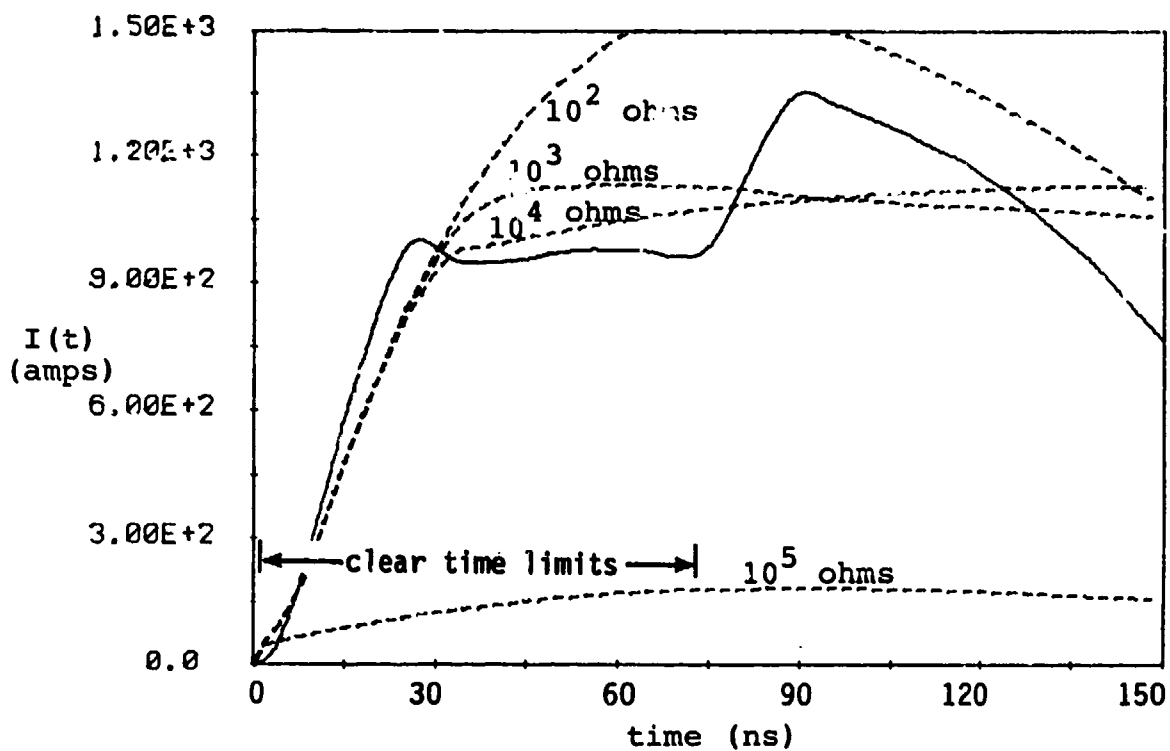
Figure 71. Comparison of Measured (——) and Kudyan/Shih
Model (---) Results:

$E_c = 5$ MV/m; R_1, R_2 as Indicated; $C_1, C_2 = 10^{-11}$ F

2. Discussion of Results

Variables:

E_C E-field value at which breakdown occurs

C_1, C_2 Capacitances in nonlinear model circuit element

R_1, R_2 Resistances in nonlinear model circuit element

Limitations:

Peek's law constrains 2.5×10^6 V/m $< E_C < 4.5 \times 10^6$ V/m.

Lacking sufficient information to make a realistic distinction between negative and positive coronas, it was assumed that $R_1 = R_2$ and $C_1 = C_2$. It is unknown to what extent this assumption affects how closely the model predictions match the experimental data.

This model may be more accurate for predicting the EMP response of a conducting line carrying AC, since the phenomenon described closely resembles "dielectric hysteresis" as described in paragraph 129, section 2-33 of [19]. The experiment performed utilized a conducting test line carrying no current, AC or DC. Future tests may wish to explore the

impact of superposi...; the EMP induced current on a current carrying test line.

Variations tested:

E_c: 1.0 x 10^6, 2.0 x 10^6, 3.0 x 10^6, 4.0 x 10^6, 5.0 x 10^6 (all in V/m)

$C_1 = C_2$: 1.0 x 10^{-9}, 5.0 x 10^{-10}, 1.0 x 10^{-10}, 5.0 x 10^{-11}, 1.0 x 10^{-11} (all in farads)

$R_1 = R_2$: 100, 1000, 10000, 100000 (all in ohms)

Note that although all these variations were tested, the results presented are a subset of the variations indicated.

Results:

The results of this model compared somewhat favorably with the experimental data are presented in Figures 62-71. For E_c < 4.0 x 10^6 V/m, the fit of the model to the experimental data is poor at all chosen values of R_1, R_2, C_1, and C_2. At E_c = 4.0 :: 10^6 V/m, the fit is fair for all ranges of C_1 and C_2 when $R_1 = R_2$ = 10000 ohms , with the best fit found when $C_1 = C_2$ = 10^{-11} farads. At E_c = 5.0 x 10^6 V/m, better fits were found when $R_1 = R_2$ = 100 ohms and 5 x $10^{-10} \leq C_1 = C_2 \leq 10^{-9}$ farads as well as for $R_1 = R_2$ = 1000 ohms and 5 x $10^{-11} \leq C_1 = C_2 \leq 10^{-9}$ farads.

V. CONCLUSIONS

Five separate corona models were compared against a
baseline test case (i.e. a representative example of the
acquired experimental data) to determine the model providing
the closest fit to that measured data. In general, three
models appeared to fit the measured data reasonably well: the
Townsend and Conductivity models proposed by Engheta et al.
[7] and the corona model proposed by Kudyan and Shih [13].
When a mobility for appropriate for ions was used in the Mo
model [16], its predictions fit the acquired data fairly well
also.

The Baum model [6] showed insufficient current
suppression once corona effects were noted. This model
neglected the physics of corona formation and assumed that all
current suppression was due to a change in effective
per-unit-length line capacitance brought on by the presence of
corona. The transmission line was also assumed to be
lossless. It is possible that including some consideration of
both the line losses and a more detailed look at the physics
of corona and its formation might improve the predictions of
this model.

The model proposed by Mo demonstrated a remarkable fit to the acquired data when an ion mobility value was used for the model parameter μ_e. However, when a mobility value appropriate for electron was used instead, the model results were unstable and never approached the experimental data. This may reflect inadequacies in the form of solution chosen when applied to this particular model or it may indicate that ions were the actual charge carriers involved in corona formation.

The models demonstrating good fits to the experimental data were the Townsend, Conductivity, Kudyan/Shih (also commonly referred to as the "Hysteresis" model) and the Mo model (assuming ions as primary charge carriers in the formation of corona). In the Townsend model, the best fit is seen when $\alpha_j = 100 \text{ V}^{-1}\text{s}^{-1}$ and $E_c = 4.5 \text{ MV/m}$ (see Figure 48). Recall that α_j in this model is, in essence, a measure of the rate of corona formation. The Conductivity model most closely matched the measured data when $\sigma = 5.0 \times 10^{-5}$ mhos/m and $4.5 \leq E_c \leq 5.0$ MV/m. Here, σ is a measure of the corona conductivity. The Hysteresis model generally fit the measured data when $4.5 \leq E_c \leq 5.0$ MV/m and $R_1 = R_2$ was between 10^3 and 10^4 ohms. Varying $C_1 = C_2$ had minimal effect within this range. Perhaps the best fit of this model to the acquired data was for $R_1 = R_2 = 10^3$ ohms and $C_1 = C_2 = 10^{-11}$ F. The Mo model fit the acquired data

best for $\mu_e = 2 \times 10^{-4}$ m^2/V-s, 4.5 MV/m $< E_c <$ 5.0 MV/m and s_o on the order of 10^{-2} mhos. It may be noted that none of these models fits the measured data extremely well in the time prior to corona formation and immediately after its effects are noted.

Clearly, much work remains to be done. The comparisons made in this paper indicate a limited group of the comparisons that could be made. Some models may demonstrate better fits for other sets of acquired data. By the same token, the models demonstrating good fit for the selected baseline case may not continue to fit other pieces of acquired data. During the experiment, over 400 sets of data were acquired, representing more than 20 different test configurations [see Reference 3]. It may be useful to understand the variations within data sets for the same configuration and to check the fit of each model to an appropriate representative data set for each of the configurations. These tests may more clearly indicate the strengths and weaknesses of each model.

REFERENCES

1. Legro, J.R., et al., "Study to Assess the Effects of Electromagnetic Pulse on Electric Power Systems: Phase I Executive Summary, Oak Ridge National Laboratory Report, ORNL/Sub/83-43374/1/V1, September, 1985.

2. Blanchard, J.P., et al., "Task 5 Report: Test Data Overview from Experimental Investigation of the Effects of Corona on Current Surges on Long Lines by EMP", submitted to Oak Ridge National Laboratory, Subcontract number 19X-027461C, June 1986.

3. Blanchard, J.P., and S.S. Russell, "Data Collected from an Experimental Determination of EMP Induced Corona Effects on Conducting Lines", DNA publication, in progress.

4. Goldman, M., and A. Goldman, "Corona Discharges", Gaseous Electronics, Vol. I, Academic Press, Inc., 1978.

5. Peek, F.W., "Law of Corona and Dielectric Strength of Air", AIEE Trans., Vol. 30, pp. 1889-1965, June 1911.

6. Baum, C.E., "Effect of Corona on the Response of Infinite-Length Transmission Lines to Incident Plane Waves", to be published in the Proc. of the 1987 Zurich EMC Symposium, Zurich, Switzerland.

7. Engheta, N., et al., "HEMP-Induced Transients in Transmission and Distributions (T&D) Lines", Oak Ridge National Laboratory Report ORNL/Sub/84-73986/1, September, 1985.

8. Townsend, J.S., "Die Ionisation der Gase", Handbuch der Radiologie Band I, Akademisher Verlag, Leipzig, 1920.

9. Standard EMP and Lightning Instrumentation, EG&G Washington Analytical Services Center, Inc., Data Sheet 1122, September 1980.

10. McEachman, K.B., et al., "Traveling Waves on Transmission Lines with Artificial Lightning Surges", AIEE Trans., Vol 49, pp. 855-894, July 1930.

11. Brune, O. ad J.R. Eaton, "Experimental Studies on the Propagation of Lightning Surges on Transmission Lines", AIEE Trans., Vol 50, pp. 1132-1138, September 1931.

References (cont'd)

12. Wagner, C.F., and B.L. Lloyd, "Effects of Corona on
    Traveling Waves", AIEE Trans., Vol 74, pp. 858-872,
    October 1955.

13. Kudyan, H.M., and C.H. Shih, "A Nonlinear Circuit
    Model for Transmission Lines in Corona", IEEE PES
    Paper 80 SM 684-1, presented July 13-18, 1980.

14. Lee, K.C., "Non-Linear Corona Models in an Electro-
    magnetic Transients Program (EMTP)", IEEE PES Paper
    83 WM 224-3, presented January 30 - February 4, 1983.

15. Gary, C., et al., "Prediction of Surge Propagation
    Influenced by Corona and Skin Effect", IEE Proceedings,
    Vol. 130, No. 5, July 1983.

16. Mo, T.C., "Effect of Corona on EMP-Induced Wire
    Current", R&D Associates report RDA-TR-117900-001,
    December, 1981.

17. Chen, K.C., "Transient Corona Effects on a Wire Over
    the Ground", Proc. Lightning Technology, NASA Conf.
    Pub. 2128 and FAA-RD-80-30, April 1980, pp. 265-281.

18. Rogers, S.R., and R.A. Perala, "The Effects of Corona
    and Angle of Arrival on the EMP Response of Cables
    Lying on the Surface of the Earth", Harry Diamond
    Laboratories Report, HDL-CR-83-004-1, February, 1983.

19. Fink, D.G., and H.W. Beaty, Editors, "Standard Handbook
    for Electrical Engineers", 11th edition, McGraw Hill
    Book Company, 1978.

20. McConnell, B.W., Martin-Marietta Energy Systems, Oak
    Ridge National Laboratory, Oak Ridge, Tennessee,
    private communication, September 1986.

21. Liu, T.K., "Transient Analysis of TEM Transmission
    Lines", Proceedings of the IEEE, June, 1968,
    pp. 1090-1092.

22. Lee, K.S.H., and L. Marin, "SGEMP for Resonant Structures",
    AFWL Theoretical Notes, Note 199, Air Force Weapons
    Laboratory, New Mexico, September, 1974.

23. Cheng, D.K., Field and Wave Electromagnetics, Addison-
    Wesley Publishing Company, Menlo Park, CA, 1983.

24. Davies, D.K., and P.J. Chantry, "Air Chemistry
    Measurements II", AFWL Theoretical Notes, Note 352,
    Air Force Weapons Laboratory, New Mexico, July 1984.

References (cont'd)

25. EMP Interaction: Principles, Techniques and Reference
    Data (A Compleat Concatenation of Technology from the
    EMP Interaction Notes), EMP Interaction 2-1. K.S.H. Lee,
    editor. AFWL-TR-80-402. Air Force Weapons Laboratory,
    NM, December 1980.

INTERNAL DISTRIBUTION

1-24.	P. R. Barnes	36.	J. N. MacDonald
25.	R. B. Braid	37.	B. W. McConnell
26.	R. S. Carlsmith	38.	M. O. Pace
27.	F. C. Chen	39-43.	D. J. Slaughter
28.	L. G. Christophorou	44.	R. A. Stevens
29.	R. I. Cruther	45-46.	J. P. Stovall
30.	S. J. Dale	47.	Central Research Library
31.	W. Fulkerson	48.	Document Reference Section
32.	P. A. Gnadt	49.	Energy Information Library
33.	T. L. Hudson	50-52.	Laboratory Records - RC
34.	M. A. Kuliasha	53.	Laboratory Records Department
35.	F. C. Maienschein	54.	ORNL Patent Section

EXTERNAL DISTRIBUTION

55. V. D. Albertson, Department of Electric Engineering, 123 Church Street, S.W., University of Minnesota, Minneapolis, MN 55455

56. D. J. Allan, Technical Manager GEC Power Transformer Limited P. O. Box N. 26, Lichfield Road, Stratford, England ST174IN United Kingdom

57. H. W. Askins, Jr., The Citadel, Charleston, SC 29409

58. AT&T Information Systems, Division Manager, Building 83, Room 1B23, 100 Southgate Parkway, Morristown, NJ 07960

59. C. E. Baum, AFWL/NTAB, Kirkland AFB, NM 87117-6008

60. R. Bellem, Director for Radiation, Defense Nuclear Agency, Washington , DC 20305

61. Guy Bellot, Engineering Manager/DAS Dept, Division Travaux Exterieurs et Services, Thompson - CSF, 34 Boulevard Ornano B.P. 130 1 Saint-Denis Cedex 93204, France

62. D. W. Boehm, DCA, Code R-430, DCEC, 1860 Wiehill Avenue Reston, VA 22090-5500

63. J. N. Bombardt, R & D Associates, 105 E. Vermijo Street, Suite 450, Colorado Springs, CO 80903

64. G. E. Brackett, Code H25, Navy Surface Weapons Center, 1092 New Hampshire Avenue, Silver Springs, MD 20903-5000

65. E. H. Brehm, Department GK/CN32, Brown, Boveri, and Cie, Aktiengesellschaft, Postfach 351, D-6800 Mannheim 1, WEST GERMANY

66. F. C. Buchholz, Pacific Gas & Electric Co. 77 Beagle Street Room 2933, San Francisco, CA 94106

67. J. F. Buck, Wisconsin Electric Power Company, 231 W. Michigan, Milwaukee, WI 53201

68. L. M. Burrage, McGraw-Edison, P. O. Box 100, 11131 Adams Road, Franksville, WI 53126

69. H. S. Cabayan, Lawrence Liversmore Laboratory, P. O. Box 5504 Liversmore, CA 94550

70. F. L. Cain, Georgia Institute of Technology, Engineering Experiment Station, Atlanta, GA 30332

71. J. G. Carbonell, Carnegie-Mellon University, Pittsburgh, PA 15213

72. R. N. Carlile, Department of Electrical and Computer Engineering, University of Arizona, Tucson, Arizona 85721

73. I. J. Carney, Nuclear Survivability Organization, Boeing Aerospace Company, P. O. Box 399, Seattle, WA 98124

74. V. L. Chartier, Bonneville Power Administration, P. O. Box 491-ER Vancouver, WA 98666

75. K. K. Chen, Sandia National Laboratory, Drawer 1333, P. O. Box 5800 Kirkland AFB, NM 87185

76. R. F. Chu, Philadelphia Electric Company, 2301 Market Street, MS 10-1 P. O. Box 8699, Philadelphia, PA 19101

77. H. E. Church, Aluminum Company of America, 1505 Alcoa Building, Pittsburgh, PA 15219

78. B. Cikotas, Defense Communications Agency, Code 8340, Arlington Hall Station, Arlington, VA 22213-542

79. C. F. Clark, Bonneville Power Administration, P. O. Bos 3621 Portland, OR 97208

80. R. E. Clayton, Power Technologies, P.O. Box 1058, 1482 Erie Boulevard, Schenectady, NY 12301-1958

81. A. Clerici, Sanelmi, Via Pergolesi 25, 20124 Milani, Italy

82. H. W. Colburn, North American Electric Reliability Council, 101 College Road East, Princeton, NJ 08540-6601

83. P. L. Collins, Defense Intelligence Agency, VP-TPO, Washington, DC 20301-6111

84. D. E. Cooper, Southern California Edison Company, P.O. Box 800, 2244 Walnut Grove Avenue, Rosemead, CA 91770

85. R. Cortina, ENEL-Centro Ricera, Automatica, VIA Volta 1, Cologno Monzese (MI), ITALY

86. Commander, White Sands Missle Range, ATTN: STEWS-TE-NO Kent Cummings White Sands Missle Range, NM 88002

87. G. Dahlen, Royal Institute of Technology, S-100-44, Stockholm, SWEDEN

88. J. Darrah, Headquarters, NORAD/G5, Perterson AFB, CO 80914

89. W. M. Druen, 8200 South Memorial Parkway, Suite D. Huntsville, Alabama 35802

90. Nadir Engheta, Dikewood, Division of Kaman Sciences Corporation 1613 university Blvd., N.E. Albuquerque, NM 87102

91. J. C. Engimann, Commonwealth Edison, 1319 S. First Avenue, Maywood, IL 60153

92. D. M. Ericson, Jr., Sandia National Laboratory, Division 6414 Kirkland AFB, NM 87185

93. Owen Farish, University of Strathclyde, Department of Electrical and Electronic Engineer. Glasgow Scotland G11XW, United Kingdom

94. W. E. Ferro, Electric Research and Management, Inc., P. O. Box 165 State College, PA 16804

95. W. G. Finney, Project Manager, Stanley Consultants Incorporated, Stanley Building, Muscatine, IA 52761

96. F. Fisher, GE Corporation, Electric Utility Systems Engineering, Building 5, room 306, Schenectady, NY 12345

97. M. Fitgerald, MITRE Corporation, P.O. Box 208, Bedford, MA 01730

98. P. B. Fleming, Science & Eng Associates, Mariners Square, Suite 127 1900 N. Northlake Way, P.O. Box 31819, Seattle, WAs 98103

99. R. Gates, Research Division, Federal Emergency Managment Agency, 500 C Street, SW, Washington, DC 20472

100. M. R. Gent, North American Electric Reliability Council, 101 College Road East, Princeton, NJ 08540-6601

101. W. Graham, R & D Associates, P.O. Box 9695, Marina Del Ray, California 90291

102. J. J. Grainger, Electric Eng. Department, North Carolina State University, 5004 Hermitage Drive, Raleigh, NC 27612

103. I. S. Grant, Power Technologies Incorporated, 1482 Erie Boulevard, Schebectady, NY 12305

104. A. R. Gritzke, U. S. Department of Navy, Nuclear Warfare Projects Office, Washington, DC 20360

105. J. Cut, Institute of Military Security Technology , Auf der Mauer 2 Zurich CH-8001, SWITZERLAND

106. V. Guten, National Security Agency (R-52), fort G. Mead, MD 20755

107. Dr. John Hamm, SRI - Albuquerque, 1900 Randolph Road, S.E. Albuquerque, NM 871076

108. M. H. Heese, Rensselaer Polytechnic Institute, JEC 5008, Troy, NY 12181

109. D. Higgins, JAYCOR, Santa Barbara Facility, 360 South Hope Avenue P.O. Box 30281, Sanata Barbara, CA 93105

110. D. W. Hilson, Power Electronics Application Center, 10521 Research Drive, Suite 400, Knoxville, TN 37932

111. Dr. Narain Hingorani, Electric Power Research Institute, P. O. Box 10412, Palo Alto, CA 94303

112. F. C. Holdes, Pacific Gas & Electric Company, 3235-18th Street, San Francisco, CA 94110

113. W. S. Howington, Normanda Aluminum, Inc., P.O. Box 70, New Madrid, MO 63869

114. J. Hunt, Emergency Puporedners, San Diego Gas & Electric Company P.O.Box 1831, San Diego, CA 92112

115. Dr. R. H. Hutchins, BDM Corporation, 1801 Randolph, SW, Albuquerque, NM 87106

116. Hugh M. Hyatt, Applied Pulse Corp. (APC), 153 Commerical Avenue Sunnyvale, CA 94086

117. M. Ianovici Ecole Polytecnique Federal des Lausame, EPFL-LRE Laboratorie de reseaux d'energie electrique 16, ch. de Bellerive CH-1007 Lausame SWITZERLAND

118. V. Inkis, Ontario Hydro, U7E1, 700 University Avenue, Toronto, Ontario M5G1X6, CANADA

119. Dr. Peter B. Johns, Department of Electrical an Electronic Engineering, University of Nottingham, Nottingham, NG7 2RD ENGLAND

120. Paul B. Jacobs,Mississippi State University, P.O. Drawer EE Mississippi State MS 39762

121. Wasyl Janischewskj, University of Toronto, Electrical Eng. Department, Toronto, Ontario, M5S1A4, CANADA

122. H. P. Johnson, Georgia Power Company, 270 Peachtree Street, 11th Floor, Atlanta, GA 30303

123. C. W. Jones, Metatech Corp, 2305 Renerd Place SE Suite 200 Albequerque, NM 87108

124. V. K. Jones, Science & Engineering Associates, Inc., Mariners Square Suite 127, 1900 N. Northlake Way, P.O. Box 31819, Seattle, WA 98103

125. F. R. Kalhammer, Electric Power Research Institute, 3412 Hillview Avenue, P.O. Box 10412, Palo Alto, CA 94303

126. T. Karlsson, FOA 387, Box 1165, Likoping, 58111 SWEDEN

127. W. Karzas, R & D Associates, P.O.Box 9695, Marina Del Rey, CA 90291

128. R. E. Kasperson, Clark University, Graduate School Of Geography Worchester, MA 01610

129. W. K. Klien, U.S. Dept. of Energy, 1000 Independence Avenue, SW, Forrestal Building, Room 5E-052, Washington, DC 20585

130. J. Kopefinger, Duquensne Light Company, System Planning Department 21-2, 1 OxFord Center, Pittsburgh, PA 15279

131. N. Kolcio, American Electric Power, 1 Riverside Plaza, Columbus, OH 43216

132. D. C. Koury, SHADE, CIS PCB SES, Apo, NY 09055

133. T. R. LaPorte, Institute of Government Studies, 109 Moses Hall, Berkeley, CA 94720

134. J. Labadie, IRT, 6800 Poplar Place, McLean, VA 22131

135. H. T. Lam, South Carolina Public Service Authority, 1 Riverwood Drive, Monks Corner, SC 29461

136. R. C. Latham, Duke Power Company, P.O. Box 33189, Charlotte, NC 28242

137. A. Latter, R & D Associates, P.O. Box 9695, Marina Del Rey, CA 90291

138. J. S. Lawler, University of Tennessee, Department of Electrical Engineering, Knoxville, TN 37916

139. K. S. H. Lee, Kaman Science Corporation, Dikewood Division, 2800 28th Street, Suite 3780, Santa Monica, CA 90405

140. J. R. Legro, Advanced Systems Technology, Westinghouse Electric Corporation, 777 Penn Center Blvd., Pittsburgh, PA 15235

141. M. Lessen, Consulting Engineer, 12 Country Club Drive, Rochester NY 14618

142. Library, Defense Technical Information Center, Cameron Station Alexandria, VA 22314

143. Library, JAYCOR, 205 S. Whiting Street, Alexandria, VA 22304

144. Library, Institute for Energy Analysis, ORAU, Oak Ridge, TN 37830

145. J. Lloyd, U.S. Army Engineering, USAEDH (ED-SD), P.O. Box 1600 Huntsville, AL 35087

146. J. Lacasso, Rockwell International, 3370 Meraloma Avenue, P.O. Box 4192 Mail Code 031-BB17, Anaheim, CA 92803

147. Dr. C .L. Longmire, Mission Research Corporation, P.O. Drawer 719, Santa Barbara, CA 93102

148. R. M. Maliswzewski, American Electric Power Service Corporation, 1 Riverside Plaza, P.O. Box 16631, Columbus, OH 43216-6631

149. J. N. Mallory, Southern California Edison Co., P.O. Box 800 Rosemead, CA 91770

150. G. C. Manthey, Energy R & D, DOE/ORO, Federal Building, Oak Ridge TN 37830

151. T. A. Martin, IRT Corporation, 1953 Gallows Road, Vienna, VA 22180

152. J. D. Martin, Harris Corporation, PRD Electronics Division, 6801 Jericho Turnpike, Syossett, NY 11791

153. P. S. Maruvada, Hydro-Quebec Institute of Research, 1800 Montee Ste-Julie, Varnnes, Quebec JOL2PO, CANADA

154. R. G. McCormack, CERL, U.S. Army Corps of Engineers, P.O. Box 4005 Champaign, IL 61820

155. C. Menemenlis, University of Patras, Patras, GREECE

156. David B. Miller, Mississippi State University, P.O.Drawer EE, Mississippi State, MS 39762

157. I. N. Mindel, IIT Research Institute, 10 West 35th Street, Chicago IL 60616

158. Dr. Charles T. C. Mo, R & D Associates, P.O.Box 9695, Marina del Rey, CA

159. D. L. Mohre, Cajun Electric Power Company, P.O. Box 15440, Baton Rouge, LA 70895

160. Albert Montgomery M/S R-315, Mitre Corporation, Burlington Road Bedford, MA 01730

161. B. B. Mrowca, Baltimore Gas & Electric Company, P.O. Box 1475 Baltimore, MD 21203

162. K. Müller, IABG, Insteinstrasse 20, Ottobrunn 8012, WEST GERMANY

163. E. M. Murtha, General Service Admin., Booz Allen and Hamilton 18th & F Street, NW, Washington, DC 10405

164. Dr. H. P. Neff, University of Tennessee, Dept. of Electric Engineering, Knoxville, TN 37916

165. B. O. Nettles, Enginerring Center, Navel Electronic System (Code 203) 4600 Marriott Drive, Charleston, SC 29418

166. G. B. Niles, Prin. Engineer, Baltimore Gas & Electric Company Room 1020 P. O. Box 1475, Baltimore MD 21203

167. S. Nilsson, Program Manager, Electric Power Research Institute, Electrical Systems Division , 3412 Hillview Avenue, P. O. Box 10412, Palo, Alto, CA 94303

168. D. R. Nevius, North American Electric Relaibility Council, 101 College Road East, Princeton, NJ 08540-6601

169. Principal Engineer, Baltimore Gas & Electric Company, Room 1020 P.O. Box 1475, Baltimore, MD 21203

170. B. Noel, Los Alamos National Lab., Mil Station 5000, P.O. Box 1663, Los Alamos, MN 87545

171. B. Nowlin, Arizona Public Service Company, P.O. Box 21666, Phoenix, AZ 85036

172. R. Oates, Atmoic Weapons Research Establishment, Building D57 Aldermaston, Reading RG74PR, ENGLAND

173. James O'Neil, Westinghouse Electric Corporation, 777 Penn Center Blvd. Pittsburgh, PA 15235

174. G. Orrell, Dep. Assoc. Director, Federal Emergency Management Agency, 500 C Street, SW, Washington, DC 20555

175. L. Parsi, University of Pisa, Via Diotisalvi 2, PISA 56100, ITALY

176. Dr. Sung-Won Park, Auburn University, Dept. of Electrical Engineering, 200 Braun Hall, Auburn AL 36849-3501

177. R. Parker, R & D Associates, P.O. Box 9335, Albuquerque, NM 87119

178. R. Parkison, Science Applications, Inc., 5150 El Camino Real, Suite B-31, Los Altos, CA 94022

179. R. L. Perrine, Prof. of Engineering, Civil Engineering Dept. University of California, Engineering I, Room 2066, Los Angeles, CA 90024

180. A. Pigini, CESI, Via Rubahimo 59, Milano, ITALY

181. J. B. Posey, Ohio Brass Co. 380 N. Main Street, Mainsfield, OH 44903

182. M. Rabinowitz, Electric Power Research Institute, 3412 Hillview Avenue, P.O. Box 10412, Palo Alto, CA 94303

183. W. A. Radaski, Metatech Corporation, 358 South fairview Avenue, Suite E, Goleta, CA 93117

184. A. Ramus, Maxwell Laboratories, Inc., 8835 Balboa Avenue, San Diego, CA 92123

185. J. J. Ray, Bonneville Power Administration, P.O. Box 3621, Portland, OR 92123

186. T. J. Reed, Advanced Systems Technology, Westinghouse Electric Corp. 777 Penn Center Boulevard, Pittsburgh, PA 15235

187. R. L. Retallach, American Electric Power, 1 Riverside Plaza, Columbus, OH 43126

188. J. Richardson, National Academy of Science, 2101 Constitution Avenue, Washington, DC 20418

189. F. Rosa, Division of System Intg., Nuclear Regulatory Commission, MS P1030, Washington, DC 20555

190. Lt. Col. Steven S. Russell, Field Command DNA, FCDNA/FCTO, Kirtland, AFB, MN 87115

191. Dr. Tom Reudy, AC - Laboratorium, Spoez CH-3700 Speit, SWITERZLAND

192. David R. Rutt, SRI International 333 Ravenswood Avenue Menlo Park CA 94025

193. D. H. Sandell, Haraz Engineering Co., 150 South Wacker Drive, Chicago, IL 60606

194. J. A. Sawyer, MITRE Corporation, MSH070, P.O. Box 208, Bedford, MA 01703

195. R. A. Schaefer, Metatech Corporation, 20 Sunnyside Avenue, Suite D Mill Valley, CA 94941

196. M. Schechter, A.D.A., P. O. Box 2250 (81), Haifa, 31021, ISRAEL

197. D. Serafin, Cente d'Etudes de Gramat, 46500 Gramst, FRANCE

198. Peter Sevat, Physics and Electronics Laboratory TNO, EMP Group P. O. Box 96864,Den Hagg 2509JG NETHERLANDS

199. H. Singaraju, Air Force Weapons Laboratory, Kirkland AFB, NM 87117

200. Drs. Kudyan and Shih, American Electric Power Service Corporation, 1270 Avenue of the Americas, New York, NY 10020

201. Solly Side, Managing Director, GERAC, B.P. 19 - 46500 Gramat FRANCE

202. Carol Smeerdon, Royal Aircraft Establishment, Flight Systems, BLdg. Q153, Farnborough, HANTS GU146TD ENGLAND

203. R. Smith, Defense Nuclear Agency, RAEE, 6801 Telegraph Road, Alexandria VA 22310

204. J. C. Smith, Jr. McGraw-Edison Company, Power Systems Group, P.O. Box 440 Canonsburgh, PA 15317

205. A. C. Smith, Jr., Beam Research Program, Lawrence Livermore National Lab., P.O. Box 808, Livermore, CA 9455

206. Steve Sarinen, MS-ERTH, Bonneville Power Administration, P. O. Box 491, Vancouver, Washington 98666

207. W. Sollfrey, RAND Corporation, 1700 Main Street, Santa Monica, CA 90406

208. S. Spohn, Defense Nuclear Agency, DB-6E2, Washington, DC 20301-6111

209. J. R. Stewart, Power Technologies, Inc., P.O. Box 1058, 1482 Erie Blvd., Schednectady, NY 12301-1058

210. R. L. Sullivan, Consultant, Gainesville, FL 32611

211. I. O. Sunderman, Lincoln Electric System, P.O. Box 80869, Lincoln, NE 68501

212. R. W. Sutton, Science Applications, Inc.,m 1710 Goodridge Drive P.O. Box 1303, McLean, VA 22102

213. F. M. Tesha, LuTech Inc., 3724 Mt. Diablo Boulevard, Lafayette, CA 94549

214. L. Thione, CESI Via Rubattino 54, Milano, 20734 ITALY

215. R. J. Thomas, Cornell University, 302 Phillips Hall,Ithaca, NY 14853

216. R. Torres, BDM Corporation, 1801 Randolph SW,, Albuquerque, NM 87106

217. W. Tyler, NT, Kirkland AFB, NM 87117

218. M. A. Uman, University of Florida, Department of Electrical Eng. Gainesville, FL 32611

219. E. F. Vance, Route 3 Box 268A, Fort Worth, TX 76140

220. Major Vandre, USA IDR, ATTN SGRD-UDR-E, Walter Reed Army Medical, Center, Washington, DC 20307-5300

221. Claire Vincent, IREQ (Institute de recherche d'Hydro-Quebec) 1800 Montee Ste-Julie, Varennes, Quebec JOL 2PO CANADA

222. D. R. Volzka, Wisconsin Electric Power Company, 231 West Michigan Street, Milwaukee, WI 53201

223. J. Vora, Nuclear Regulatory Commission, MS 5650 NL, Washington DC 20555

224. R. C. Webb, DNA, RAEE, 6801 Telegraph Road, Alexandria, VA 22310

225. C. D. Whitescarbee, Martin Marietta Orlando Aerospace, (SLRC) Mail point 399, P.O. Box 5837, Orlando Florida, 32855

226. Dr. F. P. Wigner, Consultant, 8 Ober Road, Princeton, NJ 08540

227. C. B. Williams, IRT Corporation, 3030 Callan Road, San Diego, CA 92121

228. D. W. Williams, Dept of Defense, Materials Research Lab, P.O. Box 50, Ascotvale, Cordite Avenue, Maribyrnonz, Victoria, AUSTRALIA

229. M. W. Wile, Forsvarets Materielverk, Stockholm, S-11588 SWEDEN

230. D. D. Wilson, Power Technologies, Inc., P.O. Box 1058, Schenectady, NY 12301

231. U. P. Wissman, AEG-Telefunken, General Electric Company, 1 River Road, Building 36-444, Schenectady, NY 12345

232. D. A. Woodford, Manitoba Hydro, System Planning Division, P.O. Box 815, Winnipeg, Manitoba R-3C-2P4, CANADA

233. H. W. Zaininger, Zaininger Engineering Company, 3408 Vance Court, San Jose, CA 95132

234. Office of the Assistant Manager for Energy Research an Development Oak Ridge Operations Office, DOE, P.O. Box E, Oak Ridge, TN 37831

235.-727. For distribution as shown in TIC-4500, Distribution Category UC-97a, b, c